KEK Proceedings 2012-7
October 2012
R

Proceedings of the Nineteenth EGS Users' Meeting in Japan

August 1 - 3, 2012.

KEK, Tsukuba, Japan

Edited by

Y. Namito, H. Hirayama and S. Ban

High Energy Accelerator Research Organization

High Energy Accelerator Research Organization (KEK), 2012

KEK Reports are available from:

High Energy Accelerator Research Organization (KEK)
1-1 Oho, Tsukuba-shi
Ibaraki-ken, 305-0801
JAPAN

Phone: +81-29-864-5137
Fax: +81-29-864-4604
E-mail: irdpub@mail.kek.jp
Internet: http://www.kek.jp

FOREWARD

The Nineteenth EGS Users' Meeting in Japan was held at High Energy Accelerator Research Organization (KEK) from August 1 to 3. The meeting has been hosted by the Radiation Science Center. More than 100 participants attended the meeting.

The meeting was divided into two parts. Short course on EGS was held at the first half of the workshop using EGS5 code. In the later half, 16 talks related EGS were presented. The talk covered the wide fields, like the medical application and the calculation of various detector responses *etc.* These talks were very useful to exchange the information between the researchers in the different fields.

Finally, we would like to express our great appreciation to all authors who have prepared manuscript quickly for the publication of this proceedings.

Yoshihito Namito
Hideo Hirayama
Syuichi Ban
Radiation Science Center
KEK, High Energy Accelerator Research Organization

CONTENTS

Effectiveness of the Message Passing Interface Method in Reducing Computation Time 1
T. Haba, S. Kondo, D. Hayashi, A. Takeuchi, T. Ishii, H. Numamoto, and S. Koyama

Air Shower Simulation with EGS5 4
K. Okei, T. Nakatsuka, and Y. Kirihara

Application and Validation of EGS5 Code to Estimate Detection Efficiencies of Multi-Cascade Nuclides 10
Y. Unno, T. Sanami, M. Hagiwara, S. Shinichi, and T. Kurosawa

Verification of Pin-photo Diode Detector Characteristics Using EGS5 16
S. Kondo, T. Haba, D. Hayashi, H. Numamoto, T. Ishii, and S. Koyama

Influence of the Gamma Camera Collimator Geometry on Quantitative Values 21
H. Yoshino, S. Hayashi, Y. Okura, and M. Yamamoto

X-ray Computed Tomography in Consideration of the Influence of Scattered Radiation 25
K. Takemoto, K. Tokumoto, Y. Yamazaki, and N. Toda

Internal Dosimetry for Nasal Thallium-201 Administration 35
S. Kinase, K. Washiyama, H. Shiga, J. Taki, Y. Nakanishi, K. Koshida, T. Miwa, S. Kinuya, and R. Amano

Verification of the Effect of Dose Reduction System in Computed Tomography
- Evaluation of Organ and Tissue Dose Distribution Using EGS5 Simulation - 41
D. Hayashi and S. Koyama

Reduction of Radiation Dose to Children in X-Ray Head CT: Investigation Using EGS5 48
T. Ishii, S. Kondo, T. Haba, D. Hayashi, H. Numamoto, and S. Koyama

Estimation of Glandular Dose Distribution in Mammography using EGS5 53
H. Numamoto, T. Haba, S. Kondo, D. Hayashi, T. Ishii, and S. Koyama

Investigation of Physical Characteristic for High Definition Multileaf Collimator 58
Y. Iwamoto, H. Takagi, S. Hashinoguchi, H. Fujiwara, M. Tamura, T. Rachi, Y. Obata, T. Shimozato, and M. Komori

The Improvement of Discrepancy between Radiotherapy Treatment Planning System and Verification System Using Effective Density Method 66
S. Kumagai, M. Okajima, H. Takaya, N. Arai, K. Waga, T. Tanaka, M. Yasuda, K. Takimoto, J. Kotoku, and T. Kobayashi

The Study of the Collimator Scatter Factor (S_{c}) and the Phantom Scatter Factor (S_{p}) Using Monte Carlo Simulation 76
T. Rachi, Y. Iwamoto, M. Tamura, K. Ota, T. Shimosato, Y. Obata, and M. Komori

Comparison about Brachytherapy of Simulation EGS5 and Treatment Planning Based on AAPM TG-43 85
S. Tsuji and N. Narihiro

Verification of Dose Calculation for Brachytherapy Using EGS5 94
K. Tanaka, K. Tateoka, O. Asanuma, K. Kamo, K. Sato, H. Takeda, M. Takagi, M. Hareyama, and J. Takada

Effectiveness of the message passing interface method in reducing computation time

T. Haba[1], S. Kondo[1], D. Hayashi[1], A. Takeuchi[1], T. Ishii[1], H. Numamoto[1], S. Koyama[1]

[1] *Department of Radiological Technology, Graduate School of Medicine, Nagoya University*
1-1-20 Daiko-Minami, Higashi-ku, Nagoya, Japan
e-mail: haba.tomonobu@f.mbox.nagoya-u.ac.jp

Abstract

In this study, we validated the effectiveness of using a message passing interface (MPI) method in reducing computation time and enhancing calculation accuracy. A chest and abdominal X-ray computed tomography scan was simulated. Our results indicated that the MPI method was accurately incorporated into the Electron Gamma Shower ver. 5 (EGS5) MC code. The MPI method could reduce computation time from 34 hours to 6 hours. We believe that MC simulation is going to be used widely. Therefore, incorporating the MPI method into EGS5 is very useful for EGS5 users.

1. Introduction

Dose calculation using Monte Carlo (MC) simulations has been widely used in the field of medical radiation exposure over the past few years [1]. MC simulation is greatly advantageous in cases where physical measurements cannot be easily performed. However, a disadvantage of this technique is the immense computation time required to reduce statistical error. Meanwhile, in recent years, parallel computing methods such as the message passing interface (MPI) are drawing considerable attention as suitable methods for reducing computation time by distributing the calculation process across multiple central processing unit (CPU) cores. The MPI method is very useful for MC simulations. In this study, we validated the effect of reducing computation time and enhancing calculation accuracy using an MPI.

2. Materials and Methods

2.1 Simulation geometry

To consider the effect of an MPI, the following simulation was performed using the Electron Gamma Shower ver. 5 (EGS5) code. A chest and abdominal X-ray computed tomography (CT) scan was simulated. An X-ray CT humanoid phantom CTU-41 (Kyotokagaku, Kyoto, Japan) was used; this phantom was voxelized to be incorporated into the simulation. A helical Aquilion 64 X-ray CT unit (Toshiba Medical Systems, Tochigi, Japan) was used. The X-ray tube voltage was 120 kV. The scan range was from the upper border of the lung to the inferior border of the liver. Under these conditions, some organ doses (thyroid, esophagus, lung, liver, kidney) and computation time were calculated. The number of photons was 1.44 billion. Fractional standard deviation (FSD) at the center of the phantom was less than 3.0% to reduce statistical error. Energy spectra from the X-ray source along the fan beam of the CT were generated using Tucker's formula, based on the aluminum half value layer (Al HVL) measured at each angle [2]. The effect of the beam-shaping filter was incorporated into the simulation.

2.2 Performance of computer

The specification for a personal computer used in this study was as follows. The CPU was an Intel^{R} Core^{TM} i7-3960X with a clock frequency of 3.3 GHz, L2 cache memory of 256 KB × 6, L3 cache memory of 15 MB, and random access memory (RAM) of 16.0 GB. Six CPU cores were used, and the above simulation was performed using a varying number of these CPU cores.

3. Results

Table 1 shows each organ dose with various numbers of CPU cores. Each organ dose was normalized to the organ dose of the liver and had the same value for any number of CPU cores.

Fig. 1 shows the computation time for various numbers of CPU cores. The circles indicate the simulated computation time. The broken line indicates the theoretical computation time, which is obtained as follows:

$$Time_{Theo}(n) = \frac{Time_{Sim}(1)}{n}$$

where n is the number of CPU cores, $Time_{Theo}(n)$ is the theoretical computation time for n CPU cores, and $Time_{sim}(1)$ is the simulated computation time for 1 CPU core.

4. Discussion

As can be observed from **Fig. 1**, the simulated and theoretical computation times were in good agreement. **Table 1** shows that the accuracy of organ doses using any number of CPU cores was precise. This is because an adequate number of photons were simulated to reduce the statistical error. These results indicated that the MPI method was incorporated into EGS5 accurately.

Using the MPI method could reduce computation time from 34 hours to 6 hours (**Fig. 1**). This is very important because an immense amount of computation time is needed for MC simulations. We believe that MC simulation is going to be used widely. Therefore, incorporating the MPI method into EGS5 is very useful for EGS5 users. Nowadays, we can obtain CPUs with multiple cores at a low cost. It is important to select an appropriate personal computer with a suitably pre-decided budget because the relationship between computation time and the number of CPU cores is inversely proportional.

5. Conclusions

In this study, we validated the effectiveness of MPI in reducing computation time and enhancing calculation accuracy. We could incorporate the MPI method into EGS5 accurately.

References

1) S. Kondo, S. Koyama, “In-Phantom Beam Quality Change in X-Ray CT: Detailted Analysis Using EGS5”, KEK Proceedings (2011)
2) Douglas M. Tucker, “Semiempirical model for generating tungsten target x-ray spectra”, Med.Phys. 18 (1991)

Table 1 Organ dose with various number of CPU cores were shown.

		Number of CPU cores					
		1	2	3	4	5	6
Relative Organ Dose	Thyroid	1.23	1.23	1.23	1.23	1.23	1.23
	Esophagus	0.92	0.92	0.92	0.92	0.92	0.92
	Lung	1.03	1.03	1.03	1.03	1.03	1.03
	Liver	1.00	1.00	1.00	1.00	1.00	1.00
	Kidney	0.92	0.92	0.92	0.92	0.92	0.92

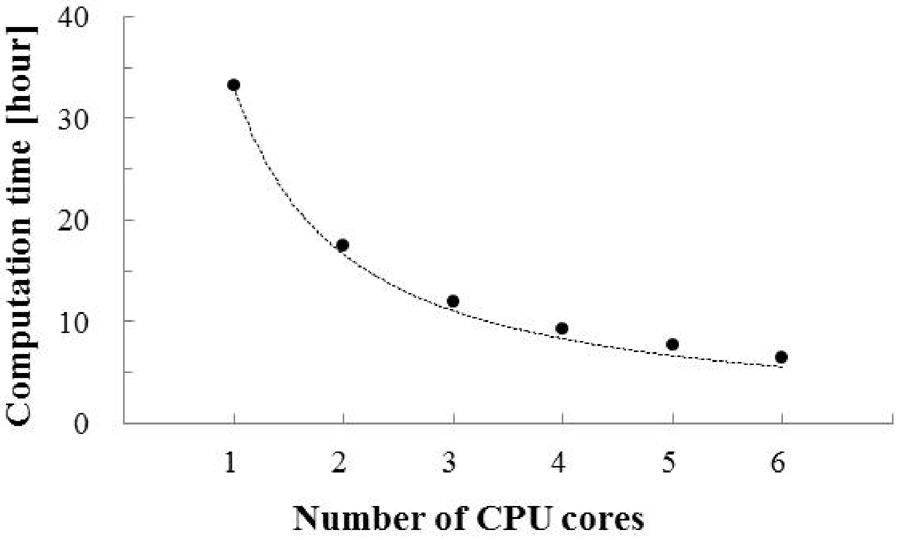

Fig. 1 Computation time with various number of CPU cores were shown.

Air Shower Simulation with EGS5

K. Okei[†], T. Nakatsuka[‡] and Y. Kirihara[✠]
[†] *Kawasaki Medical School, Kurashiki 701-0192, Japan*
[‡] *Okayama Shoka University, Okayama 700-8601, Japan*
[✠] *RIKEN Harima Institute, Sayo 679-5148, Japan*

Abstract

Air shower simulations have been performed using EGS5 as a benchmark study in the TeV region. To test the simulations, we simulated electromagnetic showers in lead and water and compared the results to those obtained by Stanev et al. (1982). The EGS5 simulation with the Landau-Pomeranchuk-Migdal (LPM) effect is functioning well overall, however results obtained with and without the LPM effect are slightly different in cases where the LPM effect is negligible. It was found that the difference is due to the sampling method and a modification of the sampling procedure is suggested to attain internal consistency.

1 Introduction

The EGS5 (Electron Gamma Shower 5) code has been improved from EGS4 in many areas, especially in low energy physics[1, 2]. The high energy physics modeling of EGS5 has also been improved recently by incorporation of the Landau-Pomeranchuk-Migdal (LPM) and dielectric suppression effect [3], and EGS5 is now applicable to simulate very high energy electromagnetic showers such as those initiated by cosmic rays.

Cosmic ray air showers are cascades initiated by cosmic rays interacting in the atmosphere. The higher the energy of cosmic rays, the smaller the flux, therefore very high energy cosmic rays can only be observed indirectly through air showers. Since the interpretation of air shower measurements strongly depends on Monte Carlo simulations, the accuracy of calculations of electromagnetic processes is important.

In this paper, we performed air shower simulations with EGS5 as a benchmark study in the TeV region.

2 Simulation

First, we performed EGS5 shower simulation without the LPM effect and the results were compared to the ones obtained from EGS4. For example, figure 1 shows the mean number of electrons with energy above 20 MeV in air showers from primary photon of energy 1 TeV. It can be seen that EGS5 consistency with EGS4 is very good for very high energy showers.

Second, photon-initiated showers in lead and water were simulated with and without the LPM effect. Figure 2 shows the longitudinal development of photon-induced showers in lead (open circles:without LPM, solid circles:with LPM). The primary photon energy E_0 is 16 TeV and the results from two different cutoff energies $E_{\rm cut}$ = 20 MeV and 0.5 TeV are shown. The result with $E_{\rm cut}$ = 0.5 TeV is to be compared with Fig. 7 of [4]. The longitudinal development of photon-induced shower in water for E_0 = 1000 TeV and $E_{\rm cut}$ = 20 MeV is shown in figure 3. This figure is to be compared with Fig. 12 of [4]. The above results show the reliability of EGS5 electromagnetic shower simulation in the TeV region.

Figure 4 shows the number of electrons as a function of depth for photon-initiated showers in homogeneous air (density: 1.205×10^{-3} g/cm^3, radiation length: 36.62 g/cm^2=303.9 m) for

$E_0 = 100$ TeV and $E_{\rm cut} = 20$ MeV. The left and right panels show the results obtained without and with the LPM effect respectively. The lines show the shower profiles for 100 individual showers and the circles show the average profile from 1000 showers. Figure 5 and 6 compare the average shower profiles obtained with and without LPM effect and figure 7 compares the lateral distribution at the depths of $t = 13.5$ and 28 radiation lengths (494 and 1025 g/cm^2).

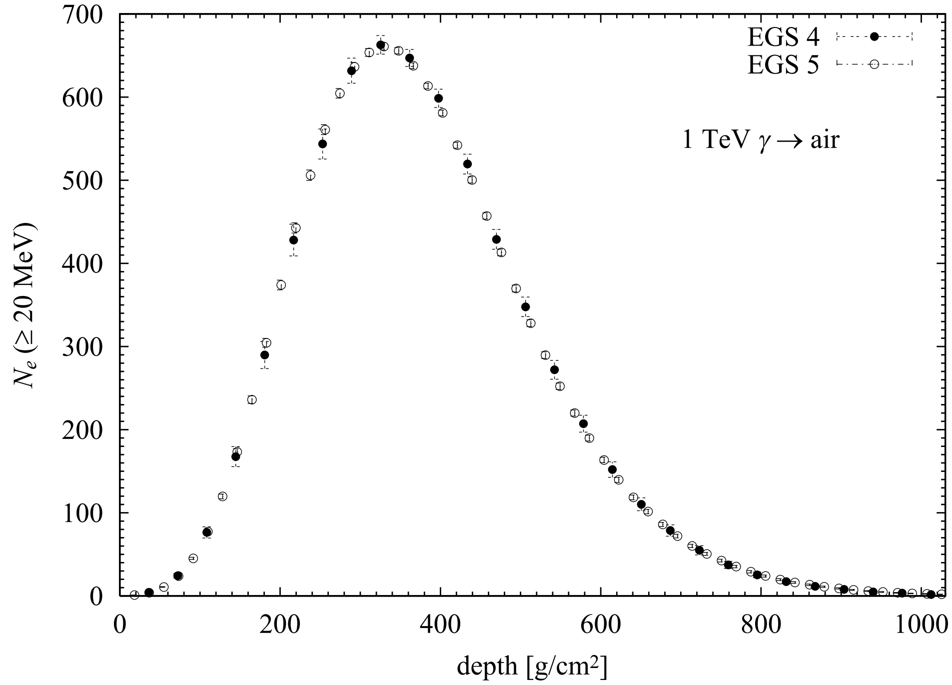

Figure 1: The mean number of electrons as a function of depth for photon-initiated showers in air for $E_0 = 1$ TeV and $E_{\rm cut} = 20$ MeV (solid circle:EGS4, open circle:EGS5).

3 Discussion

The characteristic energy $E_{\rm LPM}$ where the LPM effect becomes significant for air is ~ 200 PeV [5], whereas figure 5 of the last section shows that the average profile of 100 TeV photon shower obtained with the LPM effect is slightly different from the one obtained without the LPM effect. Here, we discuss the cause of the difference.

The Bethe-Heitler bremsstrahlung differential cross section per radiation length is

$$\sigma_{\rm BH}(y) = \frac{1}{y}\left[y^2 + \frac{4}{3}(1-y)\right] \tag{1}$$

but the cross section used in EGS5 includes several additional terms

$$\sigma_{\rm EGS}(y) = \sigma_{\rm BH}(y) + \Delta, \tag{2}$$

and the LPM cross section given by Migdal has the form

$$\sigma_{\rm LPM}(y) = \frac{\xi(s)}{y}\left[y^2\Psi(s) + \frac{4}{3}(1-y)\phi(s)\right] \tag{3}$$

where y is the fractional energy of the secondary photon [1, 3, 4, 5, 6, 7]. As y approaches 1, $\xi(s)$, $\Psi(s)$ and $\phi(s)$ approach 1 and $\sigma_{\rm LPM}(y)$ matches $\sigma_{\rm BH}(y)$ ($\sigma_{\rm LPM}(y)/\sigma_{\rm BH}(y)$ approaches 1).

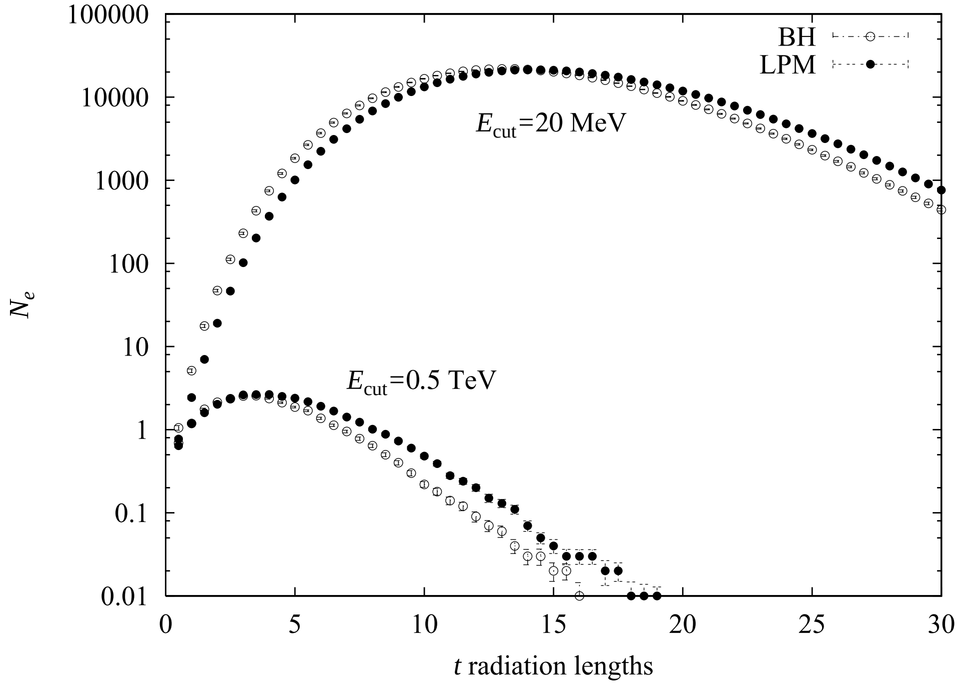

Figure 2: Longitudinal development of photon-induced showers in lead for $E_0 = 16$ TeV (open circles:without LPM, solid circles:with LPM).

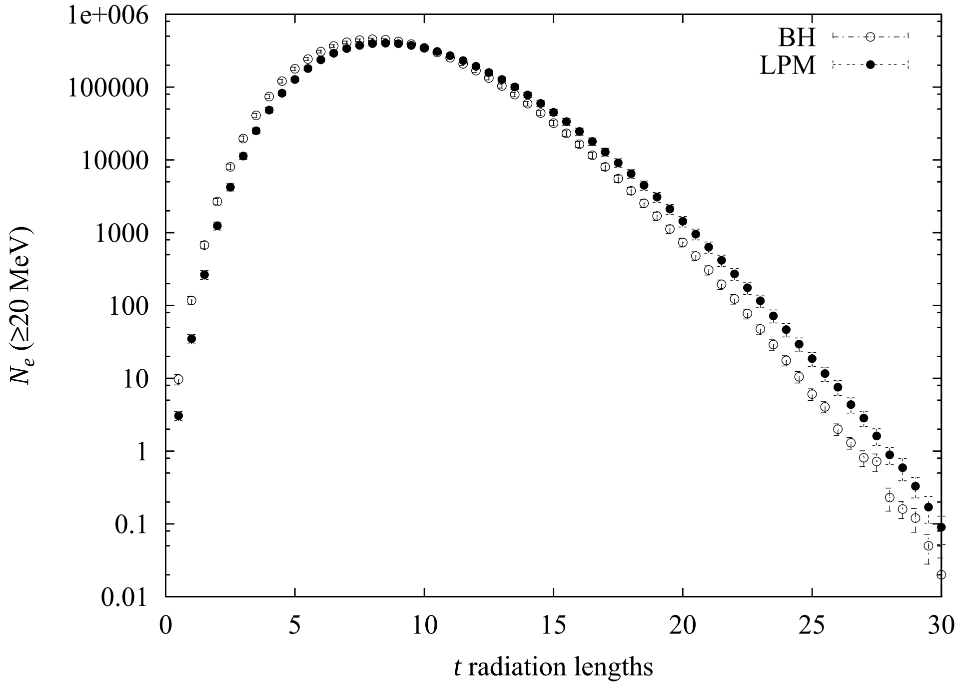

Figure 3: Longitudinal development of photon-induced showers in water for $E_0 = 1000$ TeV and $E_{\rm cut} = 20$ MeV (open circles:without LPM, solid circles:with LPM).

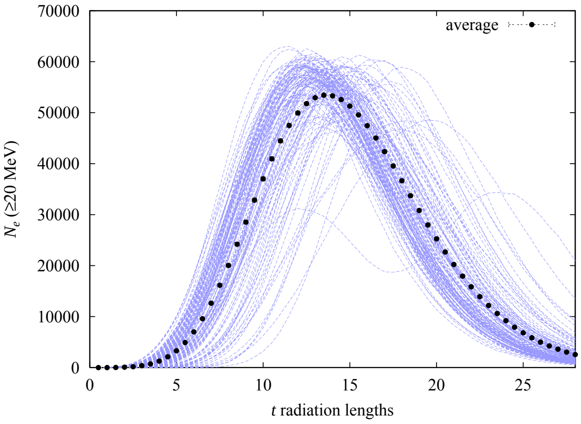

Figure 4: Longitudinal development of photon-induced showers in air for E_0 = 100 TeV and E_{cut} = 20 MeV (left:without LPM, right:with LPM). The lines show the shower profiles for 100 individual showers and the circles show the average profile from 1000 showers.

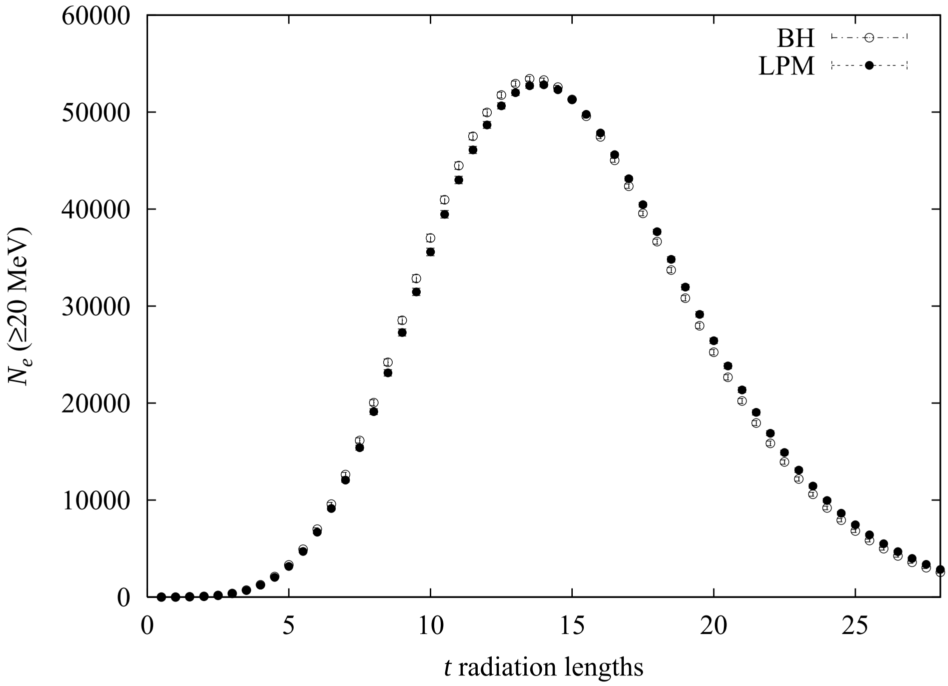

Figure 5: Longitudinal development of photon-induced showers in air for E_0 = 100 TeV and E_{cut} = 20 MeV (open circles:without LPM, solid circles:with LPM).

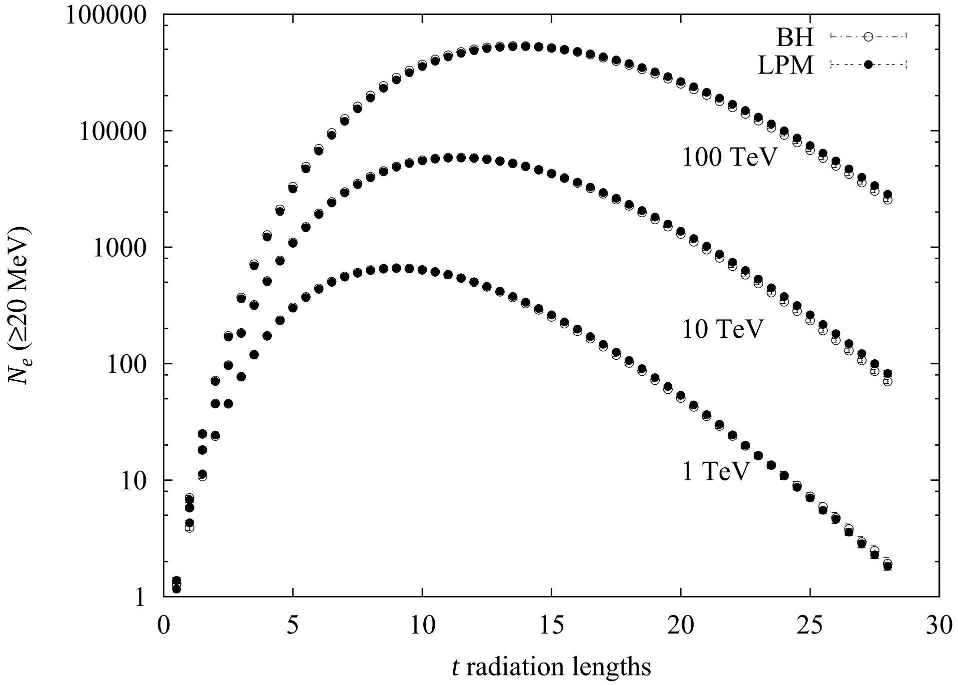

Figure 6: Longitudinal development of photon-induced showers in air for $E_0 = 1$, 10, 100 TeV and $E_{\rm cut} = 20$ MeV (open circles:without LPM, solid circles:with LPM).

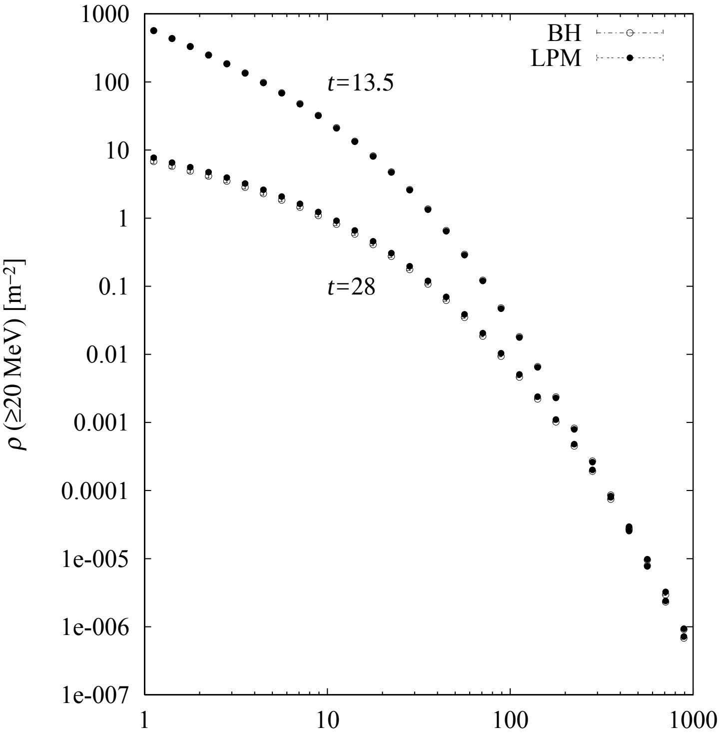

Figure 7: Lateral distribution of photon-induced showers in air for $E_0 = 100$ TeV and $E_{\rm cut} = 20$ MeV (open circles:without LPM, solid circles:with LPM).

In the current implementation of EGS5, the LPM effect is simulated using the rejection method with the ratio $\sigma_{\rm LPM}(y)/\sigma_{\rm EGS}(y)$, after a bremsstrahlung photon of fractional energy y is sampled according to $\sigma_{\rm EGS}(y)$. Since this procedure corresponds to simulating bremsstrahlung according to $\sigma_{\rm LPM}(y)$ (or to $\sigma_{\rm BH}(y)$ for y's where the LPM effect is negligible), the above mentioned difference may arise.

To test this, we modified the rejection method to use the ratio $\sigma_{\rm LPM}(y)/\sigma_{\rm BH}(y)$ so that the modified code simulates bremsstrahlung according to $\sigma_{\rm LPM}(y)\cdot\sigma_{\rm EGS}(y)/\sigma_{\rm BH}(y)$. Because $\sigma_{\rm LPM}(y)/\sigma_{\rm BH}(y)$ approaches 1 as y approaches 1, this procedure corresponds to simulating bremsstrahlung according to $\sigma_{\rm EGS}(y)$ for y's where the LPM effect is negligible. Figure 8 is the same as figure 5 but added the average shower profile obtained using the modified version (dotted line). The dotted line agrees well with the open circles and the difference between the open and solid circles can be explained by the difference between $\sigma_{\rm BH}(y)$ and $\sigma_{\rm EGS}(y)$.

Because the difference between $\sigma_{\rm LPM}(y)$ and $\sigma_{\rm LPM}(y) \cdot \sigma_{\rm EGS}(y)/\sigma_{\rm BH}(y)$ is of the order of a few percent, the modified version may be preferred for internal consistency between simulations with and without the LPM effect.

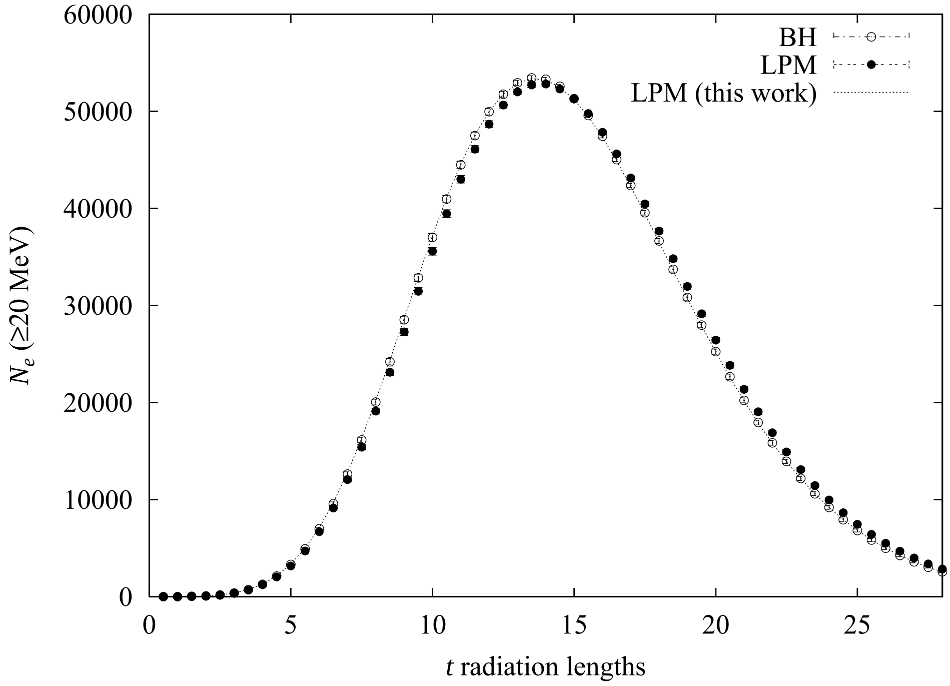

Figure 8: Longitudinal development of photon-induced showers in air for $E_0 = 100$ TeV and $E_{\rm cut} = 20$ MeV (open circles:without LPM, solid circles:with LPM, dotted line: this work).

References

[1] H. Hirayama et al., *SLAC-R-730*, (2005)

[2] W. R. Nelson, H. Hirayama, and D. W. O. Rogers., *SLAC-265*, (1985)

[3] Y. Kirihara, Y. Namito and H. Hirayama, *Nucl. Instrum. Methods* B **268**, 2426 (2010)

[4] T. Stanev et al., *Phys. Rev.* D **25**, 1291 (1982)

[5] S. Klein, *Rev. Mod. Phys.* **71**, 1501 (1999)

[6] B. Rossi and K. Greisen, *Rev. Mod. Phys.* **13**, 240 (1941)

[7] J. Nishimura, *Handbuch der Physik* **46**, 1 (1967)

APPLICATION AND VALIDATION OF EGS5 CODE TO ESTIMATE DETECTION EFFICIENCIES OF MULTI-CASCADE NUCLIDES

Y.Unno[1, 2], T. Sanami[2, 3], M. Hagiwara[2, 3], S. Sasaki[2, 3], T. Kurosawa[1]

[1]National Metrology Institute of Japan, National Institute of Advanced Industrial Science and Technology, Ibaraki 305-8568, Japan
[2]The Graduate University for Advanced Studies (Sokendai), Ibaraki 305-0801, Japan
[3]High Energy Accelerator Research Organization (KEK), Ibaraki 305-0801, Japan
e-mail: y.unno@aist.go.jp

Abstract

A code treating simultaneous photon emission was developed as a part of EGS5 code in order to take into account the coincidence summing effect of multi-cascade nuclides for detector response calculation, properly. The code calculates energy depositions of regions in a finite geometry according to Monte-Carlo method with randomly sampled decay path based on decay scheme of radionuclides given before starting the calculation. The calculation result of this code was verified through the comparison between with experimentally obtained detection efficiency of a HP-Ge gamma detector for multi-cascade nuclides. This code particularly supports the radioactivity measurement of multi-cascade nuclides.

1. Introduction

Radioactivity measurement was urgently required for the protection of the public because of the accidental discharge of a large amount of radioactive material from the Fukushima Dai-ichi Nuclear Power Plant in March 2011 [1]. In this measurement, the samples have various physical chemistry characteristics and ingredient composition since various sampling methods were adopted in the emergent condition [3]. Before then, radioactivity measurement had been performed with a sample obtained by environmental sampling methods and their preparation according to conventional procedures, e.g., [2], in order to properly estimate the radioactivity on the basis of detection and sampling efficiencies. However, we needed to adopt a flexible sampling method for the emergent measurement technique that we studied [3], [4]. Therefore, alternative sample treatment methods should be considered for the samples that have different characteristics, such as the state, size, shape, and density of the material.

In the measurement after the accident, the radioactivity of Cs-134 and Cs-137 contained in a sample with various shapes and characteristics should be measured properly. This is because they remain dominant in the radioactive discharge after the other relevant nuclides have decayed. To determine their radioactivity, gamma-ray spectrometry is often applied because of the convenience of sample preparation and the weaker dependence on sample characteristics. Nuclide identification by the detection of the photoelectron peak is also used, especially for the preeminent high energy resolution of a high-purity germanium (HPGe) detector. The radioactivity in samples is determined with the following formula:

$$A = \frac{N \times \varepsilon_{pe}}{I_{\gamma}} \times k_{decay} \times k_{self-absorption} \times k_{sum-coincidence}$$

where A is the radioactivity in Bq; N is the collected count rate of the photoelectron peak; ε_{pe} is detection efficiency at the photon energy; I_{γ} is the emission rate of photon with the energy from the identified radionuclide; k_{decay} is the correction factors of the decay between the time of reference and the time of the measurement; $k_{self-absorption}$ and $k_{sum-coincidence}$ are the corrections related to the self-absorption in the sample and coincidence summing effect, which should be considered for a multi-cascade nuclide such as Cs-134. Figure 1 shows a principal decay scheme for Cs-134. In this case, the detection efficiencies of the 796 keV and 605 keV photons, which are often used for the radioactivity determination, are affected by the coincidence summing effect. The contribution of the coincidence summing effect also varies with the geometrical orientation of the sample to the detector. Furthermore, the self-absorption varies with the characteristics of the sample mentioned above.

In this study, we developed the simulation code for simultaneous photon emission to estimate these correction factors using the EGS5 code [5]. In our code, the actual nuclear decay data [6] are used to obtain photon emission rate along with the sample characteristics. The outline of calculation procedure was described. The results of the code were compared with experimental results of detection efficiencies for a typical HPGe detector setup.

2. Methodology

2.1 Algorithm for simultaneous photon emission

Figure 2 shows a schematic block diagram of the algorithm for simultaneous photon emission developed as a part of the EGS5 code. In the repeated loop "Call Shower," simultaneous gamma-ray emission is simulated with the nuclear decay data. We regarded one execution of the loop as a single decay from a parent nuclide to a daughter nuclide. The algorithm calculates energy deposition of finite cell. At first step, the source position was randomly determined in a source region, which is retained in one execution. This means we assumed that the emission of all the photons during a single decay would occur at the same position. The directions of the each photon emissions were sampled randomly without correlation among the photons.

Subsequently to the source position determination, a decay branch from the parent nuclide was randomly selected according to the branching ratio taken from the nuclear decay data that was stored in memory at prior to start the loop. Based on the data, the photon energy was selected randomly from the possible branches of the excited level. The "Call shower," process was executed with the photon energy, direction and source position. The process was repeated until reaching to the ground level. The deposited energies for all the photons are stored in memory. By using the algorithm, the detection efficiency of multi-cascade nuclide can be obtained from the number of photo electron peak events with taking into account the coincidence summing effect.

Figure 3 shows a simple example of the numbering configuration of the nuclear decay scheme. The numbers of all the levels are labeled in descending order of the excited energy. A current process level is denoted by the sum of the numbers of the previous level and the decay path. The number of a decay path indicates how many levels the path jumps over. If the result of the summation equaled the number of the ground level, the particular process proceeded to termination.

All the possible decay branches and decay paths from the parent nuclide and the excited level were correspondingly input in advance. The photon energies are labeled with the corresponding decay paths. The inputs did not only include the principal decay branches and decay paths but also the minor ones.

2.2 Measurement instruments for validation

The calculation results of the algorithm were compared with experimental data for photo electron peak efficiency obtained with some measurement instruments described here. A p-type coaxial HPGe detector the germanium crystal size of which is 90 mm in diameter and 100 mm in length was employed for gamma-ray spectrometry. The relative detection efficiency at 1.33 MeV of the Co-60 to NaI(Tl) detector (length and diameter of 3 in each) was specified as 130%. The detector was placed in a heavy lead shield. The pulse height signals from a preamplifier were shaped and properly amplified and we obtained the pulse height spectra with a multi-channel-analyzer. The net count rates of the photoelectron peaks were also calculated by a baseline fitting process.

We used a gamma-ray volume calibration source that was traceable to comply with national metrological standards [7]. The radioactive source, which was made of alumina powder, was put in a 100 cm^3 polypropylene cup known as a U8-type container. The contained nuclides, in ascending order of photon energy, were Cd-109, Co-57, Ce-139, Cr-51, Sr-85, Cs-134, Cs-137, Mn-54, Y-88, and Co-60. The nuclides were chosen considering the efficiency calibration in the wide energy range. The multi-cascade nuclides among them were Cs-134, Y-88, and Co-60. The contained radioactivity of each nuclide was several hundreds of becquerels with an uncertainty of 4.5–5.3% (the value of the coverage factor k was 2). The source was immovably set on top of the end cap of the HPGe detector with a specific jig.

The simulation geometry in the EGS5 code was based on the specifications of the detector and the U8 container obtained from the manufacturer and references [7], respectively. We made minor adjustment to the geometry of the calibration, particularly that of the dead layer in the germanium crystal, which is strongly associated with the curve in the profile of the efficiency around the peak of the energy range.

3. Results

Figure 4 shows the gamma-ray spectra obtained for (a) the Cs-134 and Cs-137 of the contained source and (b) the other nuclides of the contained source. Several photoelectron peaks were observed with preeminent energy resolution. The full width at half-maximum (FWHM) at 661.7 keV for Cs-137 was 1.8 keV. We decided to treat 605, 796, and 802 keV as the peaks in the photoelectron decay of Cs-134. The count rate of each peak was several counts per second. The measurement was repeated at almost one month intervals during a year. The repeatability over the period was estimated at 0.5% (k = 1) on the basis of the count rates at 661.7 keV for Cs-137.

Figure 5 shows the detection efficiencies obtained by the experiment (E) in comparison with calculation results (C). The calculation results are in good agreement with experimental results within the uncertainty of the calibrated source. The differences evaluated from $1 - C/E$ were within $\pm 3\%$ over the entire photon energy range including one for multi-cascade nuclides. Therefore, the algorithm calculates energy deposition properly with taking account effect due to multi-cascade gamma.

The dotted line in Fig.5 indicates the detection efficiencies obtained by calculation over consecutive photon energy. The line connects experimental points smoothly except for one of multi-cascade nuclides. The correction factor for coincidence summing effect was estimated from the ratio of the calculated efficiency with multi-cascade to the value on the line for the same energy.

4. Conclusions

A new algorithm to process simultaneous photon emission was developed as a part of the EGS5 code. The code was validated by the good agreement of the results of its calculations with those obtained experimentally using a calibrated source. This technique is quite useful for estimating detection efficiency because the calculation can be performed for other nuclides and samples with characteristics different from that of the calibration. For example, we adapted the algorithm to estimate the detection efficiency for I-132, which has a high excitation level [3]. We also found that a very complicated multi-cascade was treatable with the algorithm. This emphasized a benefit of the Monte-Carlo simulation, which is its flexibility in handling multiple geometric conditions. This enables us to calculate the efficiency in various situations and for diverse samples, e.g., paper filter, soil, and food. We can freely set a parameter of the sample relevant to the detection efficiency, such as the composition, density, geometric orientation, and distance.

We project that the code could be expanded to simultaneous emission of beta and gamma rays. It could be utilized in the development of radioactivity measurement with the 4πβ–γ coincidence counting method [8].The additional code treating beta-ray emission would be implemented between the fixing steps of the "decay branch from the parent nuclide" and the "decay path from the excited level." This could be used to estimate the prospective performance of a planning detector by considering the fundamental detection property of beta rays.

Acknowledgments

We express our gratitude to Dr. Yamada of the Japan Radioisotope Association and the members of NMIJ/AIST and KEK for supporting this study. This work was funded by JSPS KAKENHI Grant Number 24686106.

References

1) Nuclear Emergency Response Headquarters in Government of Japan, "Report of the Japanese Government to the IAEA Ministerial Conference on Nuclear Safety - The Accident at TEPCO's Fukushima Nuclear Power Stations" (2011)
2) Ministry of Education, Culture, Sports, Science and Technology, A series of methods to radioactivity measurement, http://www.jcac.or.jp/series.html
3) Y. Unno, A. Yunoki, Y. Sato, Y. Hino, "Estimation of immediate fallout after Fukushima NPP accident with HPGe detector using EGS5 code", *Applied Radiation and Isotopes* (To be published)
4) Homepage of Advanced Industrial Science and Technology, "The results of ionizing radiation dose survey, Radiation Activity Fallout Measurement", http://www.aist.go.jp/aist_e/taisaku/en/measurement/index.html
5) H. Hirayama, Y. Namito, A.F. Bielajew, S.J. Wilderman, W.R. Nelson, "The EGS5 code system", SLAC-R-730 (2005)
6) R.B. Firestone, V.S. Shirley, C.M. Baglin, J. Zipkin, S.Y. Frank Chu, "Table of Isotopes", Eighth edition (1996)
7) T. Yamada, Y. Nakamura, "Examination of the U8 type polypropylene container used for radioactivity standard volume sources", *Radioisotopes* **54** 105-110 (2005)
8) Y. Unno, T. Sanami, M. Hagiwara, S. Sasaki, A. Yunoki, "Application of beta coincidence to nuclide determination of radioactive samples contaminated by the accident at the Fukushima Nuclear Power Plant", *Progress in Nuclear Science and Technology* (To be published)

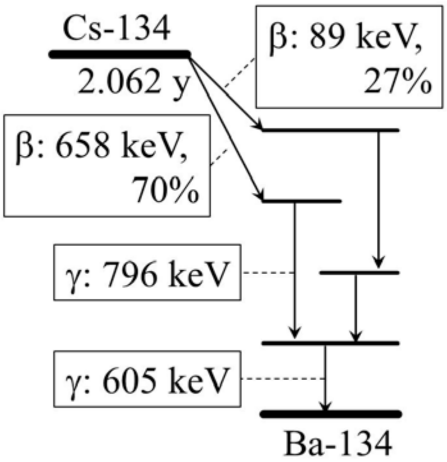

Figure 1. Principal decay scheme of Cs-134

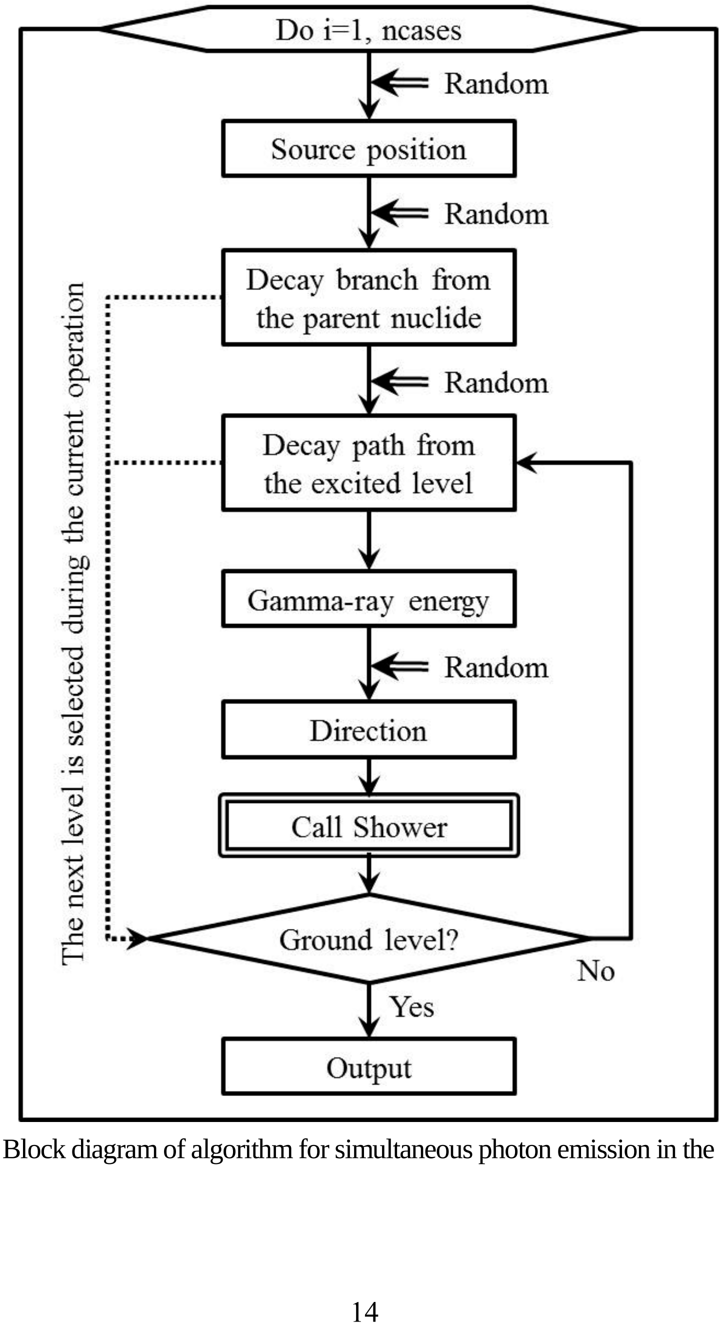

Figure 2. Block diagram of algorithm for simultaneous photon emission in the EGS5 code

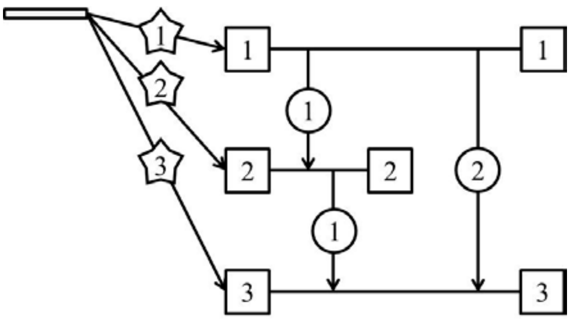

Figure 3. Numbering configuration of the nuclear decay scheme

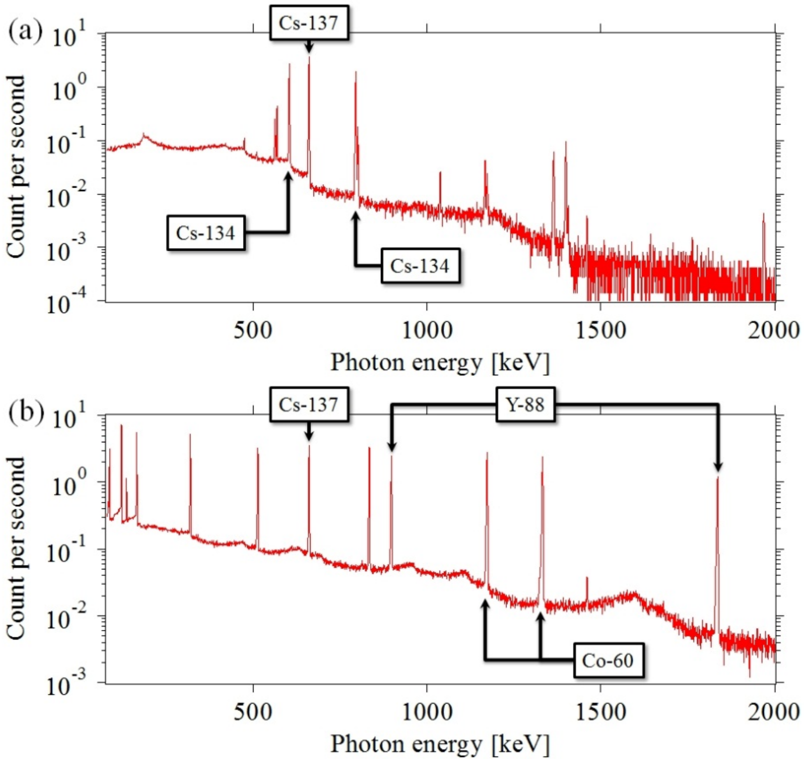

Figure 4. Gamma-ray spectra obtained using the HPGe detector: (a) Cs-134 and Cs-137, (b) Cd-109, Co-57, Ce-139, Cr-51, Cs-137, Mn-54, Y-88, and Co-60.

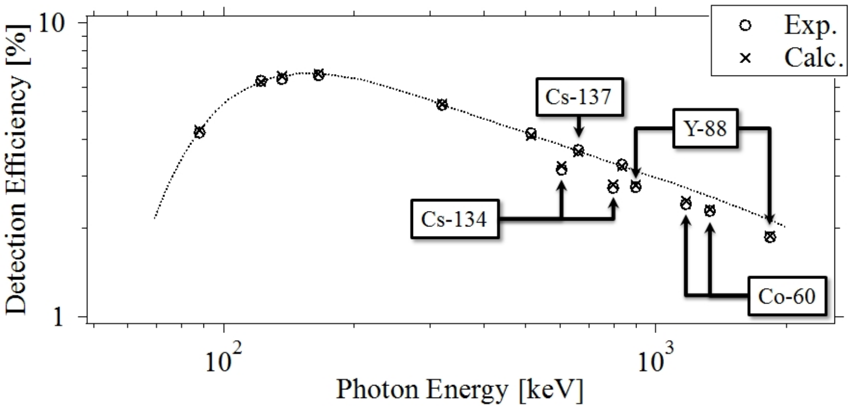

Figure 5. Comparison of the gamma-ray detection efficiencies of the experiment and the calculation

Verification of Pin-photo Diode Detector Characteristics Using EGS5

S. KONDO[1], T.HABA[1], D.HAYASHI[1], H.NUMAMOTO[1], T.ISHII[1], S.KOYAMA[1]

[1]Department of Radiological Technology, Graduate School of Medicine, Nagoya University
1-1-20 Daiko-Minami, Higashi-ku, Nagoya 461-8673, Japan
e-mail: kondo.shimpei@e.mbox.nagoya-u.ac.jp

Abstract

We developed a novel X-ray beam analyzing system with eight sensors using commercially available pin silicon photodiodes to estimate the effective energy and intensity of incident X-ray in each angle undergoing computerized tomography (CT). The aim of this study was to verify characteristics of photodiodes of X-ray beam analyzing system in a diagnostic energy region using Electron Gamma Shower ver.5 (EGS5). X-ray energy and angular dependence were assessed for the X-ray beam analyzing system by irradiating one of eight sensors, and which were also calculated by EGS5 under the same conditions as those considered during the measurement. Measurement results is that the output value of photodiode was correlated with any effective energy of incident X-rays, which suggested that when a sensor in the X-ray beam analyzing system is irradiated, the system can estimate the effective energy of the incident X-rays. X-ray energy and angular dependence calculated by EGS5 are in good agreement with measurement, which can be helpful in further experiments. In this study, the characteristics of photodiodes of X-ray beam analyzing system were obtained through measurement experiment, and were verified by EGS5. X-ray beam analyzing system can accurately estimate the effective energy of any incident X-rays which has any maximum energy and the shape of X-ray energy spectra.

1. Introduction

An Electron Gamma Shower (EGS) is a very useful tool used widely in X-ray computerized tomography (CT) simulations to calculate a patient's exposure to radiation [1, 2]. X-ray dose distribution and energy information in an X-ray fan beam are essential in X-ray CT simulation. An X-ray CT scanner is generally equipped with a beam-shaping filter in front of the X-ray tube radiation window, and it is troublesome and time-consuming to measure the X-ray intensity and effective energy of the X-ray at each angle of the X-ray CT fan beam by using an ionization chamber [3]. We developed a novel X-ray beam analyzing system with eight sensors using commercially available pin silicon photodiodes (S2506-04; Hamamatsu Photonics, Hamamatsu, Japan) shown in Fig. 1 [4]. A sensor consists of two photodiodes stacked one on top of the other. The voltages corresponding to radiation doses are outputted from the eight pairs of photodiode sensors when the sensors are irradiated. The effective energy of the incident X-rays is calculated from the ratio of the output voltage of the upper sensor to that of the lower sensor. Several X-ray spectra with different maximum energies and beam qualities are used in a diagnostic energy region. In practice, it is difficult to verify the characteristics of the sensor for a large variety of X-ray spectra. In this study, the characteristics of the sensors in the X-ray beam analyzing system were verified using EGS ver. 5 (EGS5).

2. Materials and Methods

2.1 Measurement

X-ray energy and angular dependence of the ratio of the output voltage were assessed for the X-ray beam analyzing system by irradiating one of eight sensors. Experiments were carried out in free air using medical radiography X-ray equipment with an X-ray tube having 2.2-mm Al inherent filtration. Dose readings from the system were calibrated using a Radcal 1015 dosimeter (Radcal, Inc., Monrovia, CA) with an attached 6-cm^3 ionization chamber placed adjacent to the sensor. The X-ray energy dependence on the ratio of the output voltages was measured at tube voltages in the range 40–120 kV with 10 kV intervals and additional Al filters (0–40 mm thick) to change the beam quality. X-ray irradiation was carried out with focus-to-sensor distances (FSD) of 200 cm. The angular dependence of the ratio of the output voltages was measured for an X-ray tube voltage of 120 kV as the CT tube voltage.

2.2 Calculation using EGS5

For verification, X-ray energy and angular dependence on the output voltage ratio were simulated using EGS5 under the same conditions as those considered during the measurement. Geometric data for the EGS5 calculation of X-ray energy and angular dependence were created using Combinatorial Geometry View (CGVIEW) such that they accurately followed the experimental conditions. Figures 2 and 3 show the geometry of the sensor, which consisted of silicon photo-sensitive elements, polyethylene packages for the photodiode, iron under the silicon, a Bakelite plate, a brass plate for cutting off back scattering, a polymethylmethacrylate (PMMA) plate, and aluminum foil covering the sensor to keep out visible light. Several incident X-ray spectra modeled by Tucker et al. in 1991 [5] were used in this calculation, which were determined by the maximum energy and half-value layer of the X-ray energy, as shown in Table 1 and Fig. 4. The output voltage of the photodiode for the measurement was proportional to the energy deposition on the silicon in the calculation. The ratio of the energy deposition between the upper silicon and the lower silicon corresponding to the effective energy of the incident X-rays was obtained from the X-ray energy and angular dependence calculation, and then compared with the results of the measurements. The number of incident photons was 1.6×10^9. The standard error in the energy deposition on the silicon was less than 1.0% in this calculation.

3. Results

The X-ray energy dependence of the ratio of the photodiode output value, a comparison of measurement, and calculation results, are shown in Fig. 5. This graph simply indicates that the ratio of the output value increases with the effective energy of the incident X-rays. This graph demonstrated good agreement between the measurements and calculations; however, there was a slight difference for effective energies in the range 50–70 keV. Figures 6 (a) and (b) show the results of measurement and calculation of the angular dependence of the sensors. The shape of the output value curve from the upper photodiode is similar to the measurement and calculation at any angle, and the same is true of the lower photodiode. The ratio of the upper diode voltage to the lower diode voltage indicated the same ratio from 0 to ±15° in both results. This means that the effective energy of incident X-rays can be measured correctly with less than 15° of angular error by a sensor in the X-ray beam analyzing system.

4. Discussion

The output voltage is correlated with the effective energy of incident X-rays in Fig. 5. This correlation suggests that when a sensor in the X-ray beam analyzing system is irradiated, the system can estimate the effective energy of the incident X-rays from the ratio of the output voltages using an approximated curve function given the X-ray energy dependence measurement results in Fig. 5. There is a slight difference between measurement and calculation across an effective energy of 50–70 keV. This is because the iron plate in the photodiode simulated by CGVIEW was slightly thicker than the iron plate in an actual photodiode. The iron is absorber to create a difference of the upper and lower photodiode voltage. The difference between measurement and calculation, however, was not a major drawback, and it is important that the correlation between the output voltage and the effective energy of the incident X-rays was also confirmed in the EGS5 calculation. In addition, the angular dependence calculated by EGS5 was in good agreement with the measurements, and thus, the geometric arrangement for the calculation was correctly simulated. This result can be helpful in further experiments.

5. Conclusions

The characteristics of a sensor in the X-ray beam analyzing system was obtained through experimental measurement and verified by EGS5 calculation. The correlation between the sensor output and the effective energy of the incident X-rays was clearly confirmed. This X-ray beam analyzing system can accurately estimate the effective energy of any incident X-rays.

References

1) T. Haba, S.Koyama, “Detail analysis of dose distribution in phantom in X-ray CT using EGS5,” KEK Proceedings **18**, 58-61 (2011)
2) Y. Morishita, S.Koyama, “Estimation of Patient Exposure Doses Using Anthropomorphic Phantom Undergoing X-ray CT Examination,” KEK Proceedings **17**, 82-88 (2010)
3) Randell L. Kruger, Cynthia H. McCollough, Frank E. Zink, “Measurement of half-value layer in x-ray CT: A comparison of twononinvasive techniques,” Med. Phys. **27**, 1915-1919 (2000)
4) T. Aoyama, S. Koyama, C. Kawaura, “An in-phantom dosimetry system using pin silicon photodiode radiation sensors for measuring organ doses in x-ray CT and other diagnostic radiology,” Med. Phys. **29**, 1504-1510 (2002)
5) M. Tucker, G. Barnes, D. Chakraborty, “Semiempirical model for generating tungsten target x-ray spectra,” Med. Phys.**18**, 211-218 (1991)

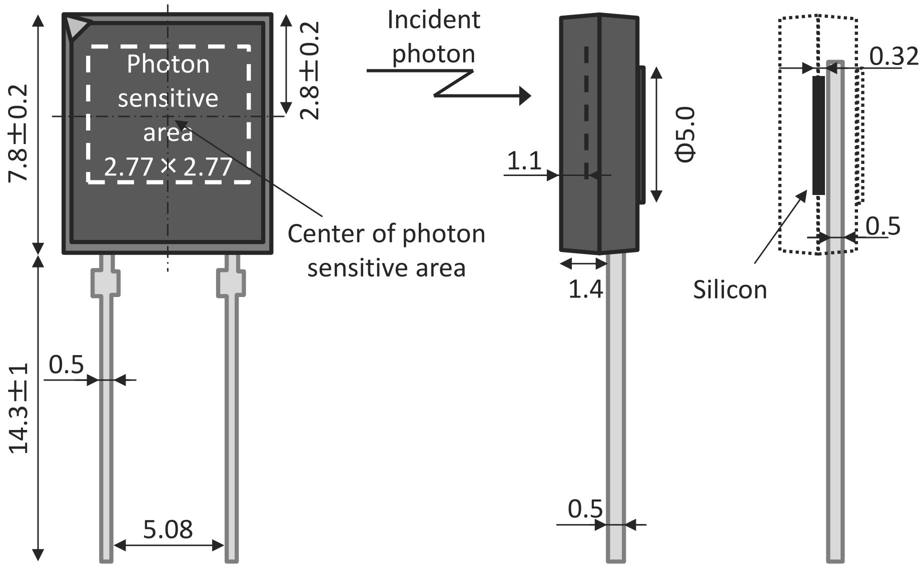

Fig.1 Dimensional outline of photodiode (Unit: mm)

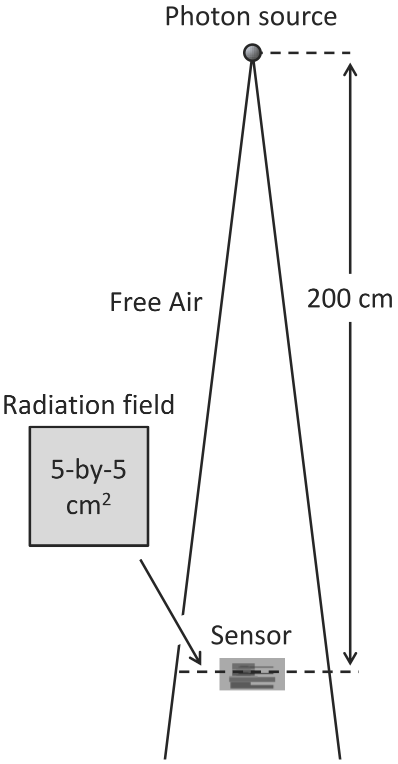

Fig.2 Experimental condition

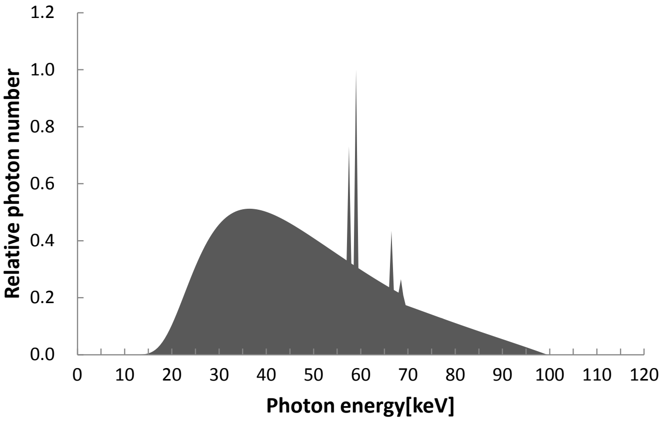

Fig.4 Example of X-ray energy spectrum (Tube voltage; 100 kV, Effective energy; 35.3 keV)

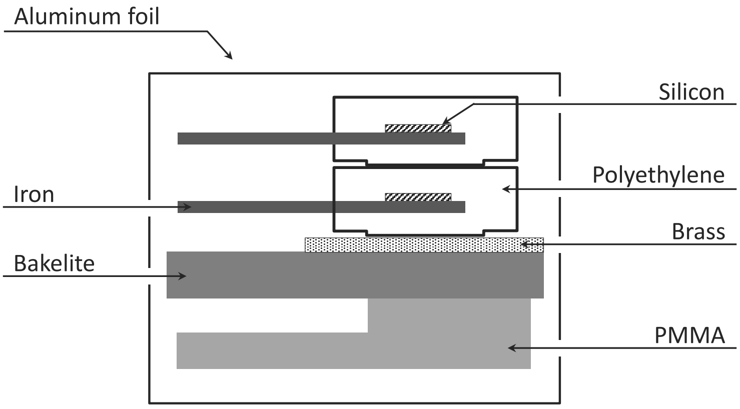

Fig.3 The geometry of sensor

Table 1 Continuous incident X-ray spectrums using EGS5

Tube Voltage [kV]	Effective energy [keV]
40	24.7
50	27.5
60	29
70	30.7
80	32.7
	38
	42
	48
	52
90	34.3
100	35.3
	35.7
	42
	47
	53.5
	58.3
110	38
120	38.5
	46
	51
	58.3
	63.5
	67.3
	71.5

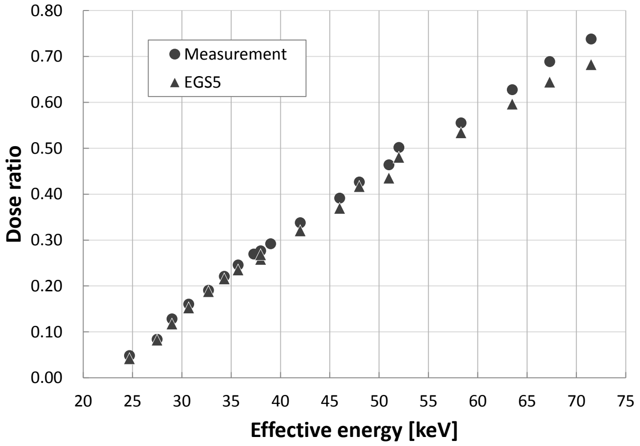

Fig.5 The X-ray energy dependence of the ratio of the photodiode output value; a comparison of measurement and calculation results,

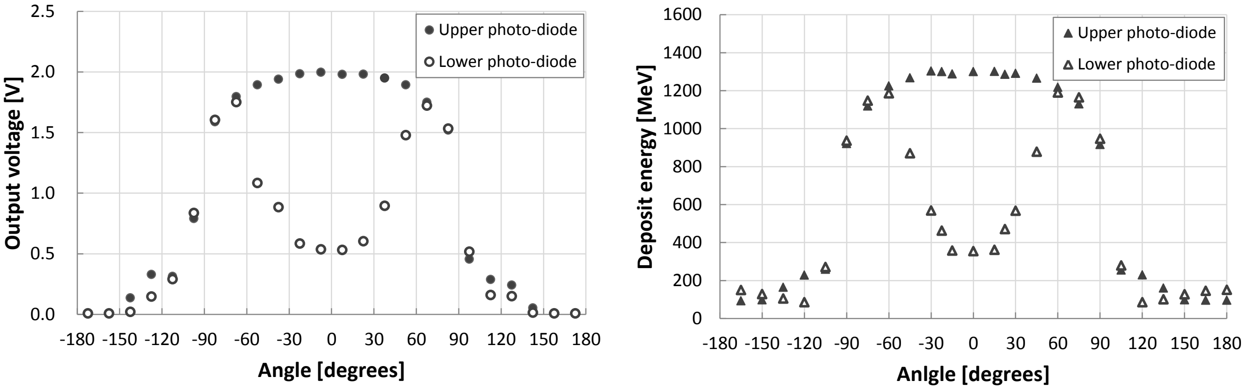

(a) (b)

Fig.6 Angular dependence, (a) is measurement and (b) is calculation.

Influence of the gamma camera collimator geometry on quantitative values

H. Yoshino, S. Hayashi, Y. Okura and M. Yamamoto
Hiroshima International University, Higashi-Hiroshima, Hiroshima 739-2695, Japan

Abstract

A standardized collimator gauge for gamma cameras has not been developed. However, patients expect that examinations conducted at one hospital should be comparable with those in another. We used the Monte Carlo simulation(EGS5 code) to estimate the heart-to-mediastinum count ratio (H/M ratio) measured by ^{123}I-metaiodobenzylguanidine myocardium scintigraphy with various collimator wall thicknesses. The H/M ratio varied depending on the thicknesses of the collimator wall.

1 Introduction

Gamma camera collimators used in diagnostic nuclear medicine vary depending on the manufacturer. However, a standardized collimator gauge has not yet been developed prepared. The variations in collimators influence quantitative values. which prevent patients from comparing values obtained at different facilities or from different collimators. It is desirable to ascertain the reliability of comparing quantitative values obtained from gamma cameras or collimators for the same patient.

The purpose of this study was to estimate the heart-to-mediastinum count ratio (H/M ratio) measured by ^{123}I-metaiodobenzylguanidine (^{123}I-MIBG) myocardium scintigraphy using the Monte Carlo simulation(EGS5 code) and to quantitatively clarify the effect of collimator differences on image quality.

Collimator design parameters include the thickness of the collimator wall and the shape and the diameter of the hole. Differences in these parameters can affect the number of the photons passing through the collimator, and the H/M ratio. In this study, we simulated the changing in H/M ratios as the collimator wall thickness varied.

2 Methods

2.1 Geometry of the simulation

Figure 1 shows the whole geometry of the simulation. To simulate the body, we used water in a 15 × 30 × 30 - cm rectangular container. To simulate the heart, we used half a rugby ball placed at the position indicated by the circle. A 20 × 20 - cm plane was used as a background region placed at the position indicated by the line. We sequentially placed a 4 cm thick Pb, a 1 cm thick NaI and a 2 cm thick Al plates to represent a collimator, a scintillator and a photomultiplier, respectively, 1 cm apart and away from the body. The parallel hall collimator was used and the collimator holes were hexagonal and positioned as shown in Figure 2. The diameter of the holes was set at 2.5 mm, and the thickness of the collimator wall varied from 0.25 mm to 1.00 mm. The base of the 12.5 × 12.5 - cm square scintillator was divided into an array of 32 × 32 regions, and the number of photons in each region was counted.

2.2 Sources

The incident energy of the photons, E_i, was set at 159 keV and 4×10^5 photons were emitted from the heart region. The source were positioned randomly in the region, and the incident angle of the emitted photon beam was less than 30 degree from a line which was perpendicular to the scintillator.

The number of photons emitted from the background region was 1.6×10^5, and the other parameters were the same as those given for the heart region.

3 Results

The distribution of the number of the photons emitted by the scintillator is shown in Figure 3; these are the planar ^{123}I-MIBG images. A circular region of interest(ROI) was drawn over the entire heart. A rectangular ROI over the mediastinum was used as the background. The ratio of those two areas is approximately $1.9 - 1.0$. The diameter of the holes was set at 2.5 mm, and the thicknesses of the collimator wall were 0.25, 0.50, 0.75 and 1.00 mm. We can see that the color is lighter as the collimator wall is thicker, because the number of incident particles was the same.

The number of counts in each ROI and the H/M ratio are shown in Table 1. For reference, the central processing unit time was approximately 11.5 hours/10^5 incident particles. The H/M ratio depended on the thickness of the collimator wall. Figure 4 shows the relationship between the collimator wall thickness and the H/M ratio. In this figure, we can see that the H/M ratio peaks between collimator wall thickness of $0.5 - 0.6$. Further studies are necessary to determine if this relationship is valid, but it is very interesting to speculate why a peak might exist. We tried to represent it by a quadratic function, and obtained the relation below.

$$\mathrm{H/M} = 2.8 + 1.0t - 0.8t^2 \tag{1}$$

Further studies are required to consider if a quadratic function is appropriate to represent this data.

4 Conclusion

We used the Monte Calro simulation (EGS5 code) to obtaine the gamma camera planar images for various collimator wall thicknesses. The H/M ratio for each collimator wall thickness were estimated from the planar images. The relationship between the H/M ratio and the collimator wall thickness showed a peak at a collimator wall thickness 0.6 mm; however, further studies are required to confirm this result including the form of the fitted function. The effect of other collimator parameters such as the hole diameter, hole shape and collimator thickness on the H/M ratio varies are also require further clarification.

Table 1: The collimator wall thickness, the photon counts for each region of interest and H/M ratios.

Collimator wall thickness (mm)	Counts heart ROI	Count mediastinum ROI	H/M ratio
0.250	65201	21554	3.025
0.375	28521	9284	3.072
0.500	53540	16960	3.157
0.625	23161	7364	3.145
0.750	44537	14240	3.128
0.875	21183	6832	3.101
1.000	38567	12600	3.061

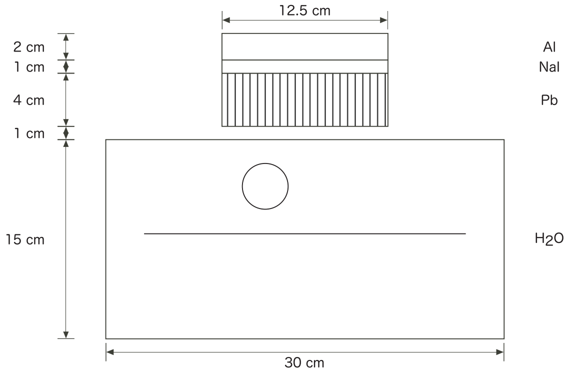

Figure 1: Geometry of the entire system.

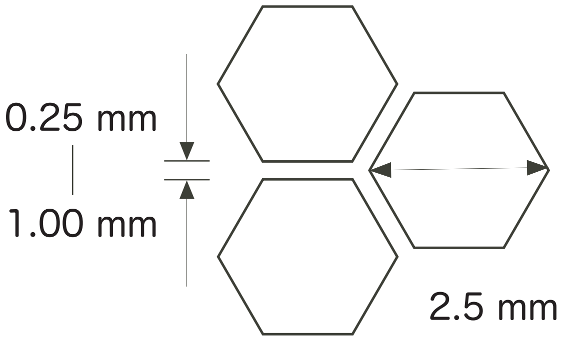

Figure 2: Hole shape, hole diameter and collimator wall thickness.

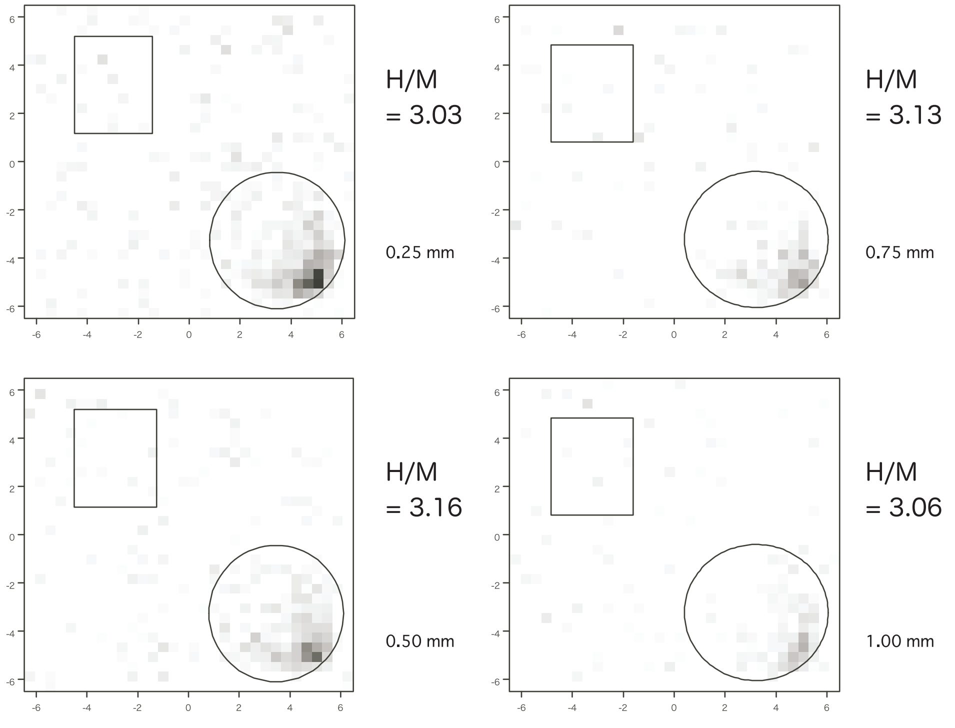

Figure 3: Planar images for various collimator wall thicknesses.

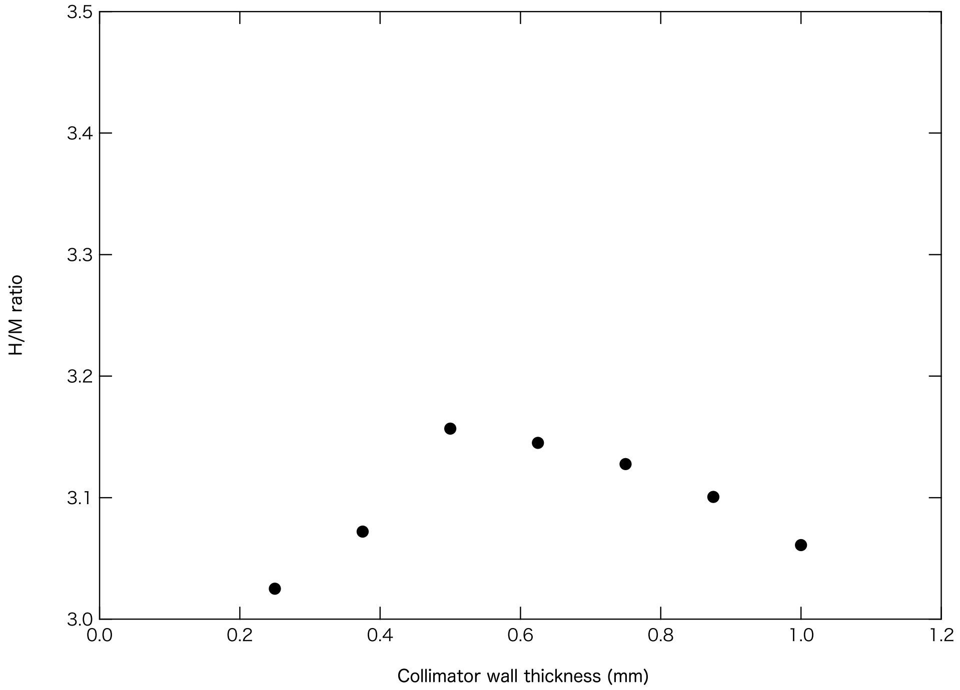

Figure 4: The relationship between collimator wall thickness and H/M ratio.

X-ray Computed Tomography in Consideration of the Influence of Scattered Radiation

Kazuma Takemoto, Kenta Tokumoto, Yoichi Yamazaki, Naohiro Toda
Information and Computer Sciences, Aichi Prefectural University

Abstract

In the conventional X-ray CT (computed tomography) that uses a fan-shaped X-ray beam (fan-beam), since the content ratio of scattered radiation is low, the influence of scattered radiation is believed to be small. In recent years, cone-beam geometry is being adopted, and the content ratio of scattered radiation increases with an increase in cone angle. However, conventional image reconstruction methods hardly deal with scattered radiation because of problems such as computational complexity. Therefore, in cone-beam CT, when the conventional image reconstruction method is used, the influence of scattered radiation appears in a reconstructed image as an artifact. In this study, Monte Carlo simulation implemented in EGS5[2] is employed for image reconstruction. Presuming the existence of scattered radiation, we propose an image reconstruction algorithm based on successive optimization to minimize I-Divergence[3, 4, 5], which is equivalent to the likelihood function, and show its validity.

1 Introduction

X-ray CT (computed tomography) is a medical diagnostic imaging technique that is used to reconstruct cross-sectional images of an object from X-ray intensities projected by a rotating X-ray source-detector pair. X-ray CT was developed in the 1970s and is still indispensable to medical diagnostics, even though new diagnostic imaging techniques such as SPECT (single photon emission computed tomography), PET (positron emission tomography), and MRI (magnetic resonance imaging) have appeared.

Cone-beam geometry has been adopted in recent years, and the content ratio of scattered radiation increases with an increase in cone angle [1]. However, since the conventional image reconstruction methods use Lambert-Beer's law only, scattered radiation is not taken into consideration sufficiently. Therefore, with cone-beam CT, the influence of scattered radiation may appear in a reconstructed image as an artifact, and it may interfere with medical diagnostics.

High-speed computers have gained popularlity with the progress of related technilogy in recent years, and it has become possible to estimate the influence of scattered radiation by Monte Carlo simulation[1].

In this paper, we propose an image reconstruction algorithm based on successive optimization, which includes a projection simulation using EGS5 (a simulator that performs transport calculation by the Monte Carlo method), and show the validity of the proposed method.

2 Reconstruction Method Under The Presence Of Scattered Radiation

When the conventional image reconstruction method is applied to the measured data containing scattered radiation, the influence of scattered radiation appears in the reconstructed image. In order to solve this, it is necessary to use a reconstruction method reflecting the influence of scattered radiation. Herein, a new iterative technique utilizing the simulation of scattered radiation to improve the accuracy of the reconstructed image is proposed. In this section, we first describe an iterative algorithm that employs I-Divergence as an evaluation function. Furthermore, a new image reconstruction method using EGS5 is proposed.

2.1 Iterative Reconstruction Method Using I-Divergence As An Evaluation Function

Iterative reconstruction using the least-squares method has been introduced since the beginning of CT development. In order to improve the performance of iterative reconstruction, several recent studies have used the likelihood function. Fessler et al.[3] proposed a method that has been applied to dual energy X-ray CT. Furthermore, O'Sullivan used I-Divergence, which is equivalent to the likelihood function, and proposed an improved method [4]. I-Divergence

$$I = \sum_{\tau \in \boldsymbol{T}} p(\tau) \log \frac{p(\tau)}{q(\tau)} - p(\tau) + q(\tau) \tag{1}$$

is employed as a cost function to be minimized, where $\boldsymbol{T}$ denotes a set of scanning position τ. $p(\tau)$ and $q(\tau)$ are determined using the following equations

$$q(\tau) = I_e(\tau) \exp \left[\sum_{\boldsymbol{x} \in L(\tau)} d(\tau, \boldsymbol{x}) \right] \tag{2}$$

$$p(\tau) = q(\tau) \frac{I_m(\tau)}{q(\tau)} \tag{3}$$

where $I_e(\tau)$ is a positive bounded function that denotes the intensity of the emitted X-rays, including the effects of filters and the energy dependency of detectors. Further, $I_m(\tau)$is a measured value, $L(\tau)$ is a projection line at position τ, and $d(\tau, \boldsymbol{x})$ is a weighting function at which the length of the beamline inside the pixel is usually chosen. (2) and (3) are derived from a Poisson random variable.

2.2 Conventional Method

In the conventional method, iterative reconstruction is performed on an initial image x_0 until the behavior of evaluation function (4) relaxes sufficiently.

$$I = \frac{Im(\tau)}{\widehat{Im}(\tau)} - Im(\tau) + \widehat{Im}(\tau) \tag{4}$$

Equation (4) is a specific version of I-Divergence (1), and it consists of the actual measured value $Im(\tau)$ and the calculated value $\widehat{Im}(\tau)$ of the model. The number of iterations is set to 10000.

2.3 Proposed Method

In this section we propose a new method for image reconstruction. The image reconstruction algorithm using Monte Carlo simulation is shown below.

1. Set an initial image x_0.
2. After 1000 itertations, a density map (a distribution of attenuation coefficient of water) is created. Calculate the amount of scattered radiation $\widehat{\beta}(\tau)$ via Monte Carlo simulation using EGS5 and the abovementioned density map.
3. Renew $\widehat{Im(\tau)}$ by $\widehat{Im}(\tau) = Im(\tau) - \widehat{\beta}(\tau)$.
4. Repeat 3 and 4 until the behavior of evaluation function (4) relaxed sufficiently.

Scattered radiation is estimated at every 1000-time update of the image. In this study, we set the upper limit of the total of iterations number to 10000 times. The flow chart is shown in Figure 1.

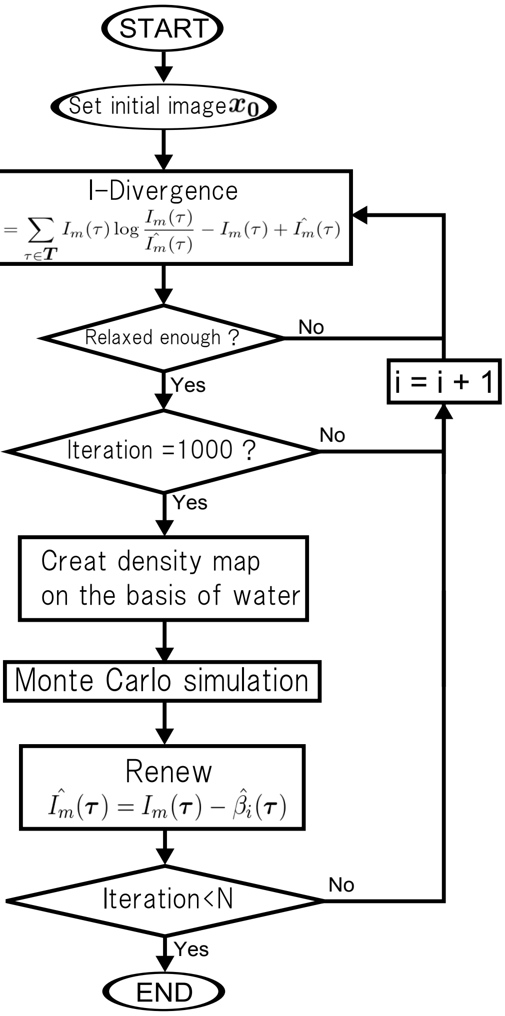

Figure 1: Flow chart of proposed method

3 Numerical Experiments

In this section, we show the validity of the proposed method via numerical experiments.

3.1 Geometry Of Simulation

The number of photons at a single energy of 60 [keV] is set to 10^6, the number of divisions in the rotation angle is set to 128, and the number of NaI detectors is set to 64. The objective space is a rectangle of size 30 [cm] × 30 [cm] × 18.75 [cm]. We prepared three phantoms. Phantom a is shown in Figure 2 (a): a water-filled sphere having a diameter of 22 [cm]. Two spheres having a diameter of 4 [cm] and composed of cortical bone are arranged symmetrically in the water-filled sphere. Phantom b is shown in Figure 2 (b): a water-filled sphere having a diameter of 22 [cm]. Two spheres having diameters of 4 [cm] and 8[cm] and composed of cortical bone are arranged in the water-filled sphere. Phantom c is shown in Figure 2 (c): a water-filled sphere having a diameter of 22 [cm]. A ring-shaped object having a thickness of 2 [cm] and composed of cortical bone is arranged in the water. These are considered as the ideal phantoms.

In the experiments, these phantoms are used after discretizing the space adequately. Phantoms which having 8×8 voxels, as shown in Figure 3, are used. The distance between the X-ray focus and the iso-center is 30 [cm], which is equal to the distance between the detectors and the iso-center. The X-ray tube radiates a cone beam whose fan angle θ and cone angle Φ are 90 [deg] and 5 [deg], respectively, as shown in Figure 4. The geometry is set as shown in Figure 5.

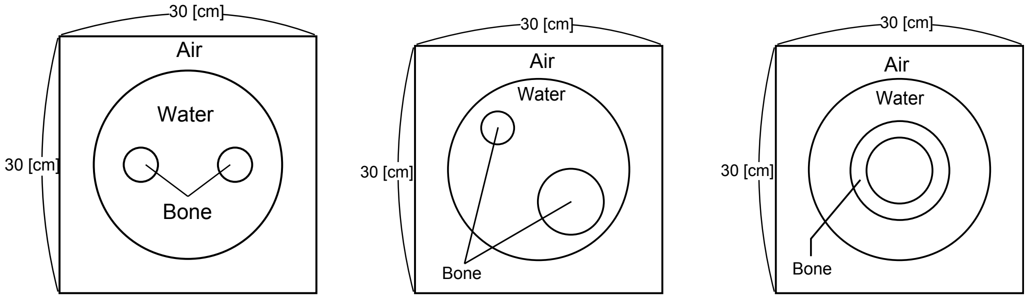

(a) Phantom a (b) Phantom b (c) Phantom c

Figure 2: Ideal phantom

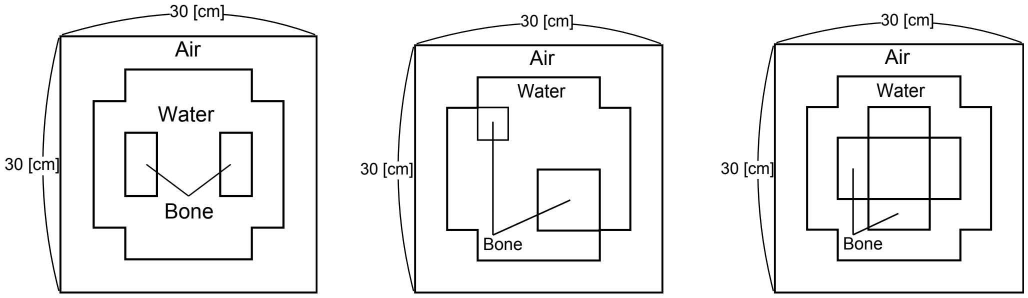

(a) Phantom a (b) Phantom b (c) Phantom c

Figure 3: Phantom of measuring object

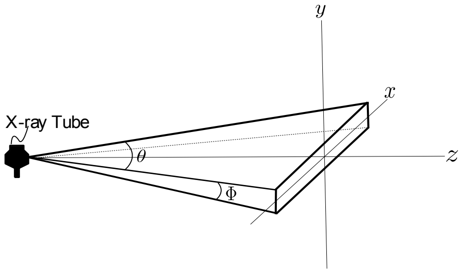

Figure 4: Shape of X-ray beam

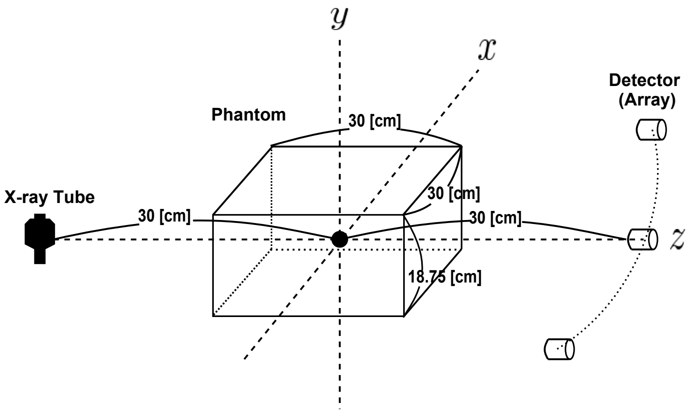

Figure 5: Geometry

3.2 Verification Of Reconstructed Images

In this section, the quality of the reconstructed images obtained with the proposed method and the conventional method is compared. The true image, which indicates the true attenuation coefficient, is shown in Figure 6. We adopt an image (shown in Figure 7) that is reconstructed by the filtered back-projection method using measured intensity and that contains scattered radiation as the initial image.

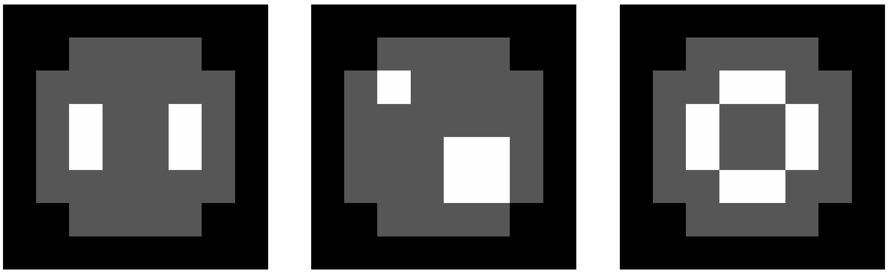

(a) Phantom a (b) Phantom b (c) Phantom c

Figure 6: True reconstruction picture

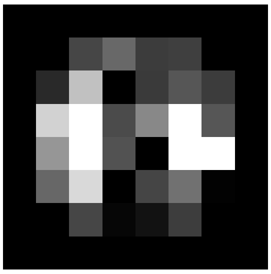

Figure 7: Initial picture

If the proposed method is effective, the reconstruction result of the conventional method for the measured value that does not contain scattered radiation and that of the proposed method for the measured value that contains scattered radiation should be almost equal. The reconstructed image after different numbers of iterations obtained by both the conventional method and the proposed method for each phantom are shown in figures 8-10. In these figures, (a)-(d) indicate the following: (a) shows the desired image reconstructed without scattered radiation, (b) shows the image obtained by the conventional method for the measured value containing scattered radiation, and (c)-(f) shows the image obtained by the proposed method for the measured value containing scattered radiation (different numbers of iterations).

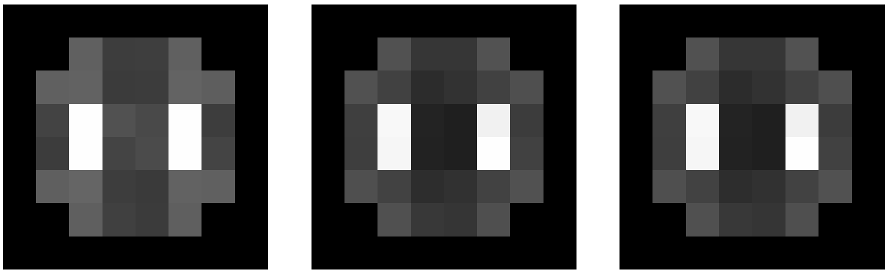

(a) Desired

(b) Conventional method

(c) Proposed method (1000 times)

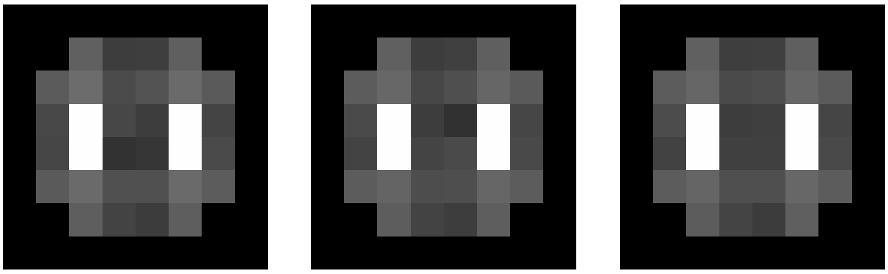

(d) Proposed method (3000 times)

(e) Proposed method (5000 times)

(f) Proposed method (10000 times)

Figure 8: Phantom a

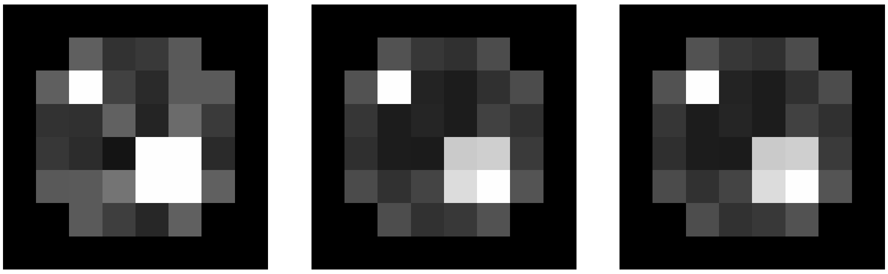

(a) Desired

(b) Conventional method

(c) Proposed method (1000 times)

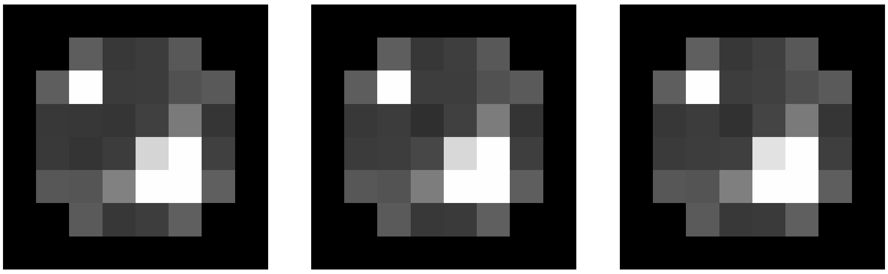

(d) Proposed method (3000 times)

(e) Proposed method (5000 times)

(f) Proposed method (10000 times)

Figure 9: Phantom b

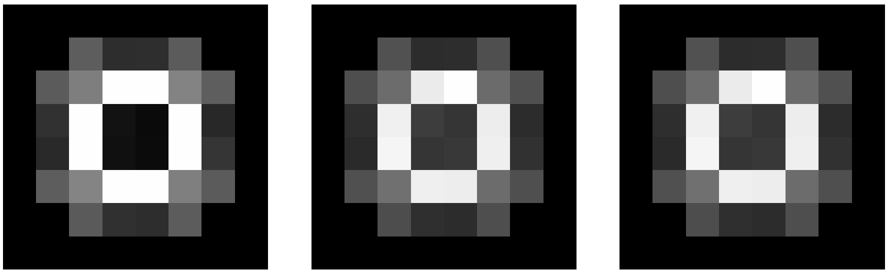

(a) Desired (b) Conventional method (c) Proposed method (1000 times)

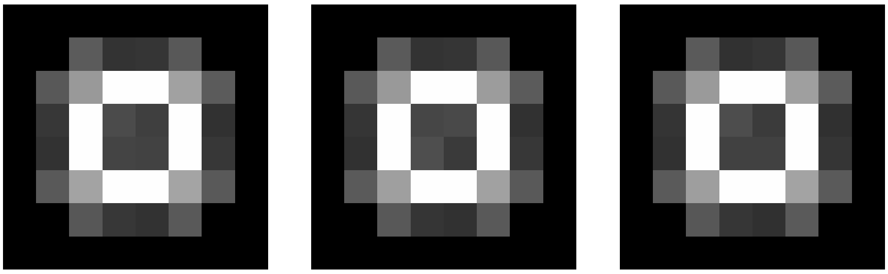

(d) Proposed method (3000 times) (e) Proposed method (5000 times) (f) Proposed method (10000 times)

Figure 10: Phantom c

From figures 8-10, it is observed that as the number of iterations increases, the accuracy of the reconstructed image obtained by the proposed method also increases.

Here, we discuss the above results quantitatively. The actual values of I-Divergence (4) against the number of iterations are shown in Figure 11. In all of the phantoms, it is seen observed as the number of iterations increases, the I-Divergence value decreases. Moreover, the I-Divergence value for the proposed method approaches the ideal value, whereas that for the conventional method does not.

We obtain the true attenuation coefficient from the simulation. The root-mean-square error of the attenuation coefficient is

$$Error = \frac{1}{N}\sqrt{\sum_{i=1}^{N}\frac{(\mu_i - \widehat{\mu}_i)^2}{\mu_i}} \tag{5}$$

which evaluates the quality, where N denotes the number of space division, μ_i denotes the true attenuation coefficient at 60 [keV], and $\widehat{\mu}_i$ denotes the attenuation coefficient obtained by each reconstruction method. Figure 12 shows the error of the attenuation coefficient against the number of iterations.

From Figure 12, for all of the phantoms, it is clearly observed that as the number of iterations increases the error decreases. In addition, the error with the proposed method is lower than that with the conventional method.

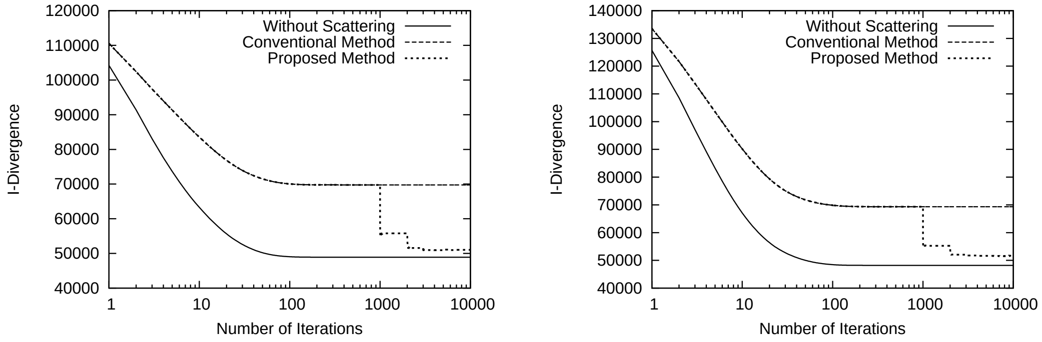

(a) Phantom a (b) Phantom b

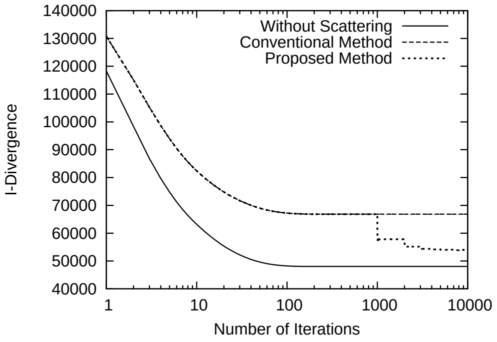

(c) Phantom c

Figure 11: Value of I-Divergence

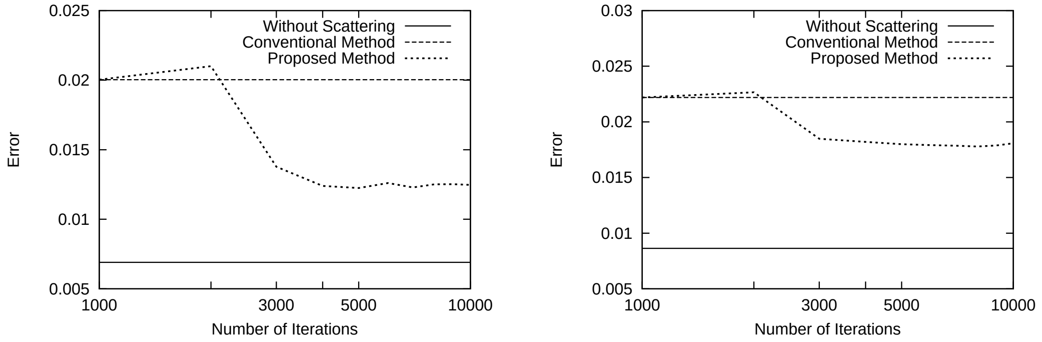

(a) Phantom a (b) Phantom b

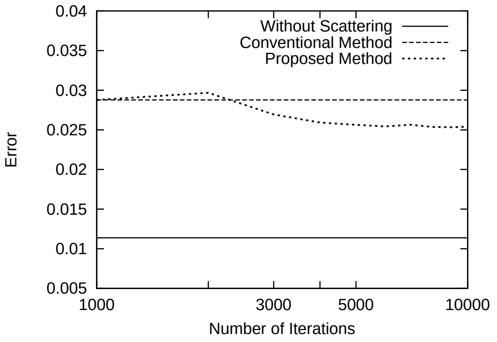

(c) Phantom c

Figure 12: Root-mean-square errors of the attenuation coefficient

3.3 Accuracy Of Scattered Radiation

If scattered radiation was not estimated with good precision, an improvement in the reconstruction image could not be observed , as mentioned previously. In this section, we observe how the scattered radiation is estimated correctly in the proposed method. Figures 13 and 14 show the estimated amount of scattered radiation after 2000 and 10000 iterations, respectively.

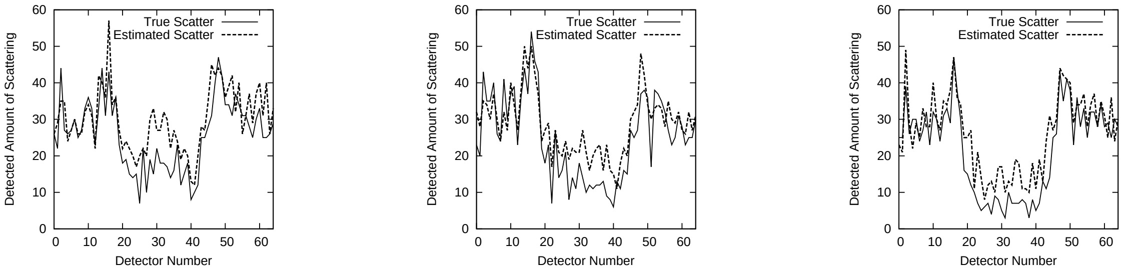

(a) Phantom a (b) Phantom b (c) Phantom c

Figure 13: 2000 iterations

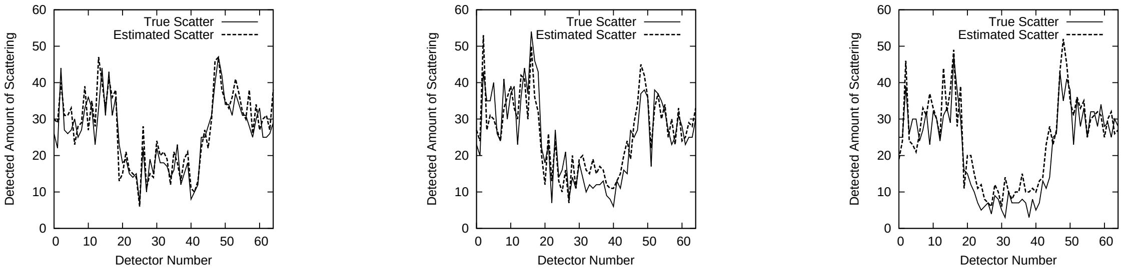

(a) Phantom a (b) Phantom b (c) Phantom c

Figure 14: 10000 iterations

The root-mean-square errors of the scattered radiation

$$Error = \frac{1}{N}\sqrt{\sum_{i=1}^{N}\frac{(\beta_i - \widehat{\beta}_i)^2}{\beta_i}} \tag{6}$$

is employed as an evaluation criterion, where N denotes the number of space divisions, β_i denotes the true scattered radiation, and $\widehat{\beta}_i$ denotes the estimated scattered radiation in each iteration. From Figures 13-15, for all of the phantoms, it is observed that as the number of iterations increases, the shapes of the estimated scattered radiation approach the true ones. Thus, we have shown the validity of the proposed method.

4 Conclusion

In this study, we proposed an image reconstruction algorithm in consideration of scattered radiation, and showed its validity. This result may make it possible to develop a reconstruction algorithm for cone-beam CT in order to obtain reconstructed images that are free from the influence of scattered radiation. As future research, it is necessary to increase the number of divisions in the objective space in order to apply the proposed method to practical clinical use.

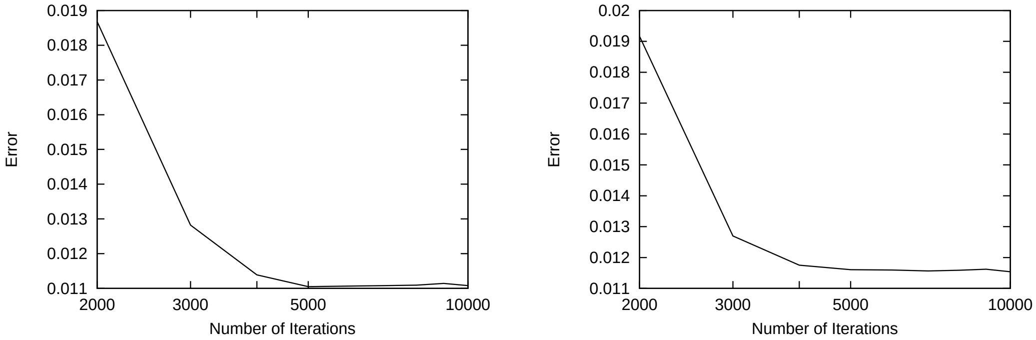

(a) Phantom a (b) Phantom b

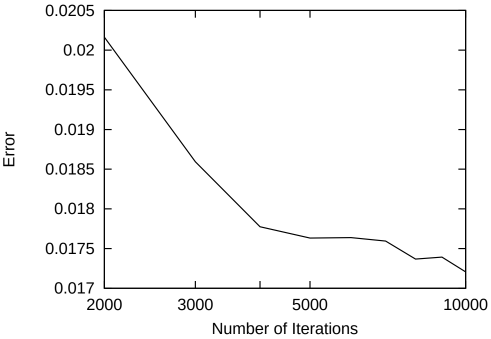

(c) Phantom c

Figure 15: Root-mean-square errors of the scattered radiation

References

[1] K. Tokumoto, Y. Yamazaki, N. Toda, "Effects of Scattering on the Reconstruction of Dual-Energy X-ray CT", KEK Proceedings, 2011-6, 2011.

[2] H. Hirayama, Y. Namito, A. F. Bielajew, S. J. Wilderman, W. R. Nelson, "The EGS5 Code System, 2005-8, SLAC-R-730", Radiation Science Center Advanced Research Laboratory, High Energy Accelerator Research Organization (KEK), Stanford Linear Accelerator Center, Stanford, CA, 2005.

[3] J. A. Fessler, I. A. Elbakri, P. Sukovic, N. H. Clinthorne, "Maximum-Likelihood Dual-Energy Tomography Image Reconstruction", Society of Photo Optical Instrumentation Engineers (SPIE) Conference Series, Vol. 4684, pp.38-49, 2002.

[4] J. A. O'Sullivan, J. Benac, "Alternating Minimization Algorithms for Transmission Tomography", IEEE Trans. Med. Imaging, Vol.26, No.3, pp.283-297, 2007.

[5] Y. Yamazaki, N. Toda, "Cone-Beam Dual-Energy CT Using an Asymmetric Filter", The Institute Of Electronics, Information and Communication Engineers D, Vol. J94-D, No.7, pp.1154-1164, 2011.

INTERNAL DOSIMETRY FOR NASAL THALLIUM-201 ADMINISTRATION

S. Kinase[1], K. Washiyama[2], H. Shiga[3], J. Taki[4], Y. Nakanishi[2],
K. Koshida[2], T. Miwa[3], S. Kinuya[4], and R. Amano[2]

[1]Nuclear Safety Research Center,
Japan Atomic Energy Agency, Ibaraki 319-1195, Japan
[2]Department of Quantum Medical Technology, Graduate School of Medical Science,
Kanazawa University, Ishikawa 920-0942, Japan
[3]Department of Otorhinolaryngology-Head and Neck Surgery,
Kanazawa Medical University, Ishikawa 920-0293, Japan
[4]Department of Biotracer Medicine, Graduate School of Medical Science,
Kanazawa University, Ishikawa 920-8640, Japan
e-mail: kinase.sakae@jaea.go.jp

Abstract

To enable us to obtain internal doses to organs/tissues around olfactory nerve from an administered ^{201}Tl in the nasal cavity, specific absorbed fractions (SAFs) for photons and electrons were evaluated for the organs/tissues using the ICRP/ICRU voxel models and Monte Carlo code. In addition, S values for the organs/tissues from ^{201}Tl in the nasal cavity were calculated by combining the appropriate decay data with the evaluated SAFs. Consequently, it was confirmed that the SAFs and S values depend on the masses of the target organs/tissues – the masses of organs/tissues around olfactory nerve, such as the brain, eyes and anterior nasal passage (ET_1). The S value for ET_1 self-irradiation in the ICRP/ICRU female reference voxel model was found to be larger than that in the ICRP/ICRU male reference voxel model.

1. Introduction

The technique of nasal administration of ^{201}Tl followed by SPECT-MRI imaging has been developed as an olfactory function test [1]. In the technique, internal dosimetry for the nasal cavity area and the olfactory bulb area is needed since the olfactory transport pathway from the nasal cavity to the olfactory bulb in the anterior skull base is irradiated by the migration of ^{201}Tl administered in the nasal cavity. In the present study, to provide data relevant to internal dosimetry on nasal ^{201}Tl administration, specific absorbed fractions (SAFs) for the brain, eyes and anterior nasal passage (ET_1) from ET_1, for photons and electrons –the fraction of energy emitted as a specified radiation type in ET_1, that is absorbed per unit mass of the brain, eyes and ET_1– were evaluated in the ICRP/ICRU voxel models [2] using the Monte Carlo simulations. In addition, S values for the brain, eyes and ET_1 from ^{201}Tl in ET_1 –mean absorbed dose to the brain, eyes and ET_1 per unit cumulated activity in ET_1– were calculated using the results of the SAFs for both photons and electrons.

2. Materials and Methods

2.1 ICRP/ICRU voxel models

The ICRP/ICRU adult male and female reference voxel models were used in the present study. The voxel models, based on computed tomographic data of real people, are digital three-dimensional representations of human anatomy. Many organs and tissues are segmented and identified. The masses of the brain, eyes and ET_1 in the voxel models are shown in Table 1.

2.2 Specific Absorbed Fractions

Specific absorbed fractions for photons and electrons were evaluated in the ICRP/ICRU voxel models using the Monte Carlo code, EGS4 [3], in conjunction with an EGS4 user code, UCSAF [4]. In the EGS4-UCSAF code, the radiation transport of electrons, positrons and photons in the phantoms was simulated, and correlations between primary and secondary particles are included. In the present study, the sources of photons and electrons were assumed to be mono-energetic in the energy range from 10 keV to 10 MeV and uniformly distributed in the source region. The source region was ET_1. Target regions were the brain, eyes and ET_1. Radiation histories were selected to be numbers sufficient to reduce statistical uncertainties below 5%. The cutoff energies were set to 1keV for the photons and 10keV for the electrons. The Parameter Reduced Electron-Step Transport Algorithm (PRESTA) [5] to improve the electron transport in the low-energy region was used. The cross-section data for photons were taken from PHOTX [6] and the data for electrons are taken from ICRU report 37 [7].

2.3 S values

S values for the brain, eyes and ET_1 from uniformly distributed ^{201}Tl within ET_1 were calculated, using the results of the SAFs for both photons and electrons. The SAFs were converted into the S values, through consideration of the masses of the target organs/tissues and the decay modes of ^{201}Tl. Table 2 summarizes decay data for ^{201}Tl [8].

3. Results and discussion

3.1 Specific Absorbed Fractions

Figures 1 (a) and (b) show SAFs for photons and electrons in the ICRP/ICRU adult male reference voxel model in the energy range of 10 keV to 10 MeV. Unlike the photon SAFs for cross-irradiation, the photon SAFs for ET_1 self-irradiation decrease with an increase in the photon energy on the whole. It would appear that the photon SAFs for ET_1 self-irradiation are largely dependent on the photon cross-section data for ET_1. The electron SAFs for ET_1 self-irradiation show constancy up to 1 MeV and then a decrease while the electron SAFs for cross-irradiation increase with increasing electron energy. The SAFs for photons and electrons show energy dependence as well as organ/tissue mass dependence, as mentioned in previous studies. SAFs for photons and electrons in the ICRP/ICRU adult female reference voxel model are shown in Figs. 2 (a) and (b). The SAFs in the ICRP/ICRU adult female reference voxel model show similar trend in the ICRP/ICRU adult male reference voxel model.

3.2 S values

S values for the brain, right eye and ET_1 from ^{201}Tl in ET_1 are shown in Fig. 3. It can be seen that the S value for ET_1 self-irradiation in the ICRP/ICRU female reference voxel model was found to be larger than that in the ICRP/ICRU male reference voxel model. This is mainly due to the different mass of ET_1.

4. Conclusions

The SAFs for the brain, eyes and ET_1 were evaluated for both photons and electrons in ET_1 of the

ICRP/ICRU voxel models using EGS4-UCSAF code. Furthermore, the S values for the brain, eyes and ET_1 from ^{201}Tl in ET_1 were calculated using the results of the SAFs. It was confirmed that both the SAFs and S values depend on the masses of the target organs/tissues. We plan in the near future to evaluate dosimetric data, such as effective doses to the nasal ^{201}Tl administration.

References

1) H. Shiga, J. Taki, M. Yamada, K. Washiyama, R. Amano, Y. Matsuura, O. Matsui, S. Tatsutomi, S. Yagi, A. Tsuchida, T. Yoshizaki, M. Furukawa, S. Kinuya, and T. Miwa, “Evaluation of the olfactory nerve transport function by SPECT-MRI fusion image with nasal thallium-201 administration”, Mol. Imaging Biol., **13**, 1262-1266 (2011).
2) ICRP, “Adult reference computational phantoms”, ICRP Publication 110 (Oxford: Elsevier)(2009).
3) W. R. Nelson, H. Hirayama, and D. W. O. Rogers, “The EGS4 Code System”, SLAC-265 (Stanford Linear Accelerator Center, Stanford, CA, 1985).
4) S. Kinase, M. Zankl, J. Kuwabara, K. Sato, H. Noguchi, J. Funabiki, and K. Saito, “Evaluation of specific absorbed fractions in voxel phantoms using Monte Carlo simulation”, Radiat. Prot. Dosim., **105**, 557-563(2003).
5) A. F. Bielajew and I. Kawrakow, “The EGS4/PRESTA-II electron transport algorithm: Tests of electron step-size stability”, In Proceedings of the XII’th Conference on the Use of Computers in Radiotherapy, 153-154 (Madison, WI:Medical Physics Publishing) (1997).
6) RSIC, DLC-136/PHOTX Photon interaction cross section library (contributed by National Institute of Standards and Technology) (1989).
7) ICRU, “Stopping powers for electrons and positrons”, ICRU Report 37 (Bethesda, MD, USA: ICRU) (1984).
8) A. Endo, Y. Yamaguchi and K. Eckerman, “Nuclear decay data for dosimetry calculation revised data of ICRP Publ.38”, JAERI 1347 (2005).

Table 1. Masses of the brain, eyes and anterior nasal passage (ET_1) in the ICRP/ICRU voxel models

Organ/tissue	Mass (kg)	
	Male	Female
Brain	1.4×10^0	1.3×10^0
Eye lens, left	1.9×10^{-4}	2.1×10^{-4}
Eye lens, right	1.9×10^{-4}	1.9×10^{-4}
ET_1	1.1×10^{-2}	4.3×10^{-3}

Table 2. Summary decay data for ^{201}Tl[*]

Radiation	Number	Frequency (/nuclear transformation)	Energy (MeV/nuclear transformation)	Mean Energy (MeV)
Gamma rays	9	1.3×10^{-1}	2.1×10^{-2}	1.6×10^{-1}
X rays	21	1.4×10^0	7.3×10^{-2}	5.3×10^{-2}
IC electrons	42	9.0×10^{-1}	3.0×10^{-2}	3.3×10^{-2}
Auger electrons	21	3.4×10^0	1.4×10^{-2}	4.1×10^{-3}

[*] In the present study, some radiations were neglected since they would be insignificant for the S value calculations.

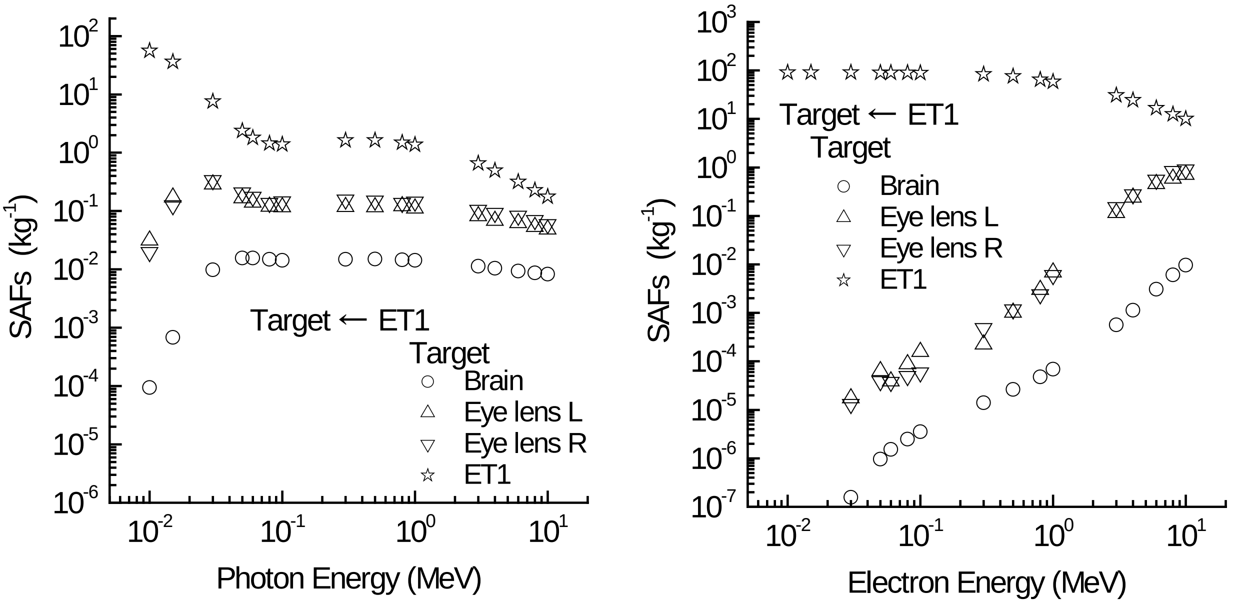

(a) (b)

Figure 1. Specific absorbed fractions for photons (a) and electrons (b) for source region ET_1 and target region the brain, eyes and ET_1 in the ICRP/ICRU adult male reference voxel model.

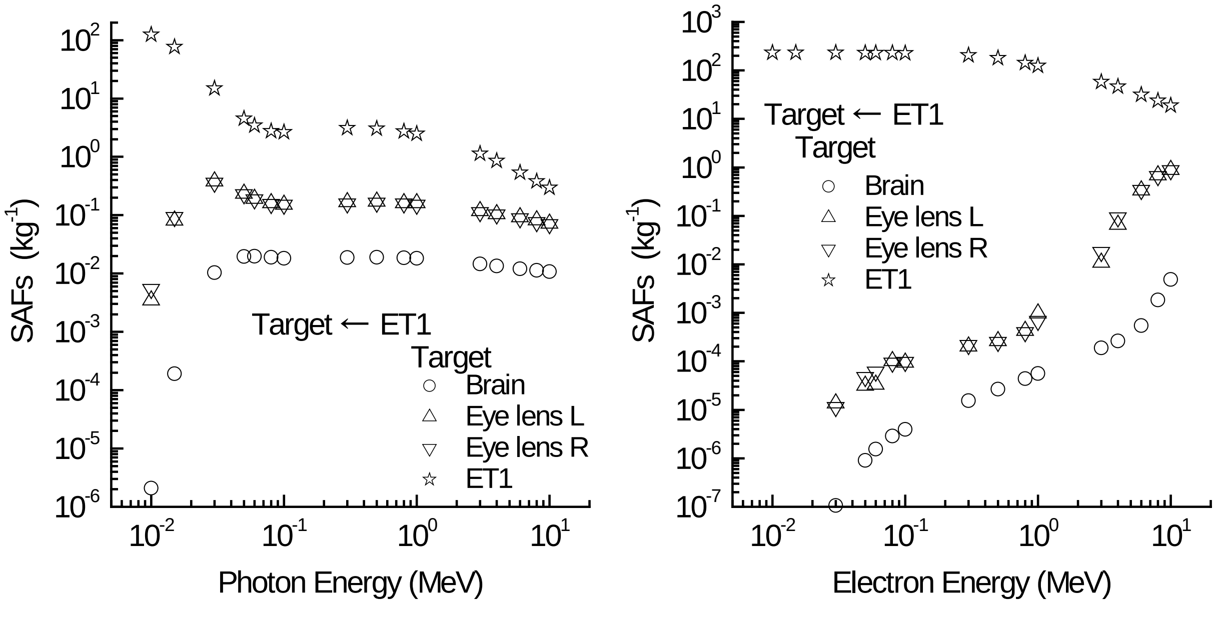

(a) (b)

Figure 2. Specific absorbed fractions for photons (a) and electrons (b) for source region ET_1 and target region the brain, eyes and ET_1 in the ICRP/ICRU adult female reference voxel model.

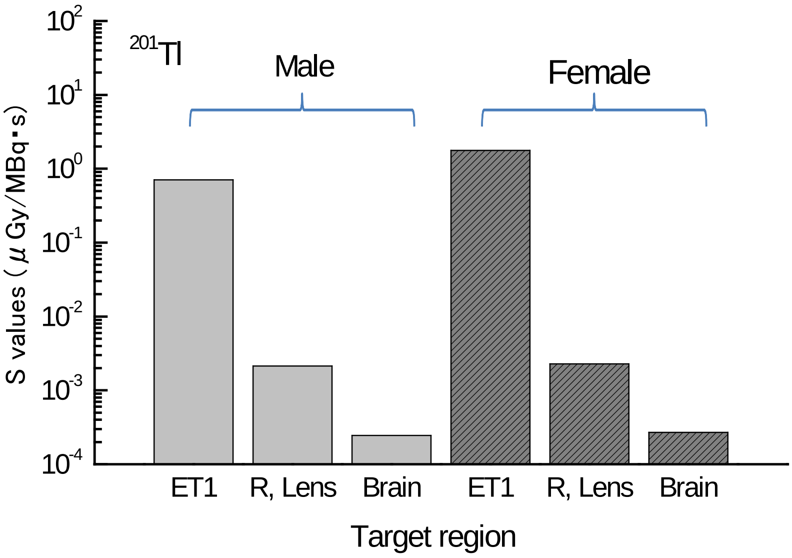

Figure 3. S values for the brain, right eye and ET_1 from ^{201}Tl in ET_1 of the ICRP/ICRU voxel models.

Verification of the effect of dose reduction system in computed tomography
— Evaluation of organ and tissue dose distribution using EGS5 simulation —

D.Hayashi and S.Koyama

Department of Radiological Technology, Graduate School of Medicine, Nagoya University
1-1-20 Daikou-Minami, Higashi-ku, Nagoya, 461-0043, Japan
E-mail: hayashi.daiki@g.mbox.nagoya-u.ac.jp

Abstract

Computed tomography auto exposure control (CT-AEC) is designed to reduce exposed radiation dose and to equalize overall image quality in X-ray CT. This study aims to validate the dose reduction effect of CT-AEC with dose distribution maps created in an anthropomorphic phantom using the Electron Gamma Shower ver. 5 (EGS5) Monte Carlo simulation code. Further we actually measured the absorbed doses of each organ and tissue in the phantom with and without CT-AEC. The organ doses in the simulation result were in good agreement with the measurement results. The dose reduction effect was assessed by a comparison of dose distribution maps with and without CT-AEC. In conclusion, the results of this study revealed that the combination of dosimetry in anthropomorphic phantoms and calculation by simulation enables a detail assessment of the dose reduction effect of CT-AEC.

1. Introduction

Over the last several years, computed tomography (CT) scanner manufactures have implemented several scan technologies and applications to enhance CT image quality and reduce exposed radiation dose. One such technology is the CT auto exposure control (CT-AEC). CT-AEC is designed to reduce exposed dose and to equalize overall image quality of the axial slices in X-ray CT. Nearly all commercially available CT scanners are equipped with CT-AEC, which can be used to performs X-ray tube current modulation (TCM) according to the physical constitution of each patient. The dose reduction effect of CT-AEC has been reported in the literature [1-3].

The human dose from a CT scan can be estimated through two methods: the measurement of organ and tissue doses in an anthropomorphic phantom [4] and the calculation of energy deposition in a voxelized human phantom using a Monte Carlo simulation [5]. This study aims to assess the dose reduction effect of CT-AEC with dose distribution maps created in an anthropomorphic phantom using the Electron Gamma Shower ver. 5 (EGS5) Monte Carlo simulation code.

2. Materials and Methods

2.1 CT scan

An anthropomorphic phantom (THRA1, Kyoto Kagaku, Kyoto, Japan) implanted with 48 semiconductor dosimeters was scanned using a multislice CT scanner (Aquilion64, Toshiba Medical Systems, Tochigi, Japan). The body trunk of the phantom was scanned. The detailed scan parameters were a tube voltage of 120kV, a beam width of 1×32 mm, a rotation time of 0.5 s, a scan time of 14.2 s, and a pitch of 2.7008. The total scan length was 70.5 cm (excluding additional rotations owing to longitudinal over-ranging).

For the scanning operation with CT-AEC, users must set a standard deviation (SD) for image noise and maximum tube current. The setting conditions were an SD of 8 and a maximum tube current of 450 mA. Additionally, the phantom was scanned without CT-AEC with the aim of assessing the effect of CT-AEC. The tube current setting without CT-AEC was 450 mA.

2.2 CT simulation geometry

Figure 1 shows the simulation geometry. The voxelized phantom was created from CT images of the THRA1 anthropomorphic phantom and consisted of soft tissue, lung, and bone. In order to match the geometry of the Aquilion64 X-ray CT unit, a bow-tie filter and a CT bed must be considered in the simulation. The angle of the X-ray CT fan beam was 38°, the beam width was 3.2 cm, and the source-isocenter distance was 60cm. The X-ray tube was rotated 360° around the voxelized phantom with in increments of 1° under the same scan conditions including an over-ranging of 2 rotations at the scan beginning and scan end. The simulation was performed with and without CT-AEC.

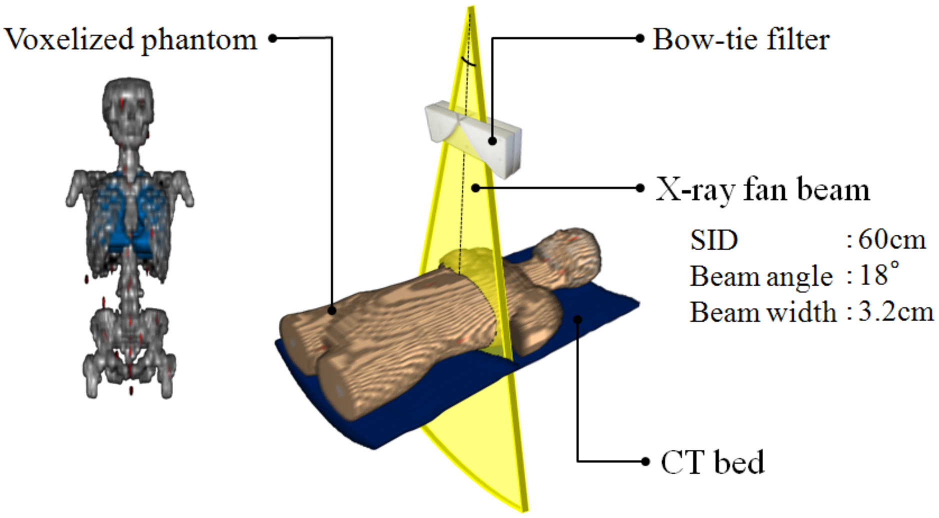

Figure 1. CT simulation geometry

2.3 Modeling CT-AEC

The actual values of the tube current under CT-AEC were obtained from the image displayed on the CT console as shown in **Figure 2(a)**. Angular and longitudinal TCM was performed using a sinusoidal wave between the lateral tube current and the anterior-posterior (A-P) tube current. **Figure 2(b)** shows a plot of the TCM, created from the value obtained from the image (**Figure 2(a)**). This plot shows the relative tube current value along the longitudinal axis. In the simulation, the number of incident photons was varied for each 1° increment according to the data.

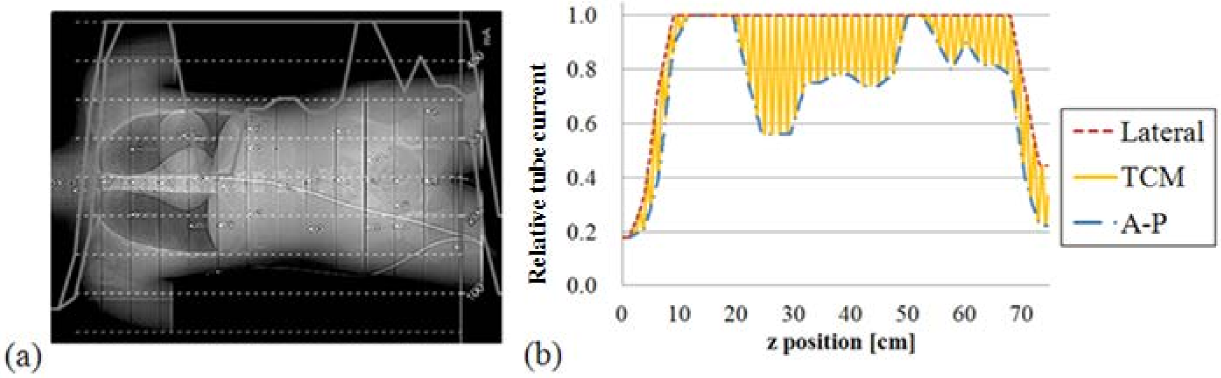

Figure 2. Angular and longitudinal TCM under CT-AEC: **(a)** TCM (actual values of tube current) image printed on CT console. **(b)** Relative tube current value as z axis made from **(a)**.

2.4 Creating absorbed dose distribution maps of organ and tissue

As the THRA1 phantom had no organs, 17 organ areas were assigned to the phantom. **Figure 3** illustrates the process of assigning organs to the soft tissue area. The weight of each organ was kept within 5 % of the literature values, which reflected the organ weight of the average Japanese male [6]. **Figure 4** shows a three-dimensional view of 17 organ areas added to the voxelized phantom. The dose distribution map of each organ and tissue was created from the absorbed doses calculated by the above method. The dose reduction effect of CT-AEC was assessed by comparing the dose distribution maps with and without CT-AEC.

Figure 3. Illustration of the process of assigning organs into soft tissue area: Left image shows an axial CT image of THRA1 phantom. Middle image shows an axial image of voxelized phantom converted from CT image. Right image shows axial image after assigning organ areas into soft tissue area.

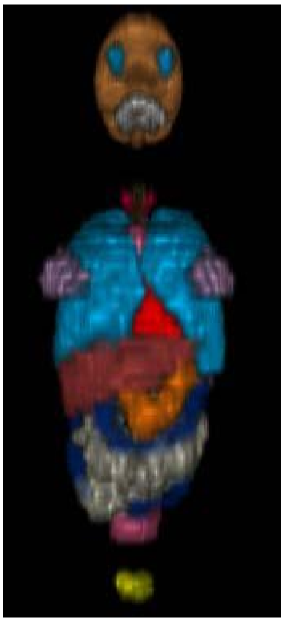

Figure 4. The three-dimensional view of 17 organs in the voxelized phantom

3. Results

3.1 Confirmation of simulation with measurement

Figures 5 and **6** show the comparison between the measurement and simulation values of the absorbed and effective doses. **Figure 5** represents the case with CT-AEC and **Figure 6**, the case without CT-AEC. **Figure 7** shows the comparison between the measurement and simulation values of the absorbed dose reduction rates. The results of the simulation are mostly in agreement with the results of measurements in these 3 figures. The average absolute percentage differences were about 3.5 % with CT-AEC, about 4.0 % without CT-AEC, and about 3.4 % of the absorbed dose reduction rates.

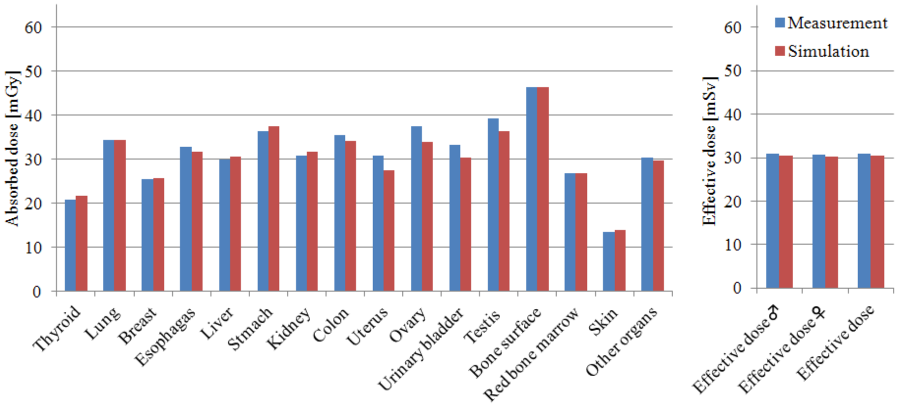

Figure 5. Comparison between measurement and simulation of absorbed doses and effective dose with CT-AEC

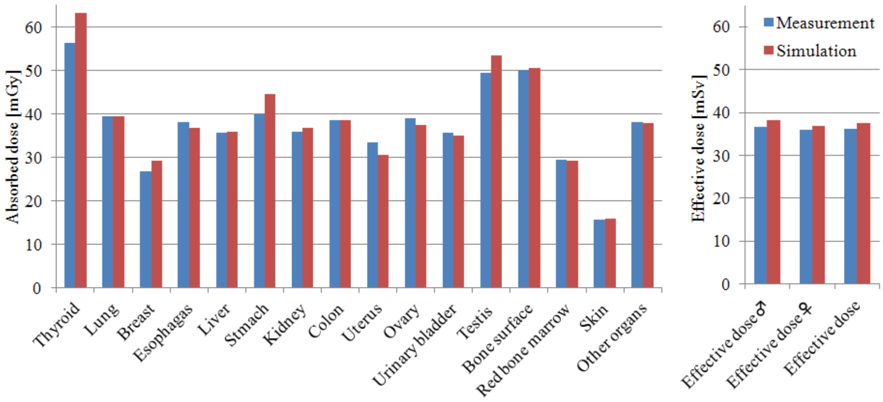

Figure 6. Comparison between measurement and simulation of absorbed doses and effective dose without CT-AEC

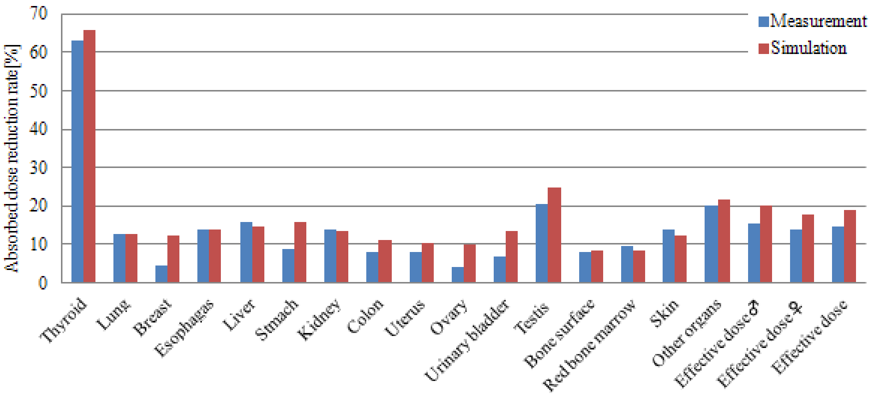

Figure 7. Comparison between measurement and simulation of absorbed dose reduction rates

3.2 Absorbed dose distribution of organ and tissue

Figures 8–12 show the dose distribution maps of each organ and tissue region created from the absorbed dose of each voxel. **Figure 8** shows the skin map; **Figure 9**, the bone surface map; **Figure 10**, a map of the chest and neck organs (thyroid, lung, heart, and thymus); **Figure 11**, a map of the upper abdominal organs (liver, stomach, kidney, adrenal, spleen, pancreas, and gallbladder); and **Figure 12**, a map of the lower abdominal organs (small intestine and colon).

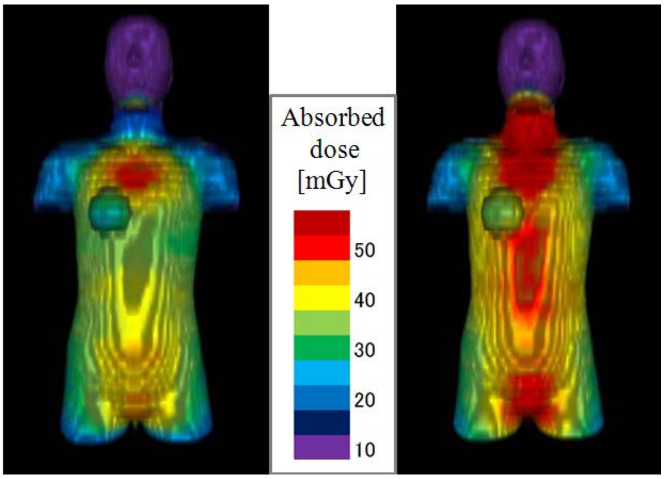

Figure 8. Absorbed dose distribution map of skin with CT-AEC (left) and without CT-AEC (right)

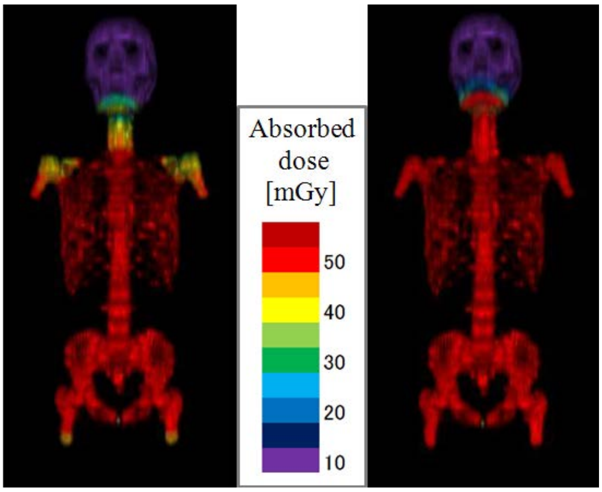

Figure 9. Absorbed dose distribution map of bone surface with CT-AEC (left) and without CT-AEC (right)

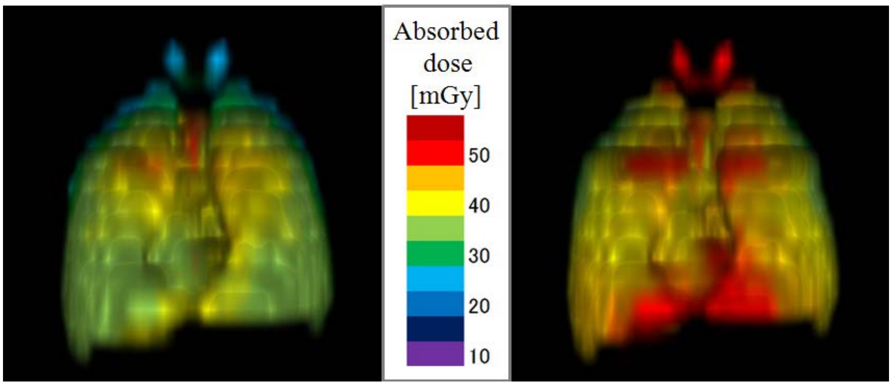

Figure 10. Absorbed dose distribution map of chest and neck organs (Thyroid, lung, heart and thymus) with CT-AEC (left) and without CT-AEC (right)

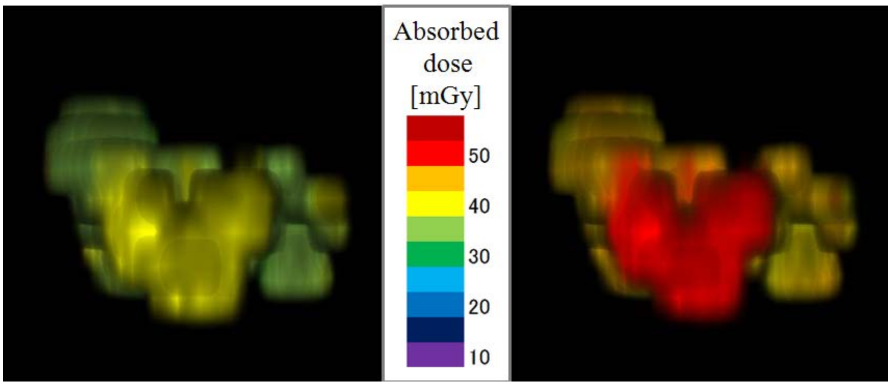

Figure 11. Absorbed dose distribution map of upper abdominal organs (Liver, stomach, kidney, adrenal, spleen, pancreas and gallbladder) with CT-AEC (left) and without CT-AEC (right)

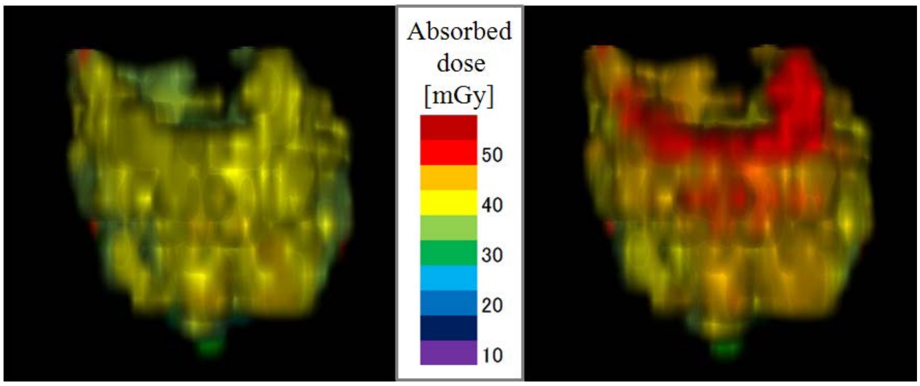

Figure 12. Absorbed dose distribution map of lower abdominal organs (Small intestine and colon) with CT-AEC (left) and without CT-AEC (right)

4. Discussion

In the simulation of CT scans, the bow-tie filter and CT bed were taken into account to match the geometric conditions of the CT scanner. The average absolute percentage differences between the measurement and simulation values of the absorbed and effective doses were about 3.5 % with CT-AEC and about 4.0% without CT-AEC, as shown in **Figures 5** and **6**, respectively. These results proved the reliability of the CT scan simulation. For CT-AEC simulation, the average absolute percentage difference between the measurement and simulation values of the absorbed dose reduction rates were about 3.3 %, as shown in **Figure 7**. This result also proves the reliability of the CT-AEC simulation.

The dose reduction effect of CT-AEC was assessed in detail by the dose distribution maps shown in **Figures 9–13**. With respect to the skin dose, CT-AEC significantly reduces the dose to the neck area and the front of the body trunk, as illustrated in **Figure 9**. For the bone surface (**Figure 10**), CT-AEC reduces the dose to the mandible, cervical spine, and shoulder bones. The organ dose maps shown in **Figures 11–13** indicate that CT-AEC significantly and equally reduced the dose to the thyroid and other organs. For example, the skin dose map with CT-AEC (left side of **Figure 9**) shows that the absorbed dose on the front chest area is about 50 mGy, and that on the shoulder area is about 25 mGy. In the measurements using the anthropomorphic phantom, it is possible that only the maximum absorbed dose was measured in each organ. In local dosimetry using a limited number of small dosimeters, it was necessary to allocate the dosimeters to appropriate positions within the phantom to avoid underestimation. It remains a challenge for future research to propose a procedure for measuring the maximum absorbed dose in each organ and tissue region.

5. Conclusions

The results of this study revealed that the combination of measurement in an anthropomorphic phantom and simulation calculation enables the assessment of the dose reduction effect of CT-AEC; the results also indicate that CT-AEC reduces the exposure dose to specific organ and tissue.

References

1) Coursey C, Frush DP, Yoshizumi T et al. *Pediatric chest MDCT using tube current modulation: effect on radiation dose with breast shielding.* AJR 190:W54–W61 (2008).
2) He W, Huda W, Magill D, Tavrides E, Yao H. *X-ray tube current modulation and patient doses in chest CT.* Radiat. Prot. Dosimetry **143**, 81–87 (2011).
3) van Straten M , Deak P , Shrimpton PC , Kalender WA. *The effect of angular and longitudinal tube current modulations on the estimation of organ and effective doses in x-ray computed tomography.* Med. Phys. **36,** 4881 – 4889 (2009).
4) HUDA, W. & SANDISON, G. A. *The use of the effective dose equivalent, HE, as a risk parameter in computed tomography.* British Journal of Radiology, **59**, 1236-1238 (1986).
5) Jarry G, DeMarco JJ, Beifuss U, Cagnon CH, McNitt-Gray MF. *A Monte Carlo-based method to estimate radiation dose from spiral CT: From phantom testing to patient-specific models.* Phys. Med. Biol. **48**, 2645−2663 (2003).
6) G.Tanaka and H.Kawamura. *Anatomical and physiological characteristics for Asian reference man. Male and female of different ages.* NIRS-M-115, (1996).

Reduction of Radiation Dose to Children in X-Ray Head CT
: Investigation Using EGS5

T.Ishii[1], S.Kondo[1], T.Haba[1], D.Hayashi[1], H.Numamoto[1], S.Koyama[1]

[1]Department of Radiological Technology, Graduate School of Medicine, Nagoya University
1-1-20 Daiko-Minami, Higashi-ku, Nagoya 461-8673, Japan
e-mail: ishii.takanori@a.mbox.nagoya-u.ac.jp

Abstract

In this study, the absorbed dose for organs in infant, child, and adult patients undergoing head computed tomography (CT) scans was determined. The CT examinations were simulated using the Electron Gamma Shower ver. 5 (EGS5) Monte Carlo code. The eye lens dose among child and infant patients was higher than that among adult patients by 15.0% and 69.7%, respectively. The effectiveness of a bismuth shield in reducing the eye lens dose for children undergoing head X-ray head CT scans was also evaluated. Application of a bismuth shield over the eyes of children undergoing head X-ray CT reduced the eye lens dose by 47.6% from the dose value in the case wherein shielding was not used. The use of metallic shields was found effective in reducing the radiation dose to children.

1. Introduction

X-ray computed tomography (CT) examination is a valuable diagnostic technique, and the immediate benefit to an individual patient can be substantial. Evaluations of radiation dose to patients have been regarded as absolutely imperative, because the relatively high radiation doses in X-ray CT compared with other plain radiography methods have raised health concerns [1]. There is a potential increase in future cancer risk from radiation exposure, particularly among infants and children, as they are more sensitive to radiation than adults. Substantial effort is required to reduce the radiation dose to infants and children. There are several dose reduction techniques including auto exposure control (AEC), low-tube current setting, adaptive noise reduction filters, and shielding with bismuth radio-protective garments [2].

The aim of this study was to evaluate the absorbed dose for organs of infant, child and adult patients undergoing head CT scans, and compare the absorbed dose among them. The effectiveness of a metallic shield that was used for reduction of the eye lens dose in head CT scans was also evaluated.

2. Materials and Methods

All simulations were performed using the electron gamma shower ver.5 (EGS5) Monte Carlo code. A helical X-ray CT unit Aquilion64 (Toshiba Medical Systems, Tochigi, JAPAN) was used for this simulations.

2.1 Anthropomorphic voxel phantoms

Three voxel phantoms were developed based on the CT images of infant, child, and adult anthropomorphic phantoms composed of lung, bone, and soft tissue. Figure 1 shows a photograph of the phantoms. These phantoms were scanned by X-ray CT. Obtained images were converted to voxel images. Brain, eye lens and thyroid labels, for serially numbered subjects, were assigned correctly to the value of each voxel in reference to the weights of the organs in normal Japanese subjects [3]. Examples of the original CT image and converted voxel image are shown in Figure 2. The absorbed energy doses for entire target organs were evaluated. Voxel sizes were $3.06 \times 3.06 \times 10.0$ mm^3 for the infant voxel phantom, $1.0 \times 1.0 \times 10.0$ mm^3 for that of the child, and $1.56 \times 1.56 \times 6.66$ mm^3 for that of the adult. Table 1 lists the characteristics of the infant, child, and adult voxel phantoms.

2.2 Simulation geometry

The X-ray fan beam angle was 38°, and the beam width at the center of rotation was 32 mm. The source-isocenter distance was 600 mm. The focus of the X-ray tube was rotated 360° in 1° step around the phantom. The head CT scan protocol was applied, the X-ray tube voltage was 120 kV and the pitch factor was 0.8. Scan lengths were 8.5 cm for the infant, 11 cm for the child, and 14 cm for the adult.

X-ray CT equipment generally uses a beam-shaping filter in front of the X-ray tube radiation window. After passing through a patient, X-rays are adjusted by the beam-shaping filter to produce homogeneous X-ray energy at the CT detector. The design of the beam-shaping filter is proprietary manufacture’s data. The aluminum half value layer (AL HVL) and dose profiles were measured for beam-shaping filter [4]. Based on this data, changes in the energy spectra and photon numbers were incorporated into the simulation. To incorporate the effect of the beam-shaping filter, the X-ray fan beam angle was divided into 7 segments (0–1.5°, 1.5–4.5°, 4.5–7.5°, 7.5–10.5°, 10.5–13.5°, 13.5–16.5°, and 16.5–18°) on one side of the fan beam. We applied 7 different energy spectra (54, 57, 59, 62, 64, 72, and 73 keV), respectively, to the beam segments. The number of incident photons corresponding to the dose distribution data was applied for each segment (0°–18°) of the X-ray fan beam.

The bed which holds a patient for X-ray CT is typically made of carbon fiber. Its composition and material density are proprietary manufacture’s data. The actual dose ratio between the conditions with a bed to those without a bed was measured. Assuming that the material of the bed was carbon, the density of the bed was adjusted to correspond with the measured dose ratio. The effect of attenuation produced by the table was incorporated into the simulation.

2.3 Evaluation of the effectiveness of metallic shields

To investigate the dose reduction effect produced by a metal shield, a bismuth shield was placed over the eyelids of children undergoing head CT scans. The size of the bismuth sheet was $20.0 \times 150.0 \times 2.0$ mm^3, and the density was 0.98 g/cm^3. CT head scanning was performed with a bismuth shield placed 10.0 mm above the eyelids [5]. A thin aluminum filter was inserted at different locations to evaluate their effect on the reduction of scattering radiation. In one case, aluminum filter was inserted between the shield and the phantom (position L). In another case, the aluminum sheet was inserted between the shield and the X-ray source (position U). The size of aluminum filters was the same with the bismuth sheet.

A copper shield, which has lower atomic numbers and lower yield of characteristic X-rays as compared to bismuth, was also used. The size and alignment of the copper shield was the same as the in case of the bismuth shield. The reduction in the absorbed dose was compared between the bismuth shielding and copper shielding cases.

3. Results

Figure 3 shows the absorbed dose in the brain, eye lens, and thyroid for each anthropomorphic phantom undergoing a head CT scan. Any organ doses were normalized to the brain dose for an adult. In Figure 3, the absorbed dose in the eye lens can be seen to decrease with advancing age. The eye lens dose of a child and an infant was higher than that of an adult by 15.0% and 69.7% respectively.

Table 2 compares the reduction of radiation dose to the eye lens of a child achieved by using three metallic shields. A bismuth shield reduced the eye lens dose by 47.6% from the dose without the shield. The aluminum sheet inserted at lower side (position L) reduced the eye lens dose by 1.3% from the dose value in the case of the aluminum sheet inserted at upper side (position U). By comparing the result obtained for the copper shield with those obtained for the bismuth shield, the eye lens dose was reduced by 36.7% from the dose value in the case wherein the bismuth shield was not used.

4. Discussion

It is found from Fig.3 that the eye lens doses for the infant and child were higher than for the adult, by 15.0%~69.7%. The dose reduction depended on the size of the phantom. It is important that appropriate scanning protocols are selected for infants and children to reduce radiation doses. The brain dose for the infant was higher than for the child due to differences in the construction of their internal organs. Photons with lower energy were absorbed more often, and organ doses from these photons are more influenced by body contours and the organ depth in the patient. The effective doses were only slightly different from the organ doses.

The data in Table 2 indicate that bismuth shields and copper shields placed over the eyelids of children undergoing head X-ray CT are both effective for reducing eye lens exposure, however, the bismuth shield is more effective than the copper shield. Bismuth has a higher atomic number, and consequently, it show a higher absorbency of the radiation dose. The use of metallic shields was found effective in reducing the radiation dose. However, these metallic shields must be applied carefully since they may degrade the quality of a diagnostic image. They use of an additional aluminum filter afforded significant enhancement of the dose reduction through the blocking of scattering radiation. It can be seen that the bismuth shield with an aluminum filter was more effective in reducing the radiation dose than only the bismuth shield.

5. Conclusions

The absorbed doses in the organs of infant, child and adult patients undergoing head CT scans were evaluated and compared based on voxel phantoms using a Monte Carlo simulation. Consequently, major differences were found between the organ doses of the infant, child, and adult anthropomorphic phantoms. Metallic shields were found effective for reducing the eye lens dose.

References

1) International Commission on Radiological Protection, “Managing Patient Dose in Computed tomography,” ICRP publication 87, Annals of the ICRP 30 (4) (2000)
2) International Commission on Radiological Protection, “The 2007 Recommendations of the International Commission on Radiological Protection,” ICRP publication 103, Annals of the ICRP 37 (2007)
3) G. Tanaka, Y. Nakahara, Y. Nakazima, “Japanese Reference Man 1988-IV –Studies on the Weight and Size of Internal Organs of Normal Japanese-,” JRS. **49**(3), 344-364, (1989)
4) M. Tucker, G. Barnes, D. Chakraborty, “Semiempirical model for generating tungsten target x-ray spectra,” Med. Phys.**18**, 211-218 (1991)
5) M. Raissaki, K Perisinakis, John Damilakis, N. Gourtsoyiannis, “Eye-lens bismuth shielding in paediatric head CT : artifact evaluation and reduction” Pediatr radiol. **40**, 1748-1754, (2010)

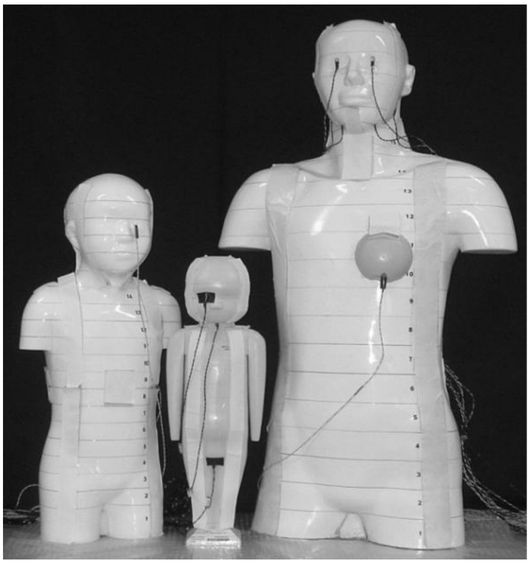

Figure 1. Anthropomorphic phantoms of child, infant and adult.

Table 1. Characteristics of the adult, child, and infant voxel phantoms.

	Adult	Child	Infant
Property			
Height(m)	1.70	1.15	0.51
Mass(kg)	60.0	20.0	3.5
Organs			
Brain(kg)	1.7×10^{0}	1.0×10^{0}	3.3×10^{-1}
Lens(kg)	1.2×10^{-3}	4.9×10^{-4}	2.0×10^{-4}
Thyroid(kg)	2.0×10^{-2}	3.9×10^{-3}	2.2×10^{-3}

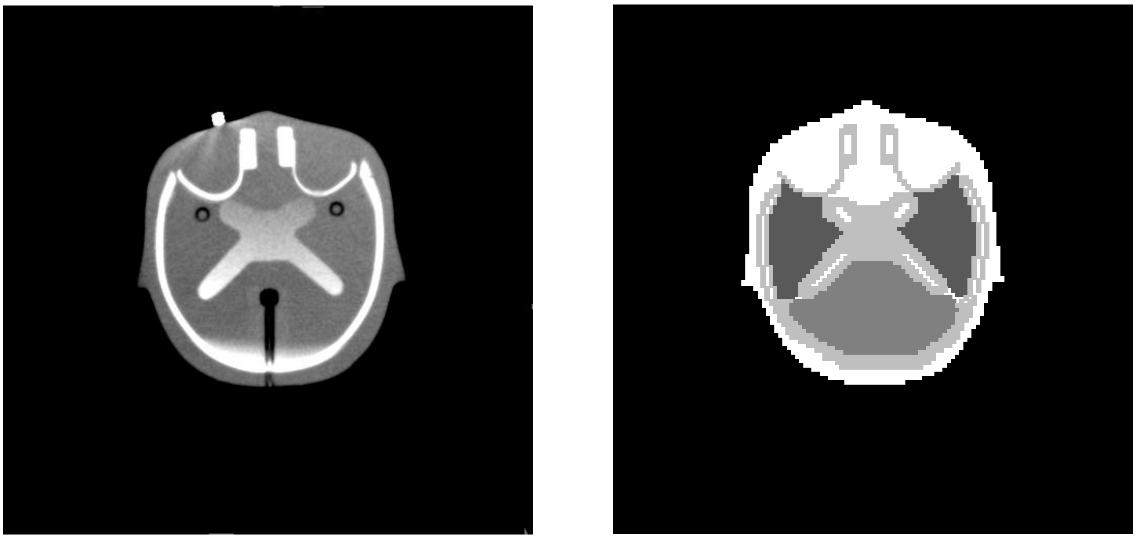

(a) (b)

Figure 2. Images of the original phantom image (a) and converted voxel image containing organs (b).

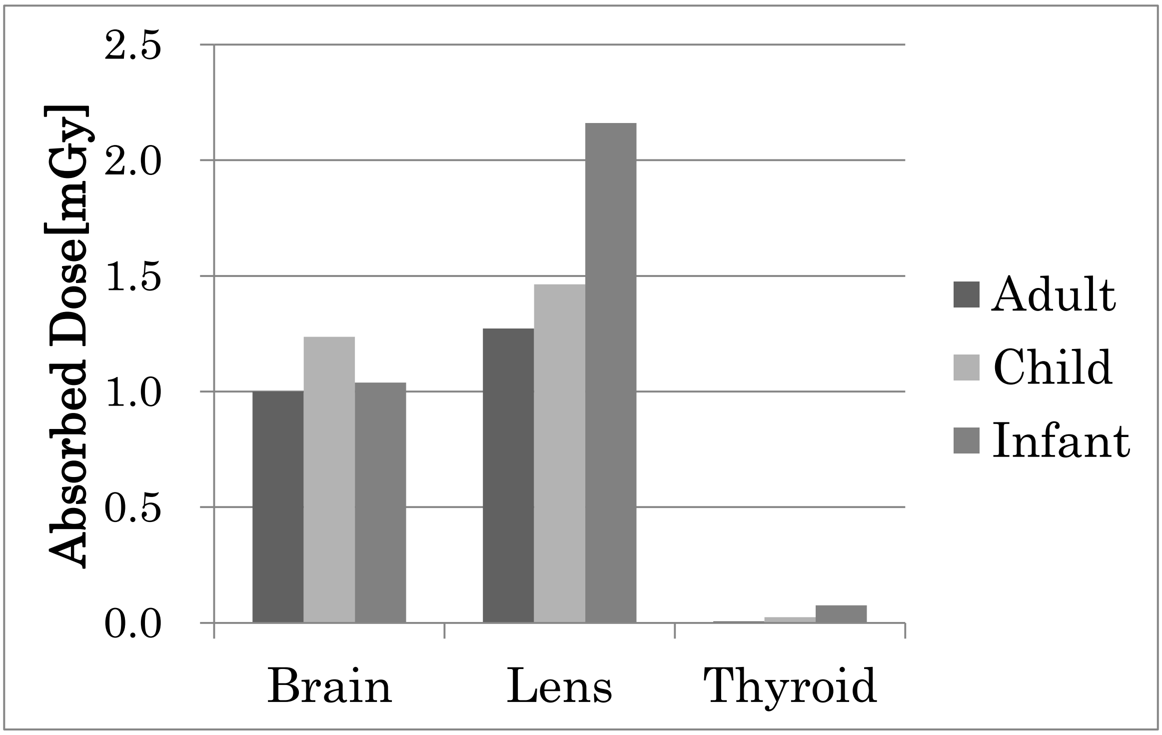

Figure 3. Comparison of the organ doses of Adult, Child, and infant undergoing X-ray head CT with identical scanning protocol.

Table 2. Comparison of reduction of radiation dose to Lens of child by use of metallic shields.

Combination of the metallic shield	The dose ratio of Lens
Without metallic shield	1.000
Bismuth only	0.524
Bismuth with Aluminum(position U)	0.486
Bismuth with Aluminum(position L)	0.473
Copper only	0.633

Estimation of glandular dose distribution in mammography using EGS5

H. Numamoto[1], T. Haba[1], S. Kondo[1], D. Hayashi[1], T. Ishii[1], S. Koyama[1]

[1]Department of Radiological Technology, Graduate School of Medicine, Nagoya University
1-1-20 Daiko-Minami, Higashi-ku, Nagoya 461-8673, Japan
e-mail: numamoto.hitomi@c.mbox.nagoya-u.ac.jp

Abstract

The aim of this research is to analyze the absorbed dose distribution by changes of thickness of subcutaneous adipose and target-filter combination in mammography using EGS5. Assume the mammography examination, x-ray tube voltage, compression plate, breast model phantom, and image receptor were included in EGS5 code. That breast model phantom had various thicknesses of subcutaneous adipose. Our results showed that absorbed dose was a tendency to increase with thinning of the subcutaneous adipose thickness. It indicated that average glandular dose (AGD) that is recently used could have been underestimated. Also relative absorbed dose of glandular tissues tended to be low when the energy of incident x-ray became large. It indicated that target/filter combinations have strong effect to incident x-ray supectrum, so that we must choose most proper target/filter combinations that reduce the radiation dose while maintaining image contrast

1. Introduction

The female breast is a radiosensitive organ, and there is a risk of carcinogenesis when mammographic examination is performed. The glandular tissues within the breast are the most sensitive to radiation, and it is important to measure the average dose to these tissues for dose estimation in mammographic examination. However, it is difficult to measure the average glandular dose directly. Therefore, conversion factors based on the incident air kerma are typically used. The conversion factors are obtained by Monte Carlo calculations using a standard breast model adopted by the IPSM (1989). The standard breast model is a 4.5-cm-thick, 16-cm-diameter semicircular columnar phantom. These dimensions were chosen to be representative of an average-sized breast undergoing firm compression. The phantom has a central region composed of a 50:50 mixture by weight of adipose and glandular tissues (50% glandularity) and an outer shield region of 0.5-cm-thick adipose tissue. [1] The average glandular dose (AGD) D to the standard breast is given as

$$D = K \times g \times c \times s$$

where K is the incident air kerma at the upper surface of the breast phantom measured without backscatter, g is the incident-air-kerma-to-AGD conversion factor, c is a factor that corrects for any difference in breast composition from 50% glandularity, and s is a factor that corrects for any difference from the original tabulation by Dance (1990) due to the use of a difference X-ray spectrum. [1, 2] The standard breast model, however, does not match the thickness of subcutaneous adipose tissue in the Japanese female. Thus, the conversion factors are inappropriate for the Japanese female breast.

In this study, we estimated the difference in the absorbed dose due to differences in the thickness of subcutaneous adipose tissue and the target/filter combination in mammography examination using EGS5. In addition, the distribution of the absorbed dose was confirmed visually.

2. Materials and Methods

2.1 Monte Carlo Simulation Geometry

The calculation of the conversion factors was based on a Monte Carlo simulation developed previously for estimation of the absorbed dose and scatter in mammography. [3, 4] In the EGS5 simulation, a PCM mammography unit (Konica Minolta Health Care Co., Ltd. Japan) was used. **Fig.1** shows the imaging geometry. The X-ray-focus image distance was 63.0 cm, and the X-ray field was 14 × 23 cm^2. The breast model was compressed using a 0.25-cm-thick PMMA (polymethyl methacrylate) compression plate and placed directly on the image receptor, which was 1.0 cm thick and consisted of carbon. This geometry was created with HOWFAR in the EGS user code. Each photon simulated by EGS5 started at the focal spot of the X-ray tube, and its path was traced from region to region of the model until all its energies were absorbed or it left the system. All energies deposited in the region of the breast model and the image receptor were recorded. Backscatter from material beyond the receptor and side scatter from regions of the patient away from the breast were neglected.

Mammographic X-ray spectra were used for the spectral data [5] and the following target/filter combinations were used for the calculations: molybdenum/30 µm molybdenum (Mo/Mo), molybdenum/25 µm rhodium (Mo/Rh), and tungsten/50 µm rhodium (W/Rh). In each case, the X-ray tube voltage was 28 kV. The number of photons was 1.0 billion, and the fractional standard deviation in the center of the breast model was less than 6.0% to reduce the statistical error.

All mammography units have automatic exposure control (AEC), a mechanism that considers the subject thickness and breast density, and can control the dose automatically in order to obtain a constant image density. It is possible to obtain the proper concentration and contrast at all times. The AEC detector is located on the back of the image receptor in mammography. To consider the effect of AEC, each depth dose was normalized by the dose at the image receptor depth in EGS5.

2.2 Breast model phantom

The breast model phantom is shown in **Fig.2**. The phantom was a semicircular column 16 cm in diameter and 2.0 or 4.5 cm thick, which consisted of 0.1 × 0.1 × 0.1 cm^3 voxels. Its central region comprised an equal mixture by weight of adipose and glandular tissue, so a random number was generated to provide a 50:50 proportion of adipose tissue:glandular tissue, and the glandular tissue and adipose tissue were assigned per voxel accordingly. [6] The 2.0-cm-thick model had an outer shield region of adipose tissue 0.1, 0.3, or 0.5 cm thick. The 4.5-cm-thick model had an outer shield region of adipose tissue 0.1 or 0.5 cm thick.

3. Results

3.1 A change of absorbed dose due to differences in thickness of subcutaneous adipose

Figs.3 and **4** show the glandular depth doses calculated for the 4.5-cm-thick and 2.0-cm-thick phantoms, respectively. Mo/Mo combinations were used in both cases. In both figures, the solid, broken, and dotted lines indicate the relative absorbed dose in the case of 0.1-cm-thick, 0.3-cm-thick, and 0.5-cm-thick subcutaneous adipose, respectively. The depth indicates the distance from the upper surface to the lower surface of the breast model phantom.

In **Fig.3**, the absorbed dose for 0.1-cm-thick subcutaneous adipose was greater than that for the 0.5-cm thicknesses. In **Fig.4**, the absorbed dose was the highest when the subcutaneous adipose thickness was 0.1 cm. In both **Fig.3** and **Fig.4,** the absorbed dose tended to increase with thinning of the subcutaneous adipose. When calculations with different combinations of target/filter were performed, both Mo/Rh and W/Rh showed the same tendency as the result using Mo/Mo.

3.2 A change of absorbed dose due to differences in target-filter combination in mammography

In **Fig.5**, the target was Mo; the solid and dotted lines indicate the relative absorbed doses of the Mo and Rh filters, respectively. The absorbed dose with the Mo filter was greater than that with the Rh filter.

In **Fig.6**, the filter was Rh; the dotted and solid lines indicate the relative absorbed doses of the Mo and W targets, respectively. The absorbed dose with the Mo target was greater than that with the W target.

4. Discussion

In both **Fig.3** and **Fig.4,** the absorbed dose tended to increase with thinning of the subcutaneous adipose. This is probably because of a difference in the mass energy absorption coefficient. Glandular tissue absorbs more energy because its mass energy absorption coefficient is greater than that of the adipose tissue that makes up subcutaneous adipose. Thus, the volume of glandular tissue increased when the subcutaneous adipose thickness decreased, and the absorbed dose increased with this reduction in thickness. Our results showed that the conversion factors that are currently being used to estimate the AGD are inappropriate for the Japanese female breast; this result is very important for AGD estimation. Our research suggests that the AGD is underestimated because, according to the mammography guideline, the AGD is calculated using conversion factors that were derived using a breast model having a subcutaneous adipose thickness of 0.5 cm.

In **Fig.5,** the absorbed dose with the Mo filter was greater than that with the Rh filter because of a difference in the k-edge. The Rh filter has a grater k-edge, X-ray spectrum contain higher energy component than that transmitted through the Mo filter. When the incident X-ray energy is relatively large, more energy components go through the object. Then, energy deposition in the glandular tissue is reduced. Therefore glandular dose in the Mo filter is larger than that in the Rh filter. In **Fig.6,** the absorbed dose in the Mo target was greater than that in the W target because of an increase in the high-energy component. The incident spectrum generated from the W target has no characteristic X-ray in mammographic X-ray energy range, maximum energy is determined by the X-ray tube voltage. On the other hand, the incident spectrum generated from the Mo target has characteristic X-rays at 17.4 and 19.6 keV and not has X-ray component farther energy. Therefore the average energy in the W target is larger than that in the Mo target. Because the target/filter combination strongly affects the incident X-ray spectrum, it is important that we choose the most suitable target/filter combinations to reduce the radiation dose while maintaining image contrast.

Fig.7 shows the absorbed dose distribution. It demonstrates how the absorbed dose decreases from the breast surface to the deep portion. We think that this graphic makes it easy to understand the dose distribution in mammography.

5. Conclusions

It has been suggested that the absorbed dose in glandular tissues in the currently used breast model is underestimated for the Japanese female. In the future, we would like to think about incorporating a more realistic breast model into the simulation.

Because the breast is a low-contrast subject, the choice of X-ray spectrum is important. Because the target/filter combination strongly affects the incident X-ray spectrum, it is important that we choose the most suitable target/filter combinations that reduce the radiation dose while maintaining image contrast.

References

1) Dance, D. R. “Monte Carlo calculation of conversion factors for the estimation of mean glandular breast dose”, Phys. Med. Biol. 35, 1211-1219 (1990)

2) Dance, D. R., Skinner, C. L., Young, K. C., Beckett, J. R., Kotre, C. J. “Additional factors for the estimation of mean glandular breast dose using the UK mammography dosimetry protocol”, Phys. Med. Biol. 45, 3225-3240 (2000)

3) Dance, D. R. “The Monte Carlo calculation of integral radiation dose in xeromammography”, Phys. Med. Biol. 25, 25-37 (1980)

4) Dance, D. R. And Day G J “The computation of scatter in mammography by Monte Carlo methods”, Phys. Med. Biol. 29, 237-47 (1984)

5) Horst Aichinger, Joachim Dierker, Sigrid Joite-Barfuβ, Manfred Säbel, (2004) “*Radiation Exposure and Image Quality in X-Ray Diagnostic Radiology*” Ohmsha

6) Hammerstein, G. R., Miller, D. W., White, D. R., Masterson, M. E., Woodard, H. Q., Laughlin, J. S. “Absorbed radiation dose in mammography” , Radiology 130, 485-491 (1979)

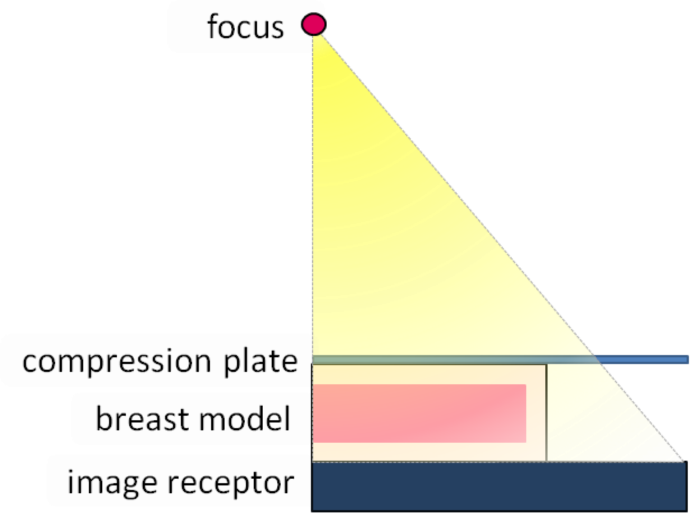

Figure 1. Geometry that is used in Monte Carlo calculations.

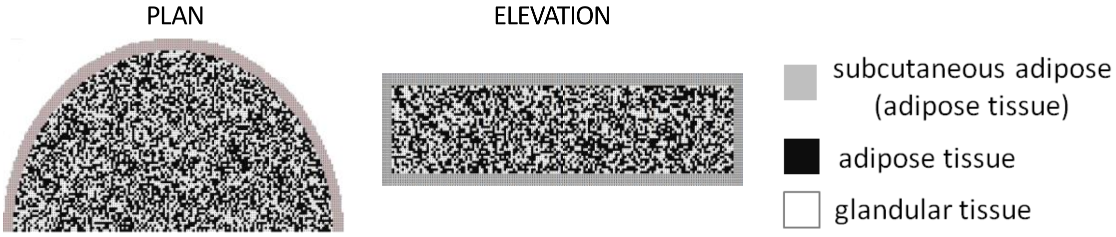

Figure 2. The standard breast model phantom.

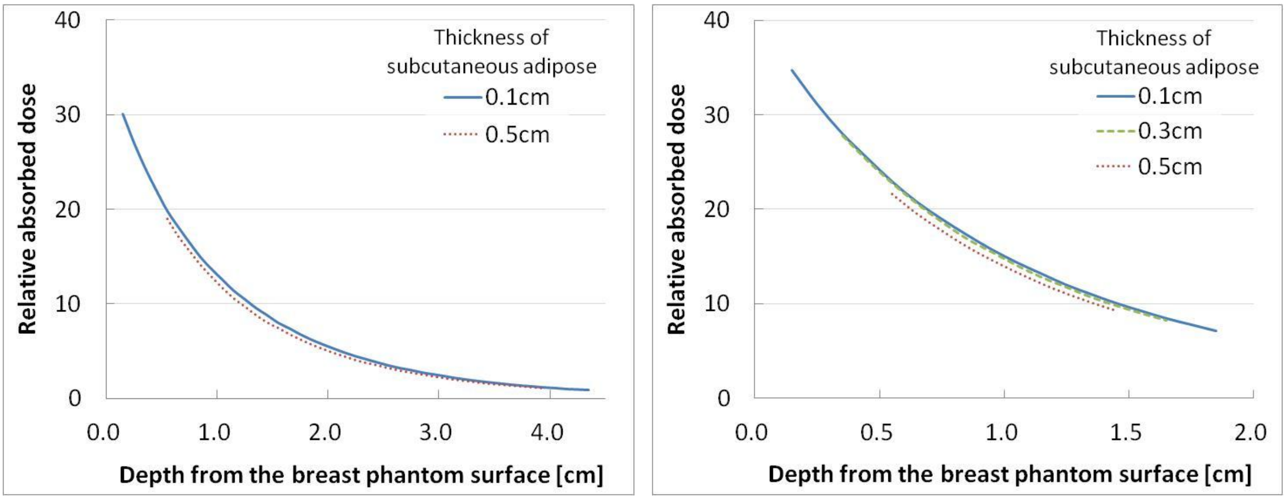

Figure 3. Relative absorbed dose in a phantom of thickness 4.5 cm

Figure 4. Relative absorbed dose in a phantom of thickness 2.0 cm.

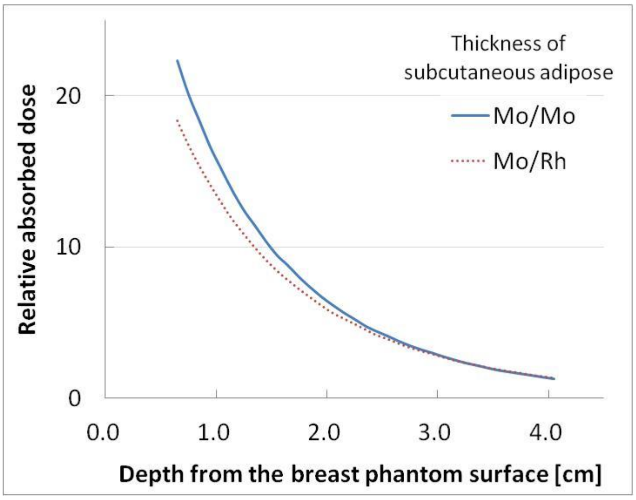

Figure 5. Relative absorbed dose in Mo target.

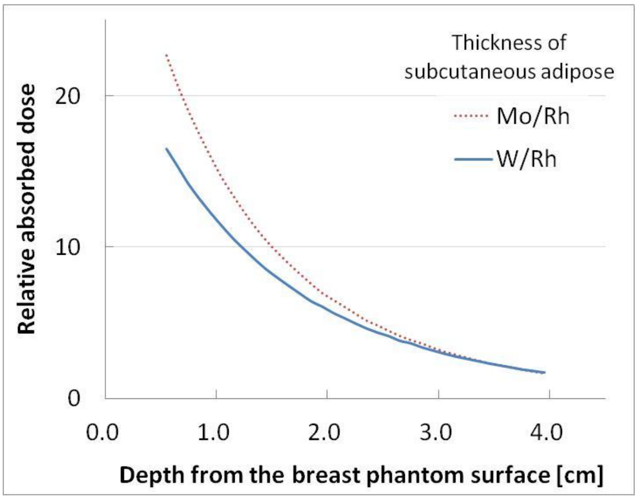

Figure 6. Relative absorbed dose in Rh filter.

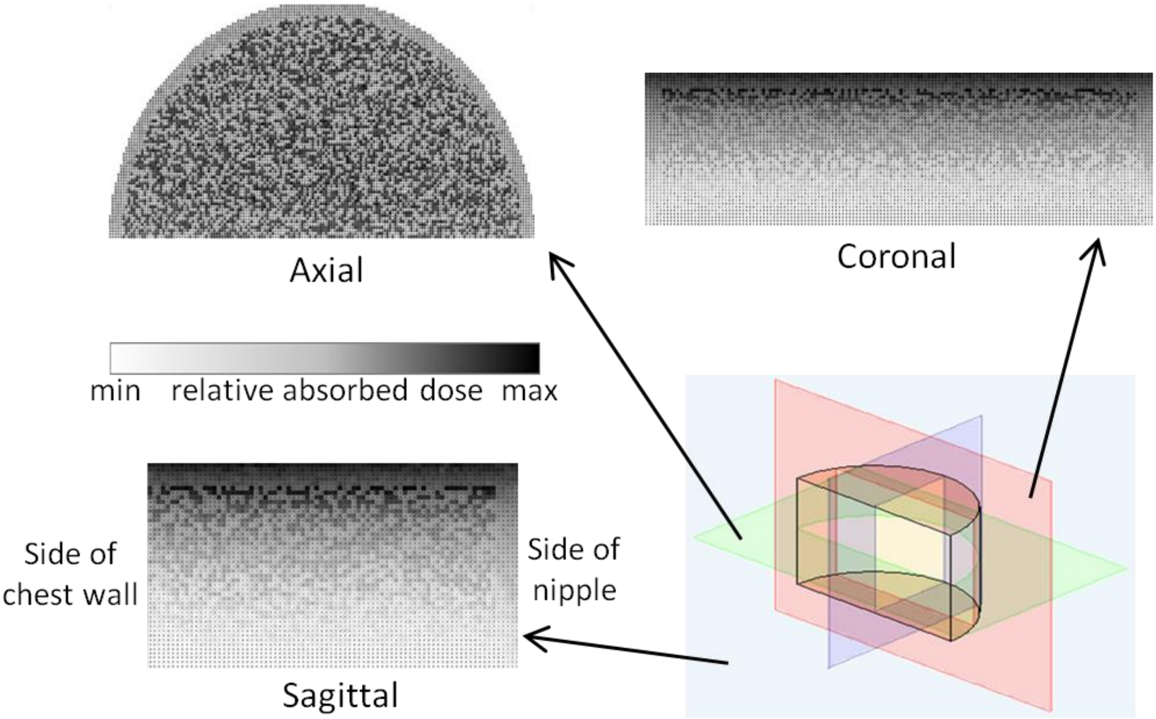

Figure 7. Absorbed dose distribution

INVESTIGATION OF PHYSICAL CHARACTERISTIC FOR HIGH DEFINITION MULTILEAF COLLIMATOR

Y. Iwamoto[1], H. Takagi[2], S. Hashinoguchi[2], H. Fujiwara[2], M. Tamura[1], T. Rachi[1],
Y. Obata[1, 3], T. Shimozato[4], and M. Komori[1]

[1]Department of Radiological and Medical Laboratory Sciences, Nagoya University,
Graduate School of Medicine, Nagoya 461-8673, Japan
[2]Ogaki Municipal Hospital, Ogaki 503-8502, Japan
[3]Ichinomiya Municipal Hospital, Ichinomiya 491-8558, Japan
[4]Iwata City Hospital, Iwata 438-8550, Japan
e-mail: iwamoto.yasushi@e.mbox.nagoya-u.ac.jp

Abstract

In radiation therapy, e.g., conformal radiotherapy and intensity modulated radio therapy (IMRT), multileaf collimator (MLC) is controlled to reduce exposure dose for normal tissue and to irradiate efficiently a tumor volume. Then, the dose distribution is affected by the transmission through the MLC and Tongue-and-Groove effect. In this study, we calculated the transmission through high definition multileaf collimator (HD MLC) and compared the differences with various materials of the MLC by Monte Carlo simulation. The structure of Novalis Tx (linear accelerator) and HD MLC were programmed with CGView. The energy and the FWHM of an incident electron were set to 6.0 MeV and 3.0 %, respectively. Secondary collimators (Jaw) were opened and the HD MLC was closed. The material of HD MLC was changed from tungsten to tantalum, osmium, lead and bismuth. The smallest transmission of materials was obtained with osmium, followed in order by tungsten, tantalum, lead and bismuth. Higher the material density is, smaller the transmission is.

1. Introduction

Radiation therapy has been constantly improved by new technical developments. In these new techniques, for example, multileaf collimator (MLC) allows delivery to complex in radiation therapy, e.g., intensity modulated radio therapy (IMRT). The MLC moves during the delivery and shapes suitable fields for the target volume. The dose distribution of conformal radiotherapy is homogeneous, but the dose distribution of IMRT is heterogeneous by dose intensity. Multiple beams are piled up; as a result, it is efficiently to reduce the exposure dose for a normal tissue and to irradiate a target volume.

The MLC has been developed by various corporations, Varian©, SIEMENS©, etc. and each has different characteristic. First, the equipped location is different by a kind of MLC. One is the upper side of a linear accelerator (linac) head, another is the lower side of a Linac head and the other is the tip of linac head. Second, the leaf of MLC is made of tungsten and leaf width is 10.0, 5.0, 3.0, 2.5 mm, etc. at isocenter. For example, the one of the MLC produced by Varian© is high definition MLC (HD MLC). HDMLC has 32 pairs of 2.5 mm inner leaf at isocenter, 26 pairs of 5.0 mm outer leaf at isocenter and 2 pairs of 7.0 mm outer-most leaf at isocenter, so max beam size by HD MLC is 22×40 cm^2.Third, the configuration of the MLC leaf is also various. The MLC has the structure called "Tongue-and-Groove" and the leaf end is rounded (Figure 1 and Figure 2) [1, 2]. The Tongue-and-Groove effect, leaf transmission (leaf side and end transmission), and abutting leaf leakage affect the dose distribution [3].

The purpose of this study was to calculate the transmission through the HD MLC by EGS5 (Electron Gamma Shower ver. 5) and to compare materials of the HD MLC for the leaf transmission.

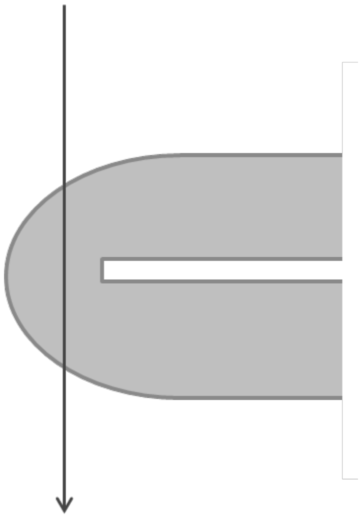

Figure 1 Shape of HD MLC and transmission and leaf end transmission.

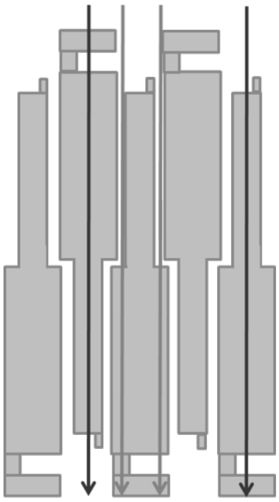

Figure 2 Shape of HD MLC and transmission and interleaf / intraleaf transmission.

2. Materials and Methods

2.1 Measured and simulated transmission

The leaf transmission was measured by using 6MV photons generated from a Varian Novalis Tx equipped with a 120 leaf HD MLC. All exposures were made using 500MUs. Secondary collimators (Y Jaw, X Jaw) were opened to 30 × 30 cm^2 and the HD MLC was closed as positioned at 0 cm. The measurements were performed using an ionization chamber (CC13, iba Dosimetry) and a diode detector (SFD, iba Dosimetry) in 3D water phantom and the source surface distance (SSD) was 90 cm. Dose profiles were measured across X axis(leaf motion direction), Y axis(leaf motion perpendicular direction) and 5 cm off center of Y axis(Figure 3).

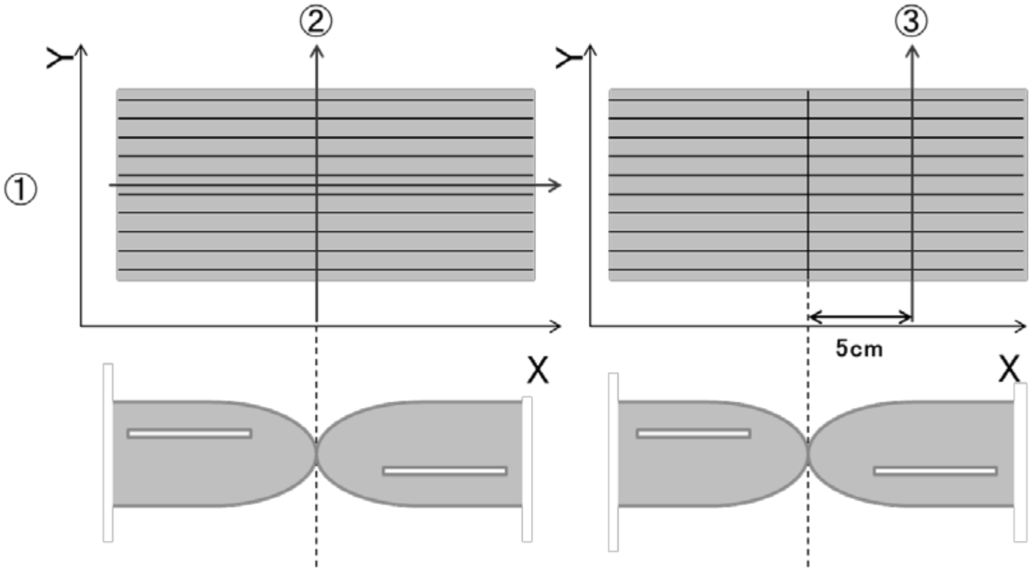

Figure 3 Location and direction of measurement of dose profile. ① center of X axis(leaf motion direction), ② center of Y axis(perpendicular leaf motion direction) and ③ 5 cm off center of Y axis

With Monte Carlo (MC) simulation code EGS5, the transmission was calculated using 6MV photons generated from Varian Novalis Tx equipped with the 120 leaf HDMLC. Novalis Tx is constructed of a target, primary collimators, a monitor chamber, a mirror, secondary collimators (Y Jaw, X Jaw), the HD MLC, and light field reticle. The HD MLC has the characteristic structures which are mechanical guides and screw holes, and rounded leaf ends [4, 5]. We simulated those in CGView. The energy and the FWHM of an incident electron are 6.0 MeV and 3.0 %, respectively. The aperture of the secondary collimators was 30 × 30cm^2 and that of the HD MLC was 0 × 0 cm^2. The calculating voxel size is 0.1 × 0.4 × 0.1 cm^3. Dose profiles across X axis were calculated and compared to those measured with an ionization chamber and a diode detector.

2.2 Changed materials of HD MLC

The transmissions were calculated changing from tungsten that is the material of the HD MLC to tantalum, osmium, lead and bismuth. The atomic numbers and physical densities of tungsten, tantalum, osmium, lead and bismuth are shown Table 1. Dose profiles across X axis were calculated and compared to that of tungsten of HD MLC.

Table 1 Materials of HD MLC for comparison

	Tantalum	**Tungsten**	**Osmium**	**Lead**	**Bismuth**
Atomic number	**73**	**74**	**76**	**82**	**83**
Density (g/cm^3)	**16.69**	**19.25**	**22.59**	**11.34**	**9.78**

3. Results and Discussions

3.1 Measured and Simulated transmission

Figure 4 shows the simulated transmission compared with previously measured one (Dayananda at 2011) [3]. For dose distribution at a center, leaf end transmission with EGS5 is good agreement with the measurement.

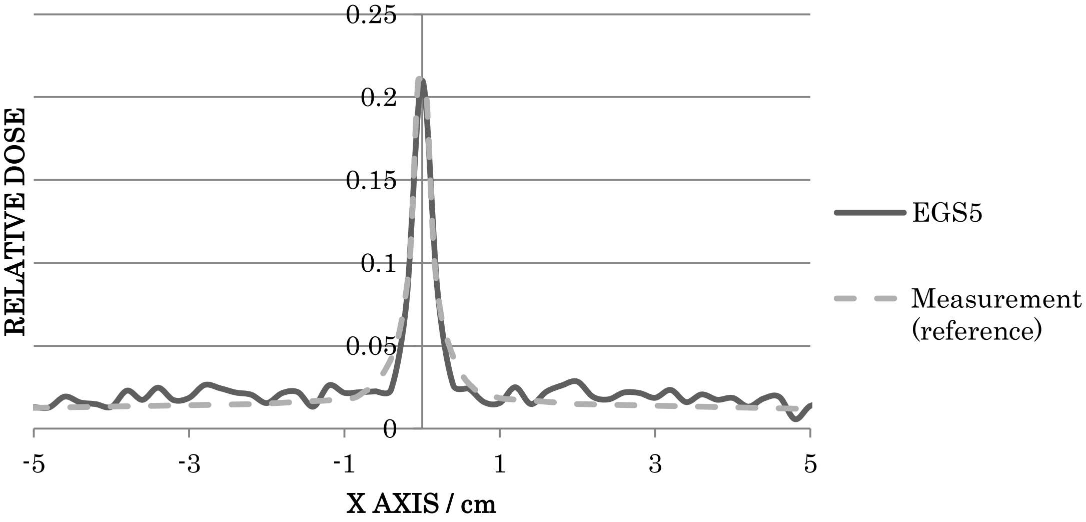

Figure 4 Line profiles across center of X axis for 6 MV photon beam measured and simulated at a depth of 10 cm in 3D water phantom.

Figure 5 shows the simulated transmission across center of Y axis compared with measured one. The result of the CC13 shows a relatively straight curve, meanwhile, the result of the SFD were a wavy curve, because of the different active volume of detectors. The cavity volume of the CC13 is 0.13 cc, on the other hand, the diameter of active area and the thickness of active volume of the SFD is 0.6 mm and 0.06 mm, respectively. When the EGS5 profiles are compared with the result of the CC13 and the SFD, there is approximately 30 % difference at both end of curve. In contrast, there is relatively good agreement in closer to the center of the curve.

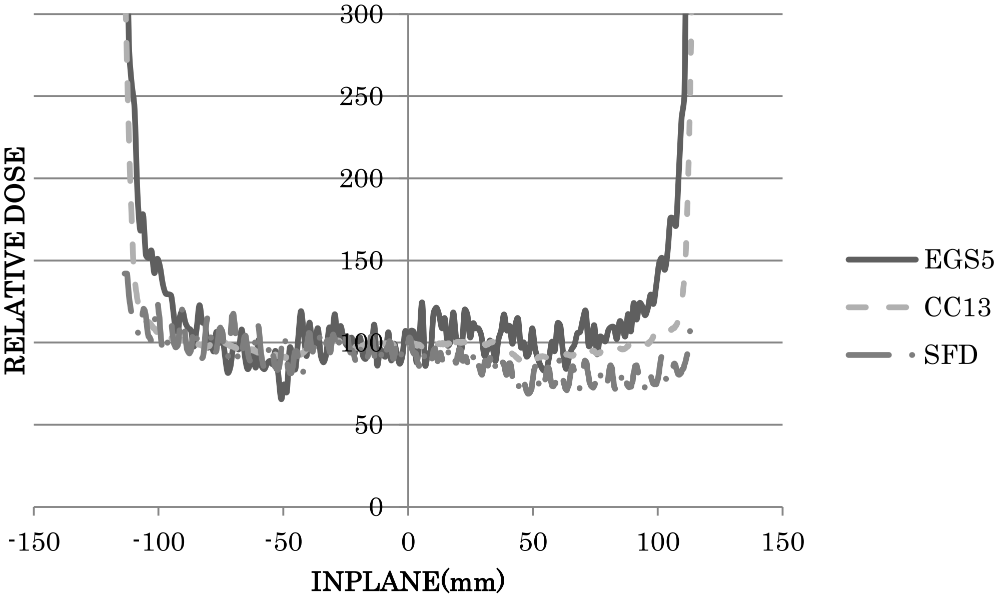

Figure 5 Line profiles across center of Y axis for 6 MV photon beam measured and simulated at a depth of 10 cm in 3D water phantom.

Figure 6 shows the simulated transmission across 5 cm off center of Y axis compared with measured one. From leaf transmission of the HD MLC, profile of EGS5 is a wavy curve. However, profiles of EGS5 and measurements are in relatively agreement.

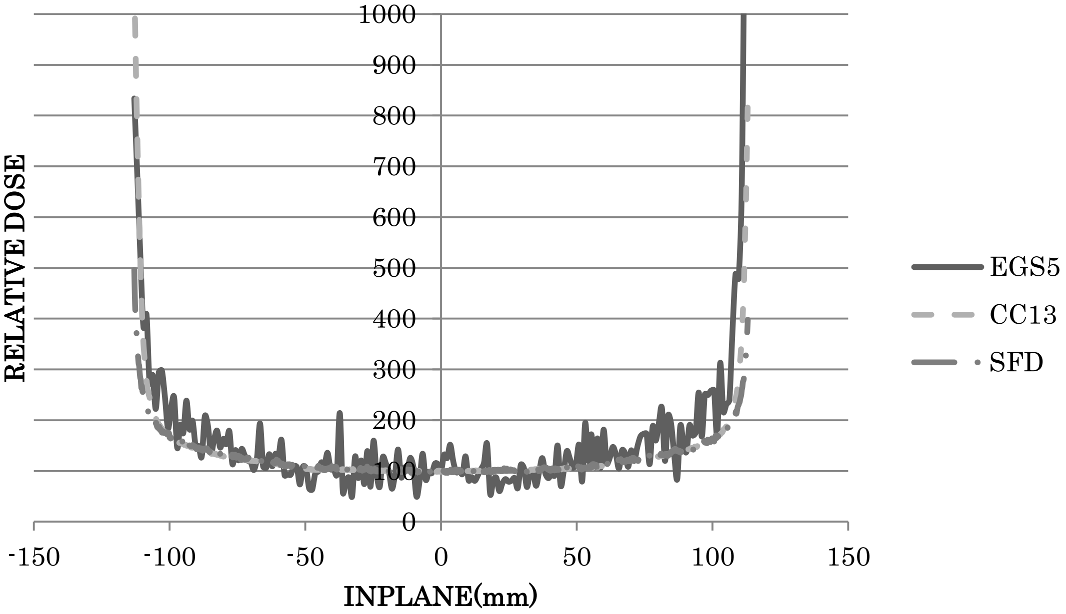

Figure 6 Line profiles across 5 cm off center of Y axis for 6 MV photon beam measured and simulated at a depth of 10 cm in 3D water phantom.

3.2 Changed materials of HD MLC

Figure 7 shows line profiles across the center of X axis for comparison of tungsten and other materials for the HD MLC. The material with the least transmission is osmium and the material with the most transmission is bismuth. The transmissions of bismuth, lead, tantalum, and osmium are 3.36 times, 2.61 times, 1.42 times, and 0.39 times as large as that of tungsten, respectively.

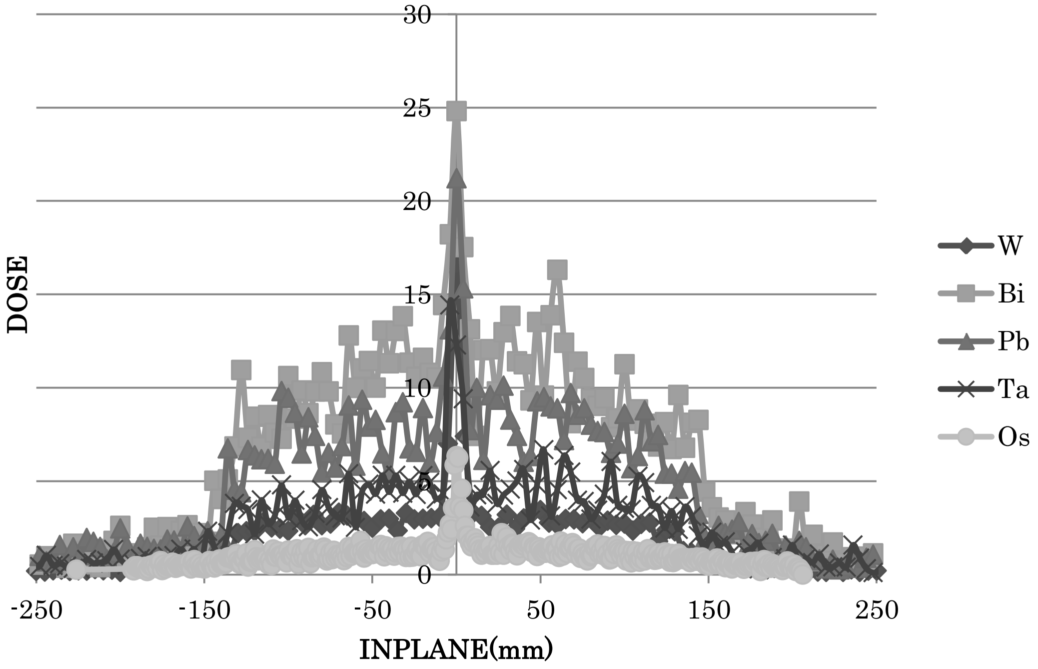

Figure 7 Comparison of tungsten and other materials for HD MLC. Line profiles across center of X axis.

Figure 8 shows line profiles across the center of Y axis for comparison of tungsten and other materials for the HD MLC. The material with the least transmission is osmium and the material with the most transmission is bismuth. The transmissions of bismuth, lead, tantalum, and osmium are 1.96 times, 1.73 times, 1.14 times, and 0.82 times as large as that of tungsten, respectively.

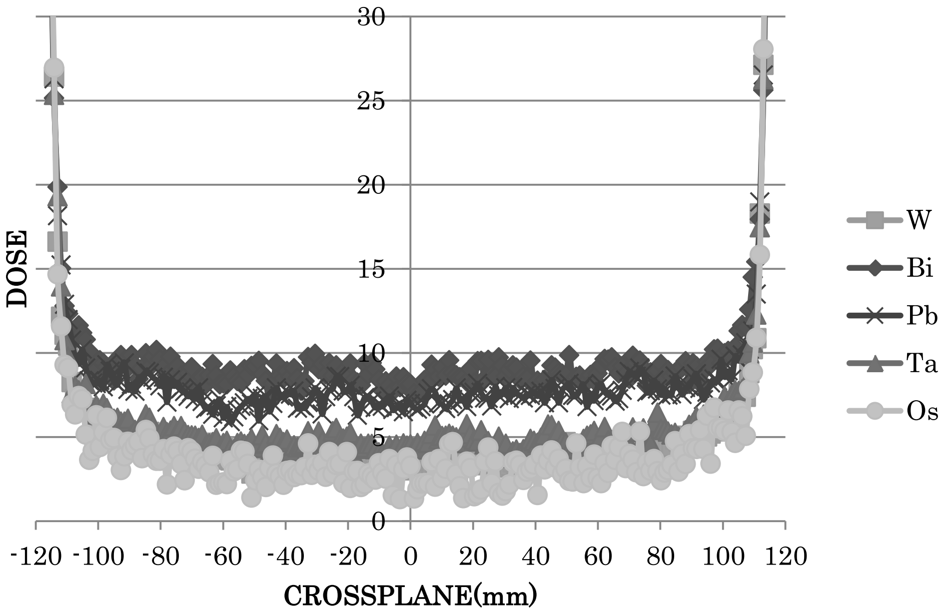

Figure 8 Comparison of tungsten and other materials for HD MLC. Line profiles across center of Y axis.

Figure 9 shows line profiles across 5 cm off center of Y axis for comparison of tungsten and other materials for the HD MLC. The material with the least transmission is osmium and the material with the most transmission is bismuth. The transmissions of bismuth, lead, tantalum, and osmium are 2.19 times, 1.86 times, 1.21 and 1.01 times as large as that of tungsten, respectively.

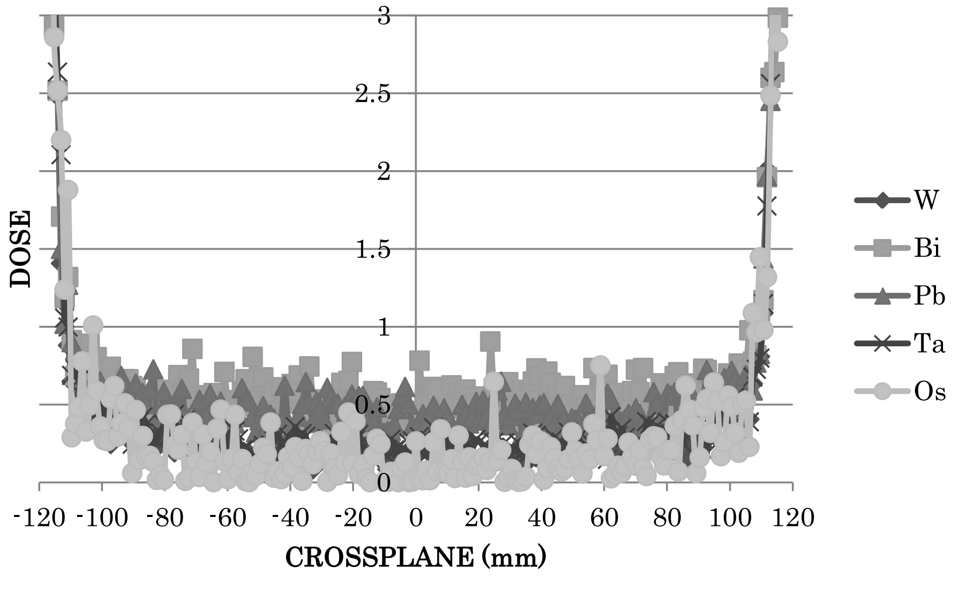

Figure 9 Comparison of tungsten and other materials for HD MLC. Line profiles across 5 cm off center of Y axis.

From these results, the transmission of osmium is the smallest, tungsten, tantalum, lead and bismuth in turn. The main interaction of photon in radiation therapy is Compton effect. The mass attenuation coefficient of Compton effect is in proportion to the ratio of atomic number to mass. The ratio of atomic number to mass is approximately 0.4 - 0.5 for all materials. Therefore the transmission is influenced by physical density. The physical densities of tungsten, osmium, tantalum, lead bismuth are 19.25, 22.59, 16.69, 11.34, and 9.78 g/cm^3, respectively. From our results, therefore, larger physical density is, smaller transmission is.

4. Conclusions

We could simulate tongue and groove structure, rounded leaf end, and others of the HD MLC using EGS5 with CGView. Changing the material of the HD MLC, the minimum transmission simulated with osmium was 39 % for X axis and 82 % for Y axis. In order to reduce the transmission of the HD MLC, it is adequate to use higher physical density material.

References

1) S. Y. Jang, O. N. Vassiliev, H. H. Liu, R. Mohan, and J. V. Siebers, "Development and commissioning of a multileaf collimator model in Monte Carlo dose calculations for intensity-modulated radiation therapy," Med Phys. **33**, 770-781 (2006).
2) T. LoSasso, C. Chui, and C. C. Ling, "Physical and dosimetric aspects of a multileaf collimation system used in the dynamic mode for implementing intensity modulated radiotherapy," Med. Phys. **25**, 1919-1927 (1998).
3) T. Losasso, "IMRT DELIVERY PERFORMANCE WITH AVARIAN MULTILEAF COLLIMATOR," Int. J. Radiat Oncol Biol. Phys. **71**, S85–S88 (2008).
4) C. Borges, M. Zarza-Moreno, E. Heath, N. Teixeira, and P. Vaz, "Monte Carlo modeling and simulations of the High Definition (HD120) micro MLC and validation against measurements for a 6 MV beam," Med. Phys. **39**, 415-423 (2012).
5) M. K. Fix, W. Volken, D. Frei, D. Frauchiger, E. J. Born, and P. Manser, "Monte Carlo implementation, validation, and characterization of a 120 leaf MLC," Med. Phys. **38**, 5311-5320 (2011).

The improvement of discrepancy between radiotherapy treatment planning system and verification system using Effective Density Method

**S.Kumagai[1], M.Okajima[2], H.Takaya[2], N.Arai[3], K.Waga[3], T.Tanaka[3],
M.Yasuda[3], K.Takimoto[4], J.Kotoku[1,2], T.Kobayashi[1,2]**

[1]*Graduate School of Radiological Technology, Teikyo Univeristy, Tokyo 173-0003, Japan*
[2]*Department of Radiological Technology Faculty of Medical Technology, Teikyo University, Tokyo 173-0003, Japan*
[3]*Central Rdiology Division, Teikyo University Hospital*
[4]*Euro MEDITECH CO.,LTD, Tokyo 141-0022, Japan*
e-mail: shinobu@med.teikyo-u.ac.jp

Abstract

It has been reported that the planned dose calculated by Pinnacle[3] showed about 2% discrepancy from the measured one. This discrepancy was also confirmed by the comparison of EGS5 simulations for PMMA phantom regarded as Delta[4] detector and for a high density water phantom as a virtual phantom in Pinnacle[3]. According to the guideline for IMRT, which recommends the maximum tolerance of dose deviation within 3%, this discrepancy is not negligible at all. One of the aims of this study was to understand what may cause this discrepancy. Another EGS5 simulation was made to examine the contribution of primary photon flux to absorbed dose in each phantom. As a result the contribution of primary photon flux in high density water phantom showed steeper decrease compared to one in PMMA phantom. This indicated that the electron density used in Pinnacle[3] was overestimated so that the primary photon flux was attenuated faster than that in PMMA phantom, supported by the fact that PMMA has larger density among other commonly used phantom materials. Then the effective density method was developed in order to eliminate the discrepancy. The effective density was defined so as to provide the same linear attenuation coefficient as PMMA in the water kernel used in Pinnacle[3]. Using an average effective density, the discrepancy in PDDs was reduced to less than 1%. The effective density method was also applied to a clinical case with remarkable improvement of Gamma index.

1. Introduction

In recent years intensity-modulated radiation therapy (IMRT) became available for the radiological cancer treatment. IMRT, relying on the advanced computerized technology, can deliver precise radiation dose to tumor while minimizing dose to surrounding healthy tissues. Then the verification of radiotherapy planning has become more crucial task to achieve safe and accurate dose delivery. Pinnacle^3[1,2,3,4] was used for planned dose calculation for this study. In the meanwhile, the new generation of dose monitors has emerged, such as Delta^4[5] used in this study. Inside Delta^4 there are 1069 newly developed p-type diodes mounted on two planes orthogonally placed in the cylindrical PMMA phantom. These detector arrays enable fast and accurate 3D verification of a delivered dose distribution.

However, it was reported that the planned dose calculated by Pinnacle^3 was found to be underestimated by 2% compared to the delivered one[6]. In addition, based on the CT scanned data for Delta^4 phantom, Pinnacle^3 predicted the density of PMMA phantom smaller than expected[5]. There appeared to be some problem existed whenever Pinnacle^3 was used for the high density materials. Since maximum tolerance of 3% for the dose deviation has been recommended according to the guideline for IMRT, this discrepancy should not be neglected. Goals of this study are to figure out what causes this discrepancy and to find out an effective measure to reduce this discrepancy.

2. Materials and Methods

2.1 Simulations of PDD for phantoms with different densities

To verify whether the difference in material composition explains the reported discrepancy of 2%, Monte Carlo simulations using EGS5[7] have been conducted. Two different material input files were prepared for simulations; one for modeling the Delta^4 phantom which is made of PMMA and another one for modeling the water kernel used in Pinnacle^3, in which PMMA phantom is treated as high density water possessing same density as PMMA, i.e. $1.19\ \mathrm{g{\cdot}cm^{-3}}$.

The geometry used for EGS5 simulations is shown in Figure 1. Absorbed doses along the central axis of the incident photon beam were obtained at 35 points with the same detection volume of $1.0 \times 1.0 \times 0.6\ \mathrm{cm}^3$ to calculate the PDD. 4MV and 10MV X-ray beams from Varian linear accelerator were modeled with field size of $10 \times 10\ \mathrm{cm}^2$ on the surface of the phantom placed at 100 cm source-to-surface distance (SSD). Energy spectra of X-ray beams were taken from the published data[8]. The number of X-ray beams used in each simulation was 2×10^9, which ensured the statistical uncertainties less than 0.5% at each detection volume. The cut-off energies for transport calculation of electron (ECUT) and photon (PCUT) were set to 521 keV and 10 keV throughout this study, respectively.

2.2 Effective Density Method

The effective density method was developed to eliminate the discrepancy between planned and delivered dose to PMMA phantom. The effective density method provides an appropriate input density to Pinnacle^3 so that the attenuation of photon flux in PMMA phantom can be retrieved in the water kernel virtually produced in Pinnacle^3 system. The effective density, $\rho_{\mathrm{eff}}(E)$, was defined as follows:

$$\mu_{\mathrm{PMMA}}(E) = \left(\frac{\mu}{\rho}\right)_{\mathrm{PMMA},E} \times \rho_{\mathrm{PMMA}} = \left(\frac{\mu}{\rho}\right)_{\mathrm{water},E} \times \rho_{\mathrm{eff}}(E)\,,$$

where $\mu_{\mathrm{PMMA}}(E)$ represents the linear attenuation coefficient for PMMA at energy E, ρ_{PMMA} represents the density of PMMA and is equal to 1.19 $\mathrm{g \cdot cm^{-3}}$, and $(\mu/\rho)_{\mathrm{PMMA},E}$[9] and $(\mu/\rho)_{\mathrm{water},E}$ [9] represent mass attenuation coefficients at energy E for PMMA and water, respectively.

Following this definition, the effective density can be obtained at any photon energy requested. However, there is only one density input allowed for the Pinnacle^3 system. Therefore the average effective density, ρ_{ave} , should be evaluated by taking the weighted average of $\rho_{\mathrm{eff}}(E)$ over relevant photon energy range:

$$\rho_{\mathrm{ave}} = \int_0^{E_0} f(E) \cdot \rho_{\mathrm{eff}}(E)\, dE\,,$$

where E_0 represents the maximum photon energy and $f(E)$ represents the probability density function which is calculated from the photon spectrum. The dose profiles for PMMA phantom were calculated by Pinnacle^3 using the average effective densities for 4MV and 10MV X-ray beams. Table Ⅰ summarized the calculation parameters used in Pinnacle^3.

2.3 Measurement of dose profile for PMMA phantom

Figure 2 shows the experimental setup for PDD measurements. 4MV and 10MV X-ray beams from Varian CLINAC21-EX were delivered to the PMMA phantom with field size of $10 \times 10\ \mathrm{cm}^2$ on the surface of the phantom. The dose profile was measured at 3cm, 5cm,10cm, and 15cm from the surface of the PMMA phantom. The ionization chamber (Semiflex 31010) was placed at source-chamber distance (SCD) of 100cm. The measurement setups are listed in Table Ⅱ.

3. Results

3.1 Comparison of the simulated PDDs

Figure 3(a) shows a comparison of the simulation results of PDD for two different phantoms for 4MV X-ray beams. The PMMA phantom, modeling Delta^4, is denoted by PMMA and the high density water phantom, modeling the water kernel in Pinnacle^3, is denoted by HDW. Figure 3(c) represents the difference between the two results. The relative difference between two phantoms, $\Delta\mathrm{PDD}(d)$, was defined as follows:

$$\Delta\mathrm{PDD}(d) = \frac{\mathrm{PDD}(d)_{\mathrm{HDW}} - \mathrm{PDD}(d)_{\mathrm{PMMA}}}{\mathrm{PDD}(d)_{\mathrm{PMMA}}}\,,$$

where d represents the depth from the phantom surface. Figure 3 shows that $\Delta\mathrm{PDD}(d)$ spread with depth and reached -2% at 15cm from the surface. The similar results were obtained for 10MV X-ray beam.

3.2 Validation of the effective density method

3.2.1 Average Effective Density

To obtain the average effective densities, the probability density functions were determined from photon spectra for 4MV and 10MV X-ray beams in advance. Then averaging the effective densities has been taken over the appropriate photon energy range. As results, the average effective density of 1.16 $\mathrm{g \cdot cm^{-3}}$ for 4MV X-ray beams and 1.15 $\mathrm{g \cdot cm^{-3}}$for 10MV X-ray beams were obtained. These values were found to be about 3% less than the density of PMMA, i.e., 1.19 $\mathrm{g \cdot cm^{-3}}$.

3.2.2 Comparison of the measured dose and the calculated dose with average effective density

Using the average effective density derived above, the dose profile for PMMA phantom was calculated by Pinnacle[3]. Figure 4 shows the results compared with the measured doses and calculated doses with PMMA density, i.e. 1.19 $\mathrm{g \cdot cm^{-3}}$ for 4MV and 10MV X-ray beams, respectively. The relative difference between these doses, $\Delta D(d)$, was defined as follows:

$$\Delta D(d) = \frac{D(d)_\mathrm{c} - D(d)_\mathrm{m}}{D(d)_\mathrm{m}},$$

where $D(d)_\mathrm{m}$ represents the measured absorbed dose at depth d and $D(d)_\mathrm{c}$ represents the calculated one by Pinnacle[3]. The relative difference between measured doses and calculated doses with PMMA density became evident with depth and reached 3% at 15cm from the surface. On the other hand, the difference between measured doses and calculated doses with average effective density remained in less than 1% over all phantom depth.

4. Discussion

The reported discrepancy between planned doses and measured doses was confirmed by EGS5 simulations shown in Figure 3. The electron density used in Pinnacle[3], i.e. 3.97×10^{23} $\mathrm{electrons\ per\ cm^3}$, is 2.6% larger than the electron density of PMMA, i.e. 3.87×10^{23}. Due to this overestimation of electron density, the primary photon flux in the high density water phantom virtually produced in Pinnacle[3] was attenuated faster than expected by Compton scattering so that the absorbed doses were decreased more rapidly with depth compared to those in PMMA phantom. Figure 5 shows the result of EGS5 simulations of the dose profile due to the primary photon flux. Same parameters as previous ones were used for the simulations. The contributions to the dose profile from secondary photons were eliminated by using the Latch technique. Both profiles were normalized at maximum depth. The dose profile of high density water phantom shows steeper decrease compared to that of PMMA, which was predicted from above discussions. Figure 6 shows that about 40% of the absorbed dose appeared to be come from secondary (scattered) photons. It should be noted that this discrepancy between planned dose and measured dose became evident only because PMMA has exceptionally high density among other commonly used water equivalent phantoms shown in Figure 7. Whenever PMMA phantom is used for the verification of the planning dose predicted by Pinnacle^3, special care must be taken, because Pinnacle^3 cannot properly generate photon flux especially deep inside PMMA phantom.

Then the effective density method has been successfully developed in order to provide an appropriate distribution of photon flux on the high density water kernel in Pinnacle^3. By introducing the average effective density, the dose profile calculated by Pinnacle^3 has shown clear improvement, remaining the deviation relative to the measured dose profile within 1%.

As another validation the effective density method was applied to a clinical case. For the sake of clinical evaluation, Gamma index was often used. Gamma index is known to be an effective measure for the comparison of dose distributions, combining both dose difference (DD) and distance to agreement (DTA) into a single quantity. In this study, the criterion of Gamma index was set to 2% for DD and 2mm for DTA. Using the average effective density instead of PMMA density, Gamma index has been remarkably improved from 82.8% to 97.7% in this example shown in Figure 8.

5. Conclusions

The EGS5 simulations confirmed the reported discrepancy between measured and planned dose. This discrepancy was caused by the loss of primary photon flux due to the overestimation of electron density of the water kernel used in Pinnacle^3. This was also proved by the results of EGS5 simulations. The effective density method has been successfully developed so that the discrepancy was found to remain in less than 1%. The effective density method also applied for a clinical case Gamma index of a clinical case with remarkable improvement of Gamma index.

References

1) T. McNutt, "The ADAC Pinnacle^3 Collapsed Cone Convolution Superposition Dose Model," ADAC radiation therapy products, ADAC Laboratories Milpitas, CA, USA.
2) M. Khan, "Treatment Planning in Radiation Oncology second edition," Lippincott Williams &Wilkins. 63-77 (2007).
3) A. Ahnesjo," Collapsed cone convolution of radiant energy for photon beam dose calculation in heterogeneous media," Medical Physics. **16**, 577-592 (1989).
4) T. R. Mackie, J. W. Scrimqer, J. J. Battista, "A convolution method of calculating dose for 15-MV x rays," Medical Physics. **12**, 188-196 (1985).
5) V. Feygelman, K. Foster, D. Opp, et al., "Evaluation of a biplanar diode array dosimeter for quality assurance of step-and-shoot IMRT," Journal of Applied Clinical Medical Physics **10**, 3080 (2009).
6) J. L. Bedford, PJ. Childs, V. Nordmark, et al., "Commissioning and quality assurance of the Pinnacle^3 radiotherapy treatment planning system for external beam photons," The British Journal of Radiology. **76**, 163-176 (2003).

7) H. Hirayama, Y. Namito, A. F. Bielajew, S. J. Wilderman and W. R. Nelson,"EGS5 Code System," SLAC-R-730 (2005) and KEK Report 2005-8 (2005).

8) D. Sheikh-Bagher, D. W. O. Rogers, "Monte Carlo calculation of nine megavoltage photon beam spectra using the BEAM code," Medical Physics. **29**, 391-402 (2002).

9) M. J. Berger, J. H. Hubbell, S. M. Seltzer, et al., "XCOM: Photon Cross Section Database (version 1.5), National Institute of Standards and Technology, Gaithersburg, MD. http://physics.nist.gov/xcom (2010).

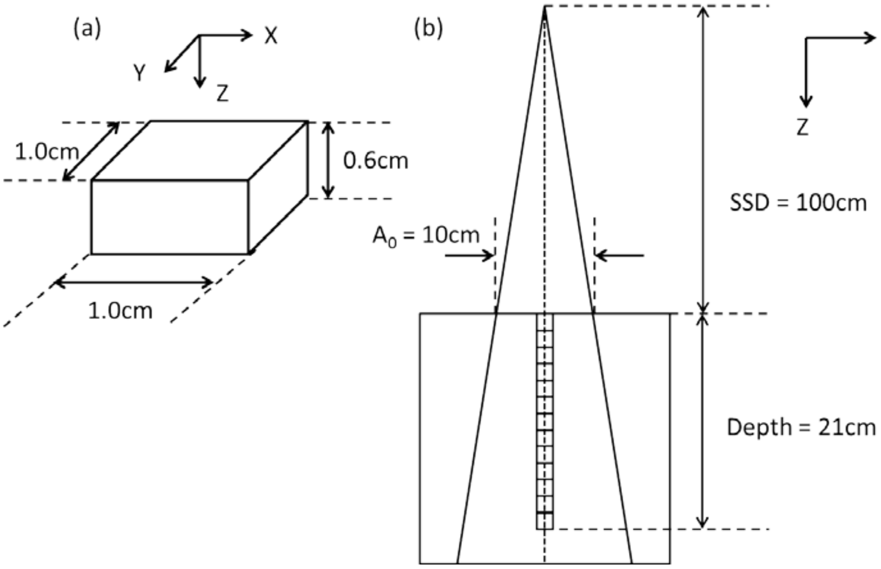

Figure 1. Geometry used for EGS5 simulations: (a) detection volume and (b) X-Z view.

Table Ⅰ. Calculation parameters used in Pinnacle^3.

Input density[g・cm^{-3}]	Physical density(1.19) Average Effective density(1.15,1.16)
Photon Energy [MV]	4, 10
Calculation Algorithm	CC Convolution/Superposition
Dose Grid [mm]	2.0

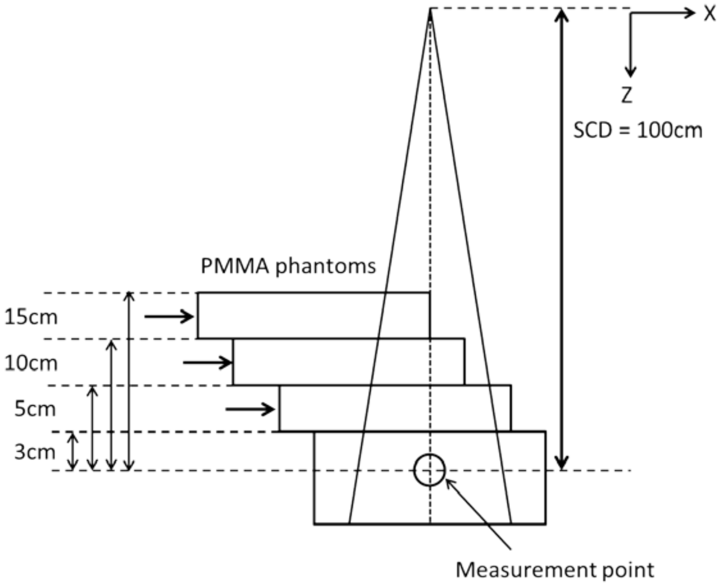

Figure 2. Experimental setup for PDD measurement.

TableⅡ. Setup for dose profile measurement.

Linac	Varian CLINAC 21-EX
Ionization Chamber	Semiflex 31010
Photon Energy[MV]	4,10
Monitor Unit[MU]	200
Dose Rate[Mumin^{-1}]	600
Phantom	Acrylic (MITSUBISHI RAYON CO.LTD)

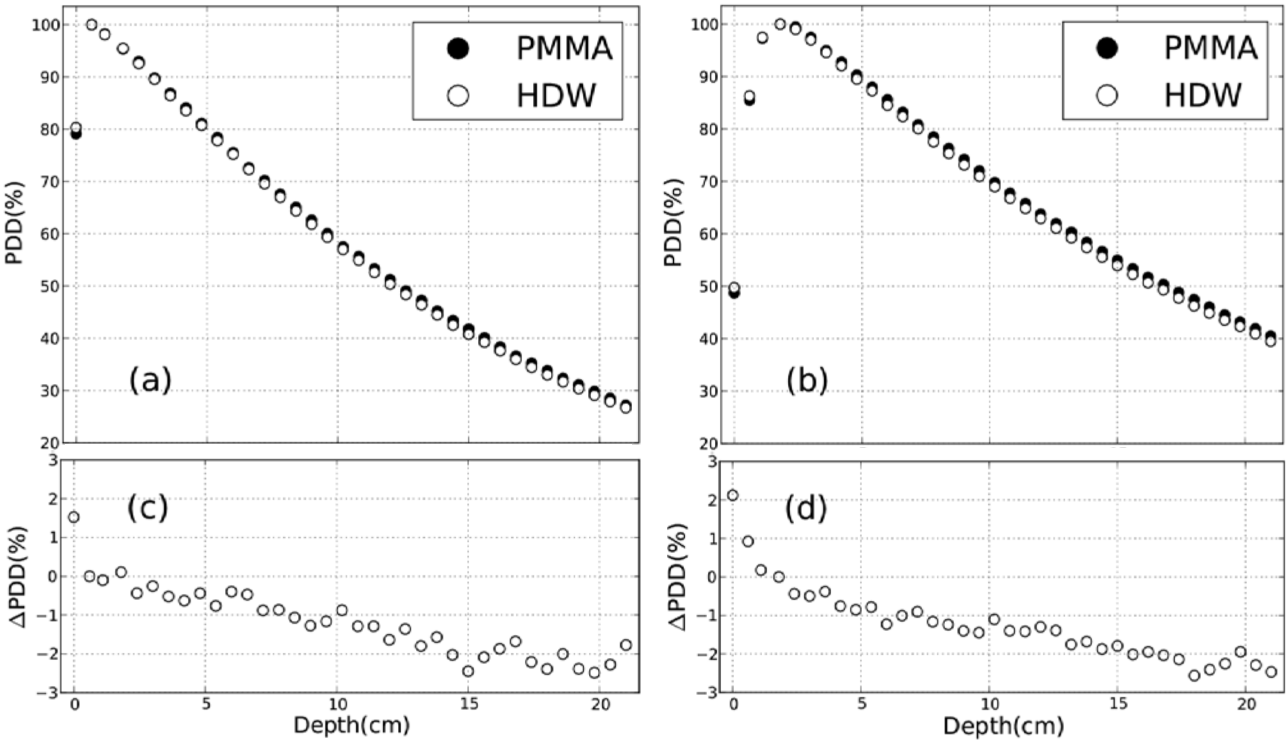

Figure 3. EGS5 simulation results. (a) and (b) represent simulation results for 4MV X-Ray beams and 10MV X-Ray beams, respectively. (c) and (d) represents the relative difference of PDDs for 4MV X-Ray beams and 10MV X-Ray beams, respectively.

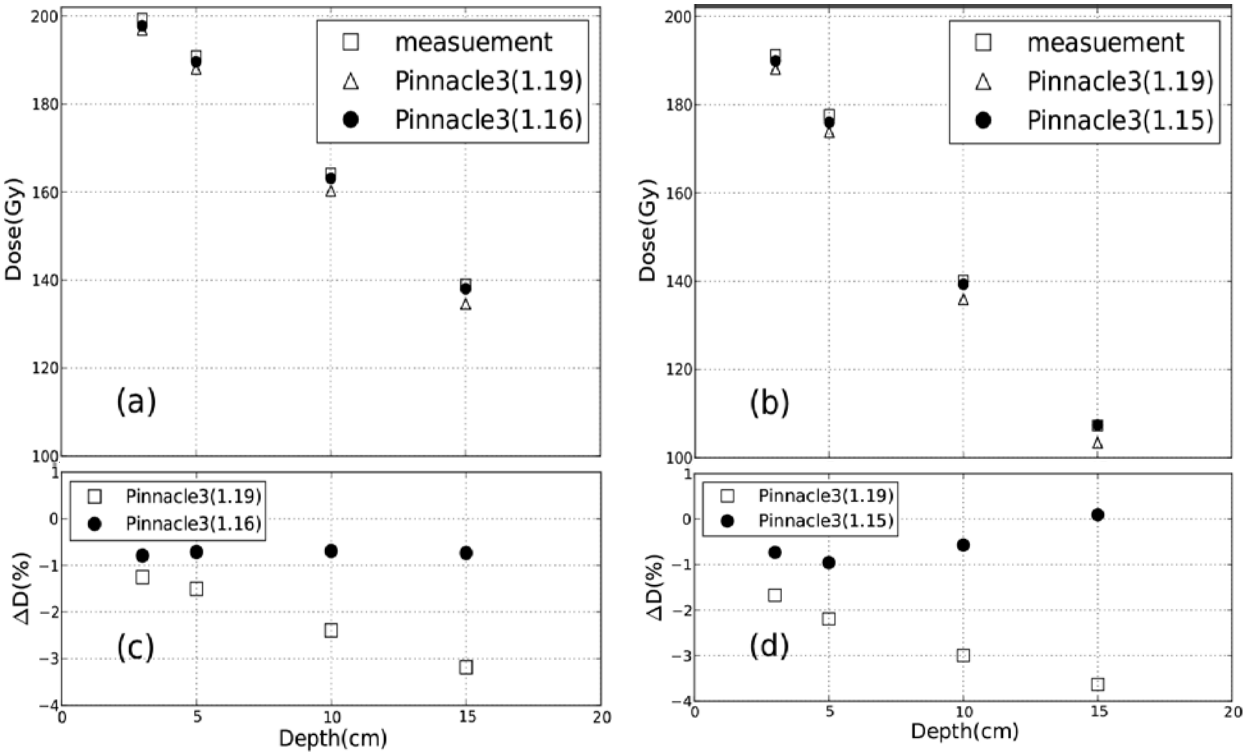

Figure 4. Comparison of measured dose and calculated dose: (a) dose profiles for 4MV X-Ray beams; (b) dose profiles for 10MV X-Ray beams; (c) relative differences to measured dose for 4MV X-Ray beams and (d) relative differences to measured dose for 10MV X-Ray beams. Pinnacle3(1.16) and Pinnacle3(1.15) represent the calculated dose with average effective density.

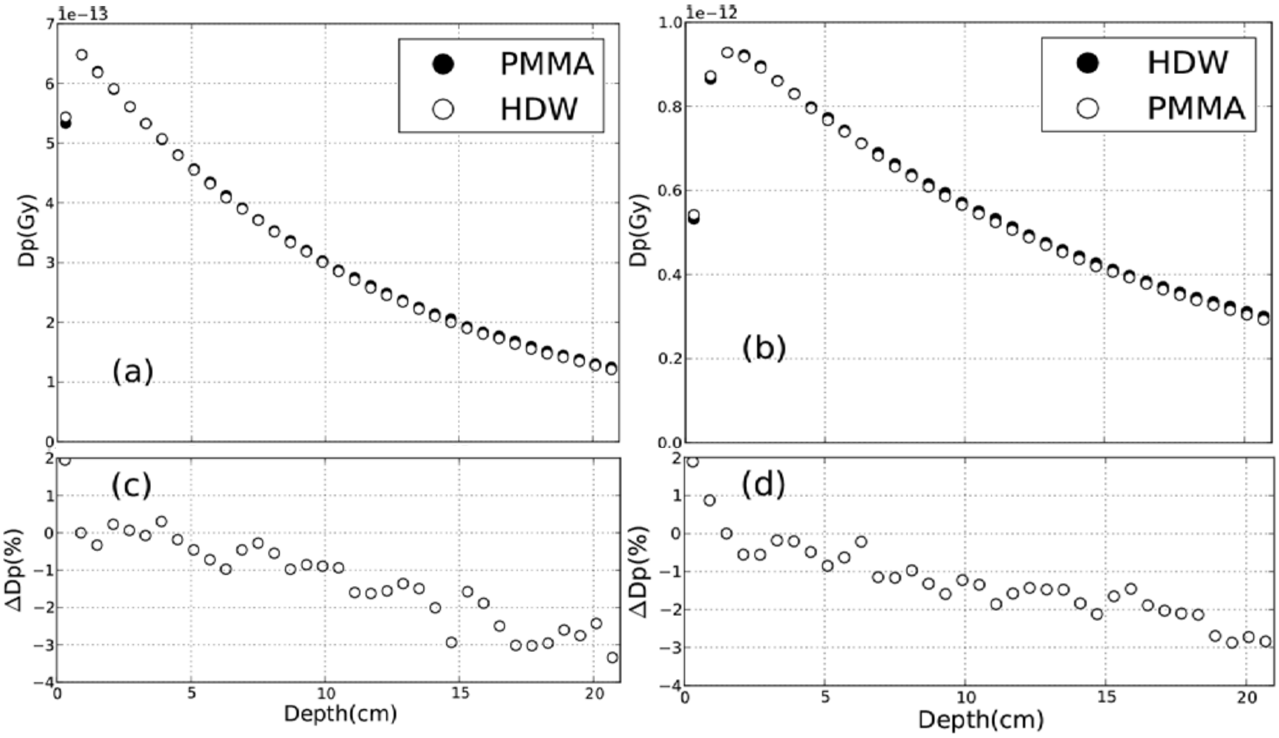

Figure 5. Simulation results for dose profile due to the primary photon flux (D_p) for PMMA phantom and high density water phantom(HDW) and the relative difference between two results (ΔD_p). Contributions from scattered photons are eliminated by using latch technique. (a) and (c) represent the results for 4MV X-Ray beams. (b) and (d) represent the results for 10MV X-Ray beams.

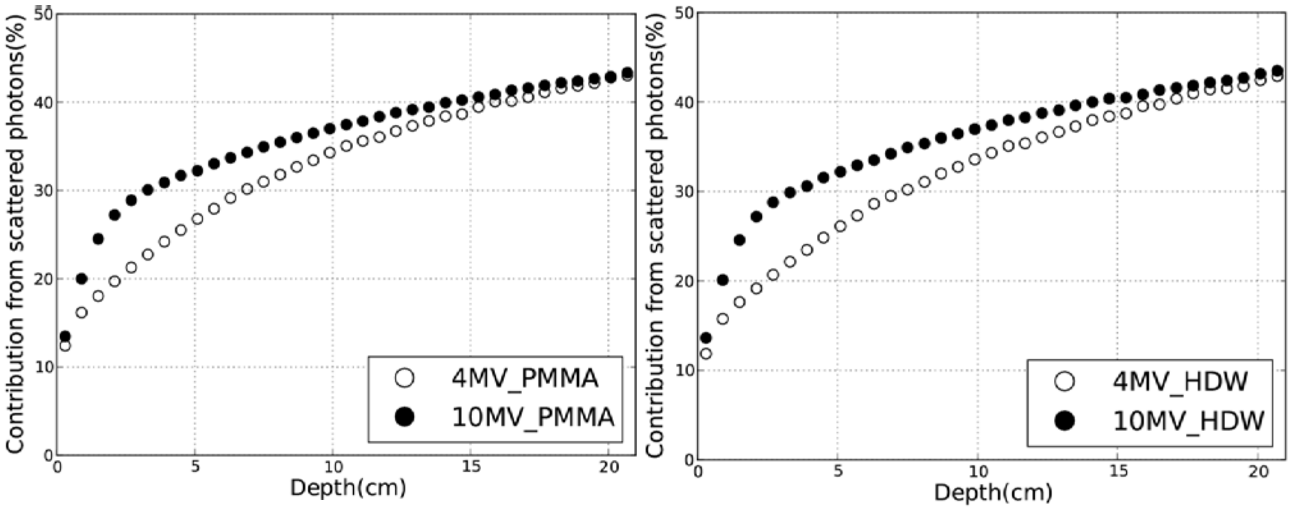

Figure 6. Contributions to absorbed dose from secondary (scattered) photons.

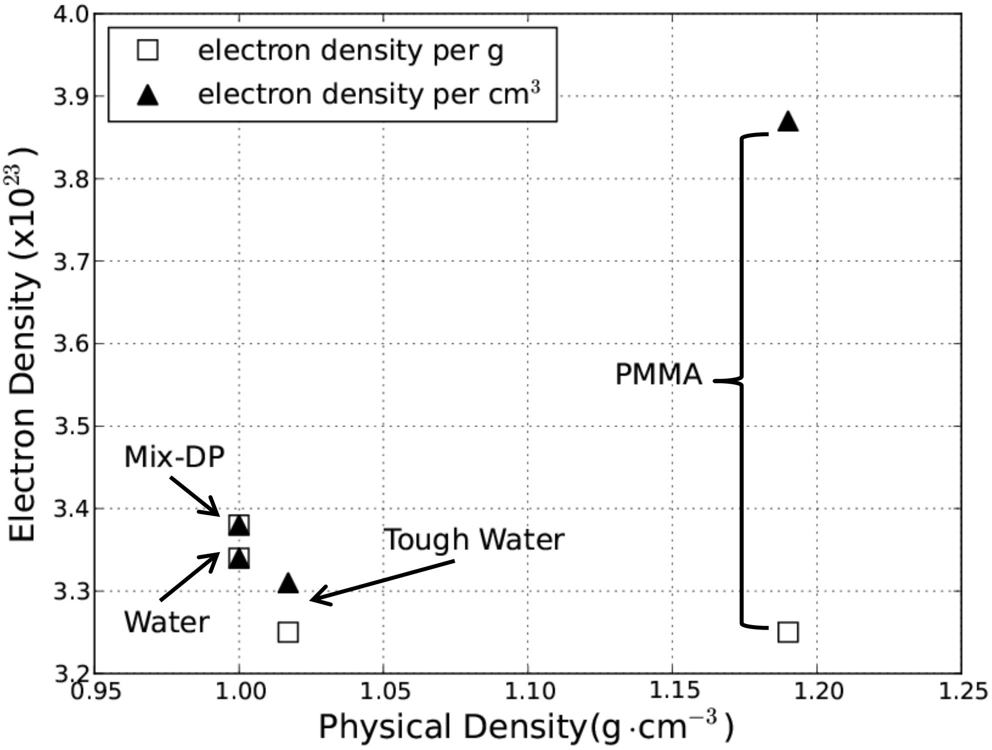

Figure 7. Electron densities for water equivalent phantom materials.

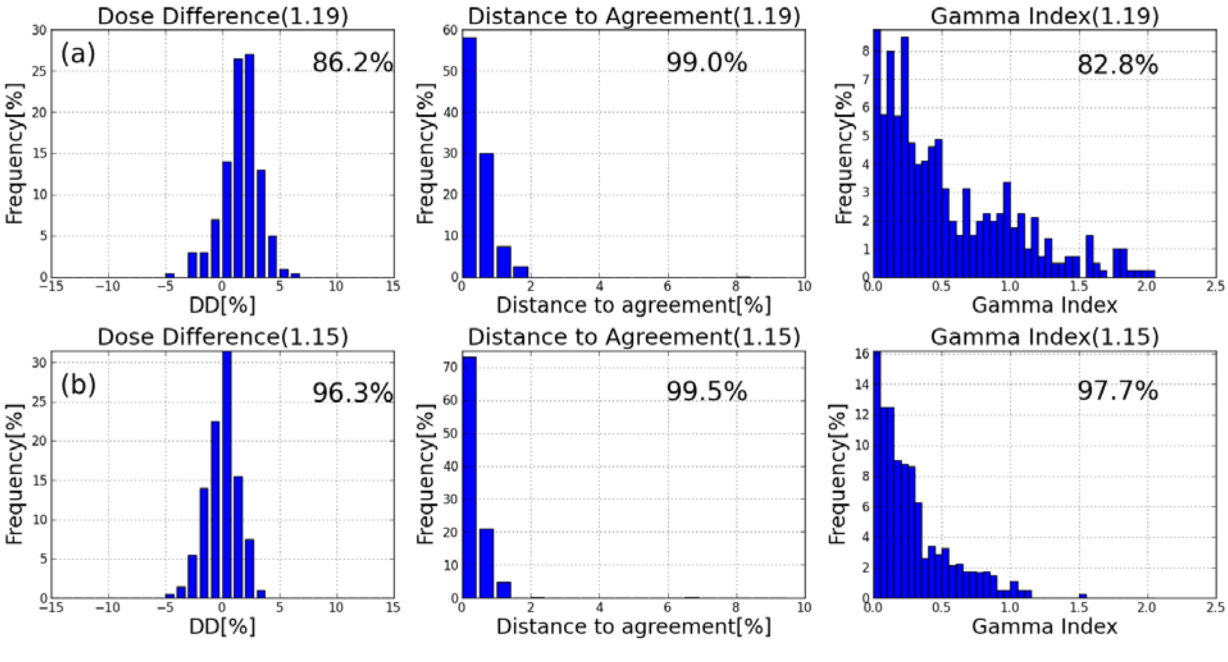

Figure 8. A clinical validation of the effective density method. Using the average effective density ($\rho_{\mathrm{ave}} = 1.15\,\mathrm{g\cdot cm^{-3}}$) instead of PMMA density ($\rho_{\mathrm{PMMA}} = 1.19\,\mathrm{g\cdot cm^{-3}}$), Gamma index has been remarkably improved.

STUDY OF COLLIMATOR SCATTER FACTOR (*Sc*) AND PHANTOM SCATTER FACTOR (*Sp*) USING MONTE CARLO SIMULATION

T.Rachi[1], Y.Iwamoto[1], M.Tamura[1], K.Ota[2], T.Shimosato[3], Y.Obata[4], and M.Komori[1]

[1]*Department of Radiological and Medical Laboratory Sciences,*
Nagoya University, Graduate School of Medicine, Nagoya 461-8673, Japan
[2]*Okazaki City Hospital, Okazaki 444-8553, Japan*
[3]*Iwata City Hospital, Iwata 438-8550, Japan*
[4]*Ichinomiya Municipal Hospital, Ichinomiya 491-8558, Japan*
e-mail: rachi.tosiya@e.mbox.nagoya-u.ac.jp

Abstract

Purpose: X-ray output factor (S_{cp}) for a linear accelerator is presented by multiplying in Collimator scatter factor (S_c) by Phantom scatter factor (S_p). The S_c shows the change of output for the linear accelerator, and the S_p shows the change of output in the patient. Because these factors affect a Monitor Unit (MU), the accurate assessment of the S_c and the S_{cp} is required. In this study using Monte Carlo (MC) simulation, we assess whether the general measurements of the output factor is accuracy or not. In addition, if there are the differences between measured output factors and computed those, our aim will be to analyze the reason of the differences and estimate a correction factor.

Methods: According to American Association of Physicists in Medicine (AAPM) Task Group-74, primary dose is proportional to collision water kerma using a proportional factor β. Calculation of the primary dose using MC simulation led to theoretical S_{csim} and similarly led to theoretical S_{psim} by calculating entire absorbed doses and the primary dose in a waterphantom. The linear accelerator of VARIAN CLINAC 2100EX was modeled by using MC code EGS5. The size of the irradiation field calculated by MC simulation were 5×5, 8×8, 10×10, 12×12, 15×15, 20×20, and 30×30 cm^2 and the incident electron energy was performed by 4.5 MeV. And the S_{cp} calculated by EGS5 corresponded to the measured one within statistical error ±0.3 % or less. A miniphantom was made of PMMA of 4 cm diameter and 20 cm length. The cutoff energy of the photon and the electron were performed 0.01 MeV and 0.7 MeV, respectively. Additionally, the spectrums of the particle at 90 cm from the target are obtained and the attenuation and mass energy absorption coefficient are estimated.

Result: The calculated theoretical S_{csim} in waterphantom is higher value than the measured one in the miniphantom. The calculated theoretical S_{psim} is lower than measured one. And when the collimator setting is larger, the relative error of the calculated S_{csim} and S_{psim} is larger. The attenuation and mass energy absorption coefficient could correct this relative error between water and PMMA.

Conclusion: The relative errors between the measured S_c and the indirect S_p and the calculated theoretical values were presented because an ion chamber and the miniphantom made of PMMA were used in the measurements of this study

and the waterphantom was used at the calculation with EGS5.

Additionally, the miniphantom of 4 cm diameter could not accurately be obtained the scatter from a linear accelerator head. As a result, when the collimator setting is larger, the relative difference between the waterphantom and the miniphantom is larger. If the mass energy absorption and the attenuation coefficient between water and PMMA using MC are estimated, the output factor may be more accurate.

1. Introduction

In radiotherapy, the patient who is required to receive the therapy must undergo the Computed Tomography (CT). The obtained image data are sent to radiotherapy treatment planning system (RTPS) to be computed the dose distribution in the patient body from the CT values. When the prescribed dose to the target is decided, the monitor unit (MU) that controls dose by monitor chamber is computed. The MU for field size *s*, at depth *d* in a miniphantom, can be expressed as

$$MU = \frac{D(d,s)\cdot wi}{DMU\cdot S_{cp}(s)\cdot G\cdot TMR(d,s)\cdot WF(d,s)\cdot TF(d,s)}\cdot\cdot\cdot\cdot\cdot(1)$$

where *D(d,s)* is the prescribed dose to the target, *wi* is the weight value of the dose, *DMU* is the absorbed dose per unit of *MU* [cGy/MU], the S_{cp} is total scatter factor, *G* is the collection factor for inverse-square low, *TMR* is tissue maximum ratio, *WF* is wedge factor, and *TF* is tray factor.

The total scatter factor S_{cp} is divided into the collimator scatter factor S_c and the phantom scatter factor S_p by Khan.et.al.$^{1)}$ The S_{cp} and the S_c can be measured, but the S_p cannot be measured, therefore the S_p must be calculated using measured the S_{cp} and the S_c. Here, the S_c shows the output dose of scatter from the accelerator head and is measured using a miniphantom or a buildup-cap. But the difference may occur, if you measure the S_c with the different instrument.

On the other hand, the S_p shows output dose from scattered photons throughout the patient body or the miniphantom. As the S_p cannot be measured on the theory published in American Association of Physicists in Medicine (AAPM) Task Groupe-74, we calculated it using MC simulation.

Although there are some differences between the measured and the calculated values, there is no disadvantage at the case of a square field. However, there is the disadvantage for a rectangular field because these factors are calculated by different method for the equivalent square field of the rectangular field. Eq. (2) and (3) show the calculation methods for the equivalent square field for the S_c and the S_p, respectively.

$$S_c \Rightarrow C_{eq} = \frac{(1+K)X\cdot Y}{KX+Y}\cdot\cdot\cdot\cdot(2)$$

$$S_p \Rightarrow S_{eq} = \frac{2X\cdot Y}{X+Y}\cdot\cdot\cdot\cdot(3)$$

Where, *K* is the collection factor of collimator exchange effect, C_{eq} and S_{eq} are one side length of the equivalent square field for the S_c and the S_p, respectively. Calculation of the water collision kerma and the primary dose using MC simulation leads to the theoretical S_{csim} and S_{psim} by these values. And the relative difference between the measured values and the theoretical those is compared.

2. Materials and Methods

2.1 The modeling of the linear accelerator

The modeling of the linear accelerator from the target to the water phantom or the miniphantom was constructed by using CGView with the structural data of CLINAC series of VARIAN 2100EX[2)]. To reduce the calculating time, a variance reduction method is utilized using the phase space file1 and 2. We assumed that the behaviors of photons and electrons through a flattening filter are constant in spite of the motion of jaws and multi-leaf collimator. Therefore, the phase space file1 was obtained between the flattening filter and the upper jaws (y-jaws), and additionally the phase space file2 was obtained on 90 cm from the target. A percentage depth dose (PDD) and off center ratio (OCR) are calculated by using the phase space file2 data repeatedly to the waterphantom or the miniphantom.

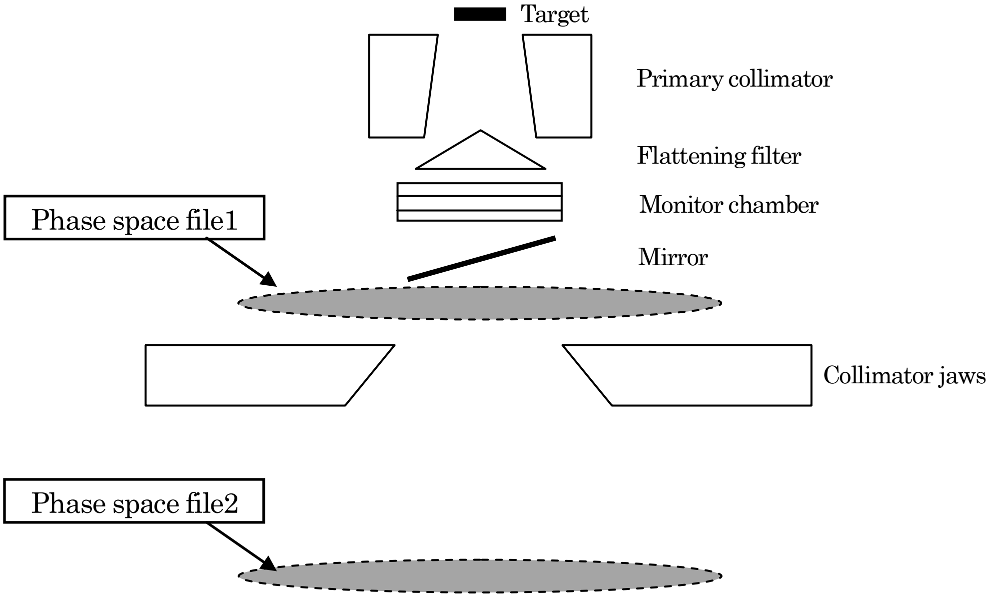

Fig. 1: The geometry from the target to the phase space file2.

Figure 1 shows the created geometry in CGview. For conditions of MC simulation, MC code is Electron Gamma Shower Version5 (EGS5), the incident electron energy is 4.5 MeV using a intensity distribution with 0.4 cm FWHM and incident electron beam spread with 1 % FWHM. Used square fields in this study are from 5×5 cm^2 to 30×30 cm^2. The cut off energy of electron is set to 0.521 MeV and 0.7 MeV as a function of material object and 0.01 MeV for the photon.

The obtained PDD and OCR are compared with measured values of CLINAC 21EX (VARIAN Inc.). Figure 2 and 3 show relative depth dose normalized by 10 cm depth dose and Figure 4 and 5 show the OCR for 5×5 cm^2 and 30×30 cm^2, respectively.

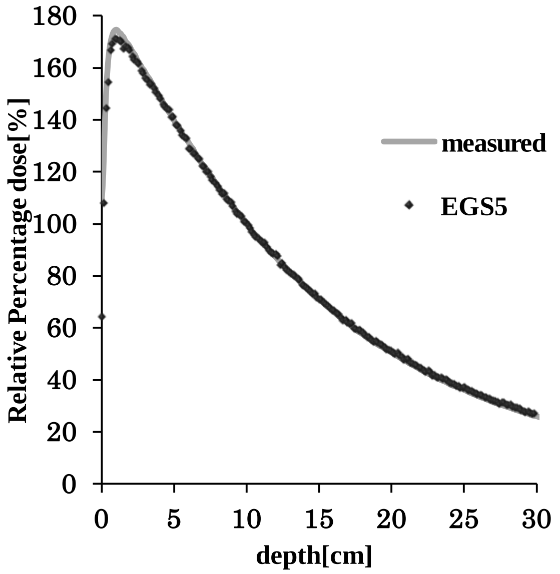

Fig. 2: The measured relative percentage dose normalized by 10 cm depth dose and the calculated one by using MC for 5×5 cm^2. The fractional standard deviation is 2 % or less.

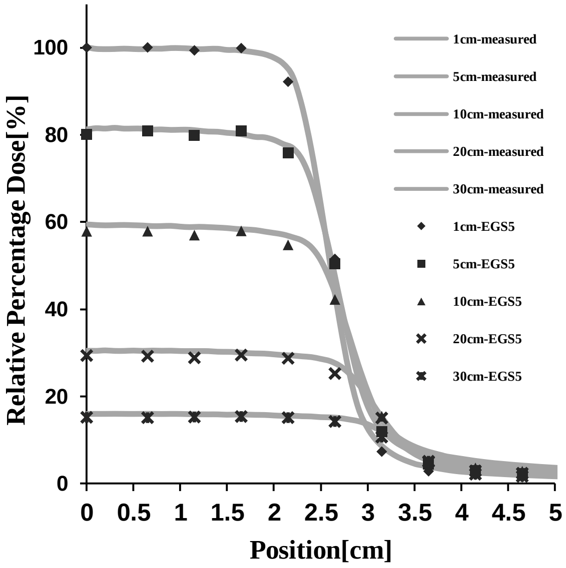

Fig. 4: The measured and calculated OCRs for 5×5 cm^2 at each depth. The fractional standard deviation is 2 % or less.

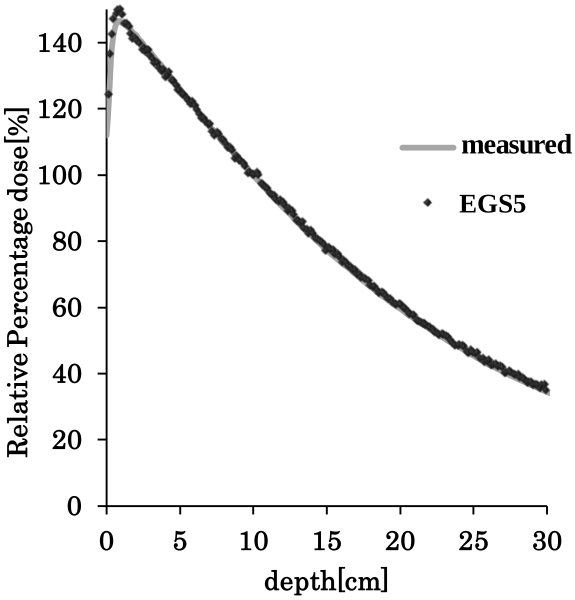

Fig. 3: The measured relative percentage dose normalized by 10 cm depth dose and the calculated one by using MC for 30×30 cm^2. The fractional standard deviation is 2 % or less.

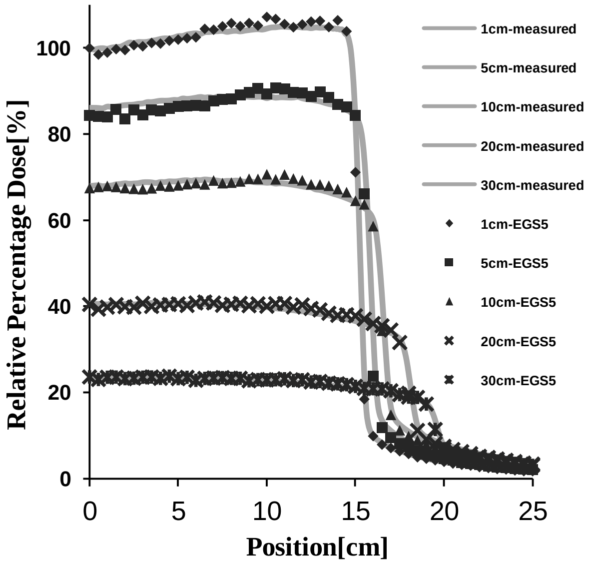

Fig. 5: The measured and calculated OCRs for 30×30 cm^2 at each depth. The fractional standard deviation is 3 % or less.

2.2 Theory

The collimator scatter factor, S_c is defined as the ratio of primary collision water kerma in free–space, K_p, per monitor unit between an arbitrary collimator setting, c, and reference collimator setting, c_{ref}, at the same location on the central axis, where z_{ref} is the reference source-to-detector distance[3)]. When the secondly charged particle equilibrium is realized, the K_p has direct proportional relationship with the primary dose using the proportional factor β, where s is a arbitrary field size, the reference field size, s_{ref}. The S_c definition is expressed as.

$$S_c(c) = \frac{K_p(c,z_{ref})/_{MU}}{K_p(c_{ref},z_{ref})/_{MU}} = \frac{D_p(C=S)/_{\beta(C=S)}}{D_p(C_{ref}=S_{ref})/_{\beta(C_{ref}=S_{ref})}}. \cdot\cdot\cdot (4)$$

The phantom scatter factor, S_p, is defined as the ratio of the scatter factors between the actual field size s and the reference field size s_{ref}, both at the reference depth, d_{ref}, in the phantom. The S_p is expressed as,

$$S_p(s) = \frac{SF(s,d_{ref})}{SF(s_{ref},d_{ref})} = \frac{D(S)/_{D_p(S)}}{D(S_{ref})/_{D_p(S_{ref})}}, \cdot\cdot\cdot (5)$$

where SF is the ratio of the total dose in water D to the primary dose D_p for the same field and same depth.
And the phantom scatter factor is expressed by Eq. (4) and (5). Finally, the S_p is driven as following equation,

$$\frac{S_{cp}(s)}{S_c(s)} = \frac{D(s)/_{D(s_{ref})}}{K_p(c=s)/_{K_p(c_{ref}=s_{ref})}} = \frac{D(s)/_{D_p(s)}}{D(s_{ref})/_{D_p(s_{ref})}} \cdot \frac{\beta(s)}{\beta(s_{ref})}$$

$$= S_p(s) \cdot \frac{\beta(s)}{\beta(s_{ref})} \approx S_p(s). \cdot\cdot\cdot (6)$$

Eq. (6) shows that $\beta(s) / \beta(s_{ref})$ is close to unity when this condition is large enough to provide lateral electron equilibrium.

2.3 The calculated back scatter factor

It is necessary to know the amount of the back scatters to the monitor chamber because MC does not include an early beam stop$^{4)}$. Figure 6 shows the absorbed dose by the back scatters from the jaws. These data change linearly with increasing size of the field.

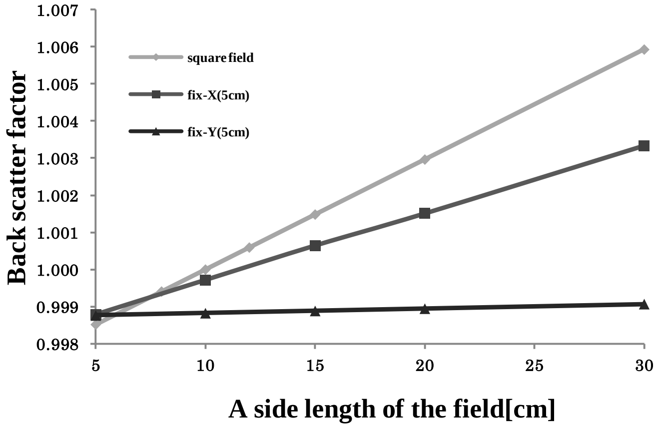

Fig. 6: The back scatter factor according to a side length of the field.

2.4 The mass energy absorption coefficient (*CF_{en}*) and the attenuation coefficient (*CF_a*) correction factor

The measured S_c is corrected to close theoretical S_c value by the mass energy absorption coefficient and the attenuation coefficient correction factor. According to the study of Jun Li et al[5), the mass energy absorption coefficient is expressed as

$$\left(\frac{\mu_{en}}{\rho}\right)^{medium}(c,d) = \frac{\int (\mu_{en}/\rho)^{medium}(E)\cdot e^{-\mu^{medium}(E)\cdot d}\cdot \partial\varphi_c(E)/\partial E\cdot dE}{\int e^{-\mu^{medium}(E)\cdot d}\cdot \partial\varphi_c(E)/\partial E\cdot dE}, \cdot\cdot\cdot (7)$$

where $(\partial\varphi_c(E)/\partial E)$ is the energy spectrum in free air, $(\mu_{en}/\rho)^{medium}(E)$ and $\mu^{medium(E)}$ are the mass energy absorption coefficient and the attenuation coefficient, respectively and these are quoted from National Institute of Standards and Technology (NIST). Therefore, the mass energy absorption coefficient correction factor is

$$CF_{en} = \frac{(\mu_{en}/\rho)^{medium}(c_{ref},d)/(\mu_{en}/\rho)^{water}(c_{ref},d)}{(\mu_{en}/\rho)^{medium}(c,d)/(\mu_{en}/\rho)^{water}(c,d)}. \cdot\cdot\cdot (8)$$

Similarly, the attenuation coefficient is expressed as

$$A^{medium}(c,d) = \frac{\int e^{-\mu^{medium(E)}\cdot d}\cdot \partial\varphi_c(E)/\partial E\cdot dE}{\int \partial\varphi_c(E)/\partial E\cdot dE}. \cdot\cdot\cdot (9)$$

The attenuation coefficient correction factor is

$$CF_a = \frac{A^{medium}(c_{ref},d)/A^{water}(c_{ref},d)}{A^{medium}(c,d)/A^{water}(c,d)}. \cdot\cdot\cdot (10)$$

Therefore, the correction factor is defined as

$$CF = CF_{en}\cdot CF_a. \cdot\cdot\cdot (11)$$

3. Results

3.1 Comparing the calculated S_{cp} and S_c with the measured those

Figure 7 and 8 show that the calculated S_{cp} and S_c compared with the measured those in the waterphantom and miniphantom, respectively. Both the calculated values have the fractional standard deviation of 3 % or less.

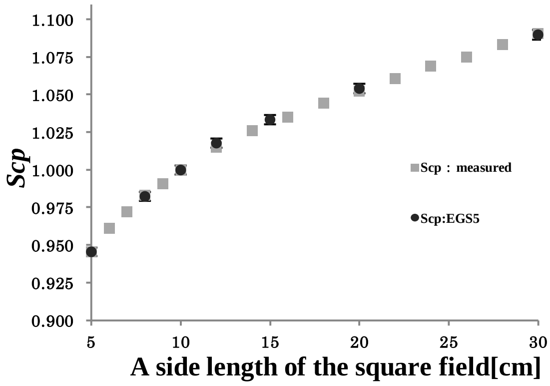

Fig. 7: The measured S_{cp} compared with the calculated one. There is 0.25 % of maximum relative error.

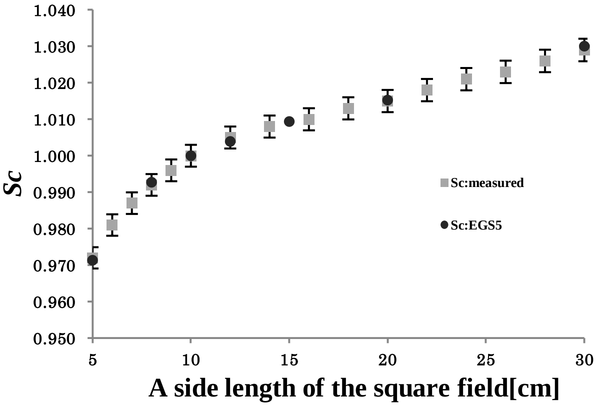

Fig. 8: The measured S_c compared with the calculated one. There is 0.11 % of maximum relative error.

3.2 Comparison of the calculated theoretical S_{csim} and S_{psim} with measured those

The calculated theoretical S_{csim} and S_{psim} are obtained in waterphantom. Figure 9 and 10 show that the calculated theoretical these values$^{6)}$ compared with the measured those.

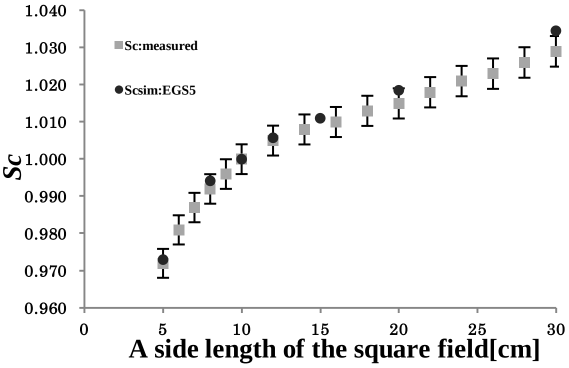

Fig. 9: The measured *Sc* compared with the calculated theoretical S_{csim}. There is 0.59 % of maximum relative error.

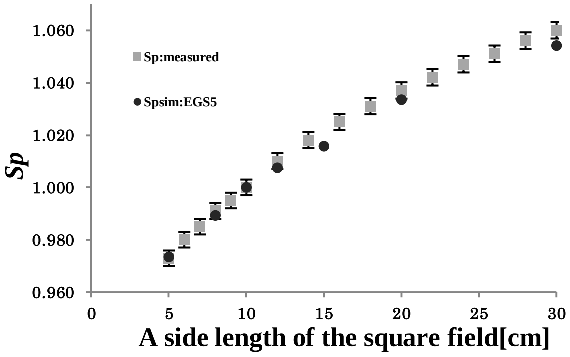

Fig. 10: The measured S_p compared with the calculated theoretical S_{psim}. There is 0.55 % of maximum relative error.

3.3 Comparison of the calculated theoretical S_{csim}／*CF* and S_{psim}×*CF* with the measured those

The *CF* is used to reduce the relative error difference between calculated theoretical values and measured those. Figure 11 and 12 show change of the relative difference when S_{csim} and S_{psim} include the *CF*.

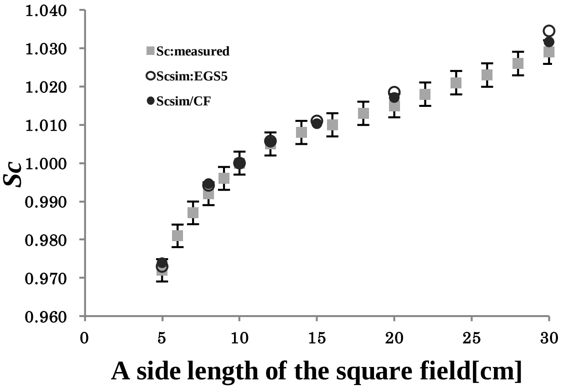

Fig. 11: The measured S_c compared with the calculated theoretical S_{csim} / *CF*. The *CF* reduces the maximum relative difference 0.59 % to 0.26 %.

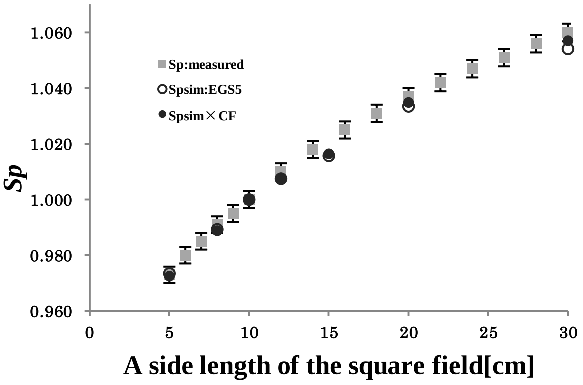

Fig. 12: The measured S_p compared with the calculated theoretical S_{psim}・*CF*. The *CF* reduces the maximum relative difference 0.55 % to 0.27 %.

4. Discussion

4-.1 Energy spectrum to calculate the *CF*

Energy spectra in four square fields are calculated as shown from Figure 13 to 16 and we calculated the *CF* at 90 cm from the target under three different ranges as 4 cm and 10 cm, whole plane.

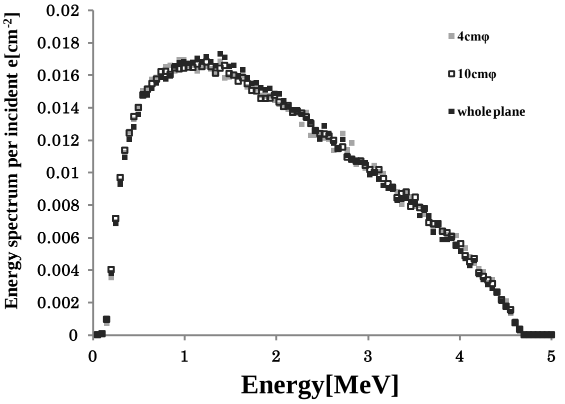

Fig. 13: The energy spectrum for 5×5 cm^2.

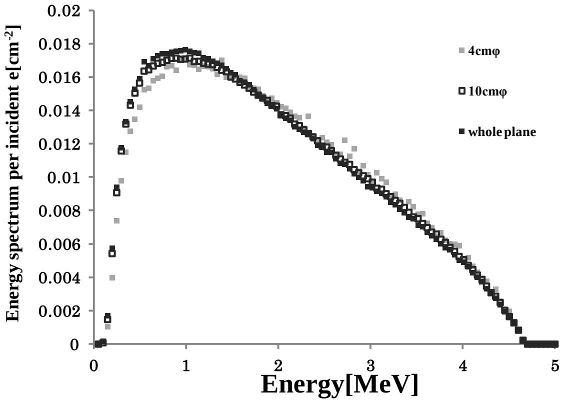

Fig. 15: The energy spectrum for 20×20 cm^2.

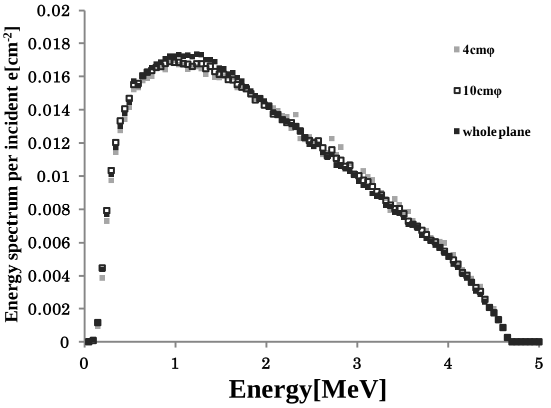

Fig. 14: The energy spectrum for 10×10 cm^2.

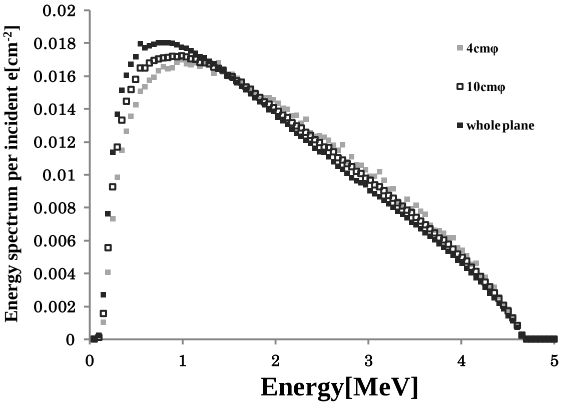

Fig. 16: The energy spectrum for 30×30 cm^2.

Figure 13 represents no change with three ranges. While, Figure 16 represents clearly change that it show larger spectrum in low energy range at whole plane. Here, the miniphantom of 4 cm diameter might not obtain the accurate spectrum in large field.

4.2 Comparison between the measured value and the calculated theoretical value

The calculated theoretical S_{csim} in waterphantom is higher than the measured one in the miniphantom. The calculated theoretical S_{psim} is lower than the measured one. However, the S_{csim} and S_{psim} corrected with the *CF* reduce the maximum relative difference from 0.59 % to 0.26 % and from 0.55 % to 0.27 %, respectively. These two relative differences are within the statistical error range of ±0.3 % by using the *CF*. We used the *CF* (CF_{en}×CF_a) to reduce the relative difference between the measured S_c and the S_{csim}. On the other hand, the S_p cannot be measure in actuality. However, if the S_p is derived using the corrected S_c by the *CF* and the measured S_{cp}, the S_p may close to S_{psim}. Here, it should be noticed that the S_c and S_p are corrected the collision water kerma and the primary dose in waterphantom, respectively.

As a result, the mass energy absorption and the attenuation coefficient correction factors are effectively for correcting difference between the waterphantom and miniphantom (PMMA) medium. The *CF* increases accuracy of the MU.

5. Conclusions

In this study, it is found out that the measured S_c is overestimated than the calculated theoretical S_{csim} by EGS5. Also, the S_p which is derived by the measured S_c and the S_{cp} in the miniphantom or the waterphantom is underestimated than the calculated theoretical S_{psim} by EGS5. Here, we calculated the mass energy absorption (CF_{en}) and the attenuation coefficient correction factor (CF_a) to reduce the relative error between the measured and the calculated theoretical value. By using these *CF*, the measured value closes to the calculated theoretical value and they are agreed within the fractional standard deviation of 0.3 %.

As the result, if the *CF* can be available the accuracy of the measured value using the waterphantom and the miniphantom may be higher than now. It will lead to advance accuracy of the MU.

References

1) F. M. Khan, W. Sewchand, j. Lee, and J. F. Williamson. “Revision of tissue-maximum ratio and scatter-maximum ratio concepts for cobalt60 and higher x-rays beams,” Med. Phys. **7**, 230-237 (1980).
2) D. Seikh-Bagheri, D. W. O. Rogers, “Monte Carlo calculation of nine megavoltage photon beam spectra using the BEAM code”, Med. Phys. **29**, 391-402 (2002).
3) T. C. Zhu, A. Ahnesjo, K. L. Lam, X. A. Li, C. C. Ma, J. R. Palta, M. B. Sharpe, B. Thomadsen, and R. C. Tailor, “Report of AAPM Therapy Physics Comimittee Task Group 74: In-air output ratio, S_c, for megavoltage photon beams,” Med. Phys. **36**, 5261-5291 (2009).
4) Y. Hu and T. C. Zhu, “Backscatter correction factor for megavoltage photon beam,” Med. Phys. **38**, 5563-5568 (2011).
5) J. Li and T. C. Zhu, “Monte Carlo simulation of the effect of miniphantom on in-air output ratio,” Med. Phys. **37**, 5228-5237 (2010).
6) R. Shih, X. A. Li, J. C. H. Chu, and W. Hsu, “Calculation of head scatter factors at isocenter or at center of field for any arbitrary jaw setting,” Med. Phys. **26**, 0506-511 (1999).

COMPARISON ABOUT BRACHYTHERAPY OF SIMULATION EGS5 AND TREATMENT PLANNING BASED ON AAPM TG-43

S. TSUJI and N. NARIHIRO[†‡]
Kawasaki Medical School, Kurashiki 701-0192, Japan
[†]*Kawasaki College of Allied Health Professions, Kurashiki 701-0194, Japan*
[‡]*Okayama University Graduate School of Health Sciences Division of Radiological Technology, Okayama 700-8558, Japan*

Abstract

Treatment plans for high dose-rate brachytherapy are calculated in AAPM TG-43. A radiation dose in TG-43 is investigated by measurements or Monte Carlo simulations, but the investigation is limited to measure for the fixed volume in 30 cm diameter sphere phantom. Absorbed doses are different depending on the size of the phantom. We approximate the elliptical cylinder phantom of the human body shape. Using Monte Carlo simulation EGS5, we investigate doses in various areas of the elliptical cylinder phantom. We compare the results between the simulation EGS5 and the calculation AAPM TG-43.

1 Introduction

Brachytherapy is carried out using the microSelectron-HDR remote afterloading device with high-intensity ^{192}Ir. The sources capsuled in a stainless are embedded and irradiate the prostate. A clinical treatment is planned before an actual irradiation in a body. The calculated values of doses are derived from Oncentra clinical planning system [1]. The calculation algorism follows American Association of Physicists in Medicine Task group No.43 Report (AAPM TG-43) [2], and they are based on dose-rate distributions used for clinical implementations and dose-calculation methodologies. AAPM TG-43 is generally the only way of the algorism for brachytherapy in radiology. The problems of Oncentra clinical planning system using TG-43 formula are based on the Dascalov et al. [3] investigation which is investigated in a liquid water phantom with a 30 cm diameter spherical volume. Absorbed dose will vary depending on the size and shape of the phantom [4, 5, 6, 7]. We simulate doses using the phantom close to a human body. The shape of the phantom is used tan elliptic cylinder. We report comparisons of the doses between the simulation EGS5 and the calculation AAPM TG-43.

2 AAPM TG-43

The Oncentra brachytherapy planning system calculate based on AAPM TG-43 [2]. The dose-rate equation is following,

$$\dot{D}(r,\theta) = S_k \cdot \Lambda \cdot \frac{G(r,\theta)}{G(r_0,\theta_0)} \cdot g(r) \cdot F(r,\theta), \tag{1}$$

where r denote a distance (in centimeters) from the center of the active source to a point of interest, r_0 denotes the reference distance which is specified to be 1 cm in this protocol, and θ denotes a polar angle specifying a point of interest, θ_0 denotes the reference angle which is specified to be 90°.

The other parameter S_k, Λ, $G(r,\theta)$, $g(r)$ and $F(r,\theta)$ represent the air-kerma strength, the dose rate constant, the geometry function, the radial dose function and the 2D anisotropy function respectively. S_k is calculated as the source intensity when a clinical implementation starts. Λ is used the value 1.108 cGy/h/U in this planning system. The unit U is defined as the air-kerma strength, 1U=1cGy·cm^2/h. The detailed parameters are listed in the reference [2].

3 Elderly human body model for the creation of phantom

The phantom used in the simulation is configured in CG (combinatorial geometry). The shape is an elliptic cylinder based on the human body [9]. The targets are 206 people whose ages are between 60 and 79. There are 100 men and 106 women of 206 people. Referred length are "side neck point height", "trochanterion laterale height", "hip breadth" and "buttock depth at great trochanter" in Fig. 1.

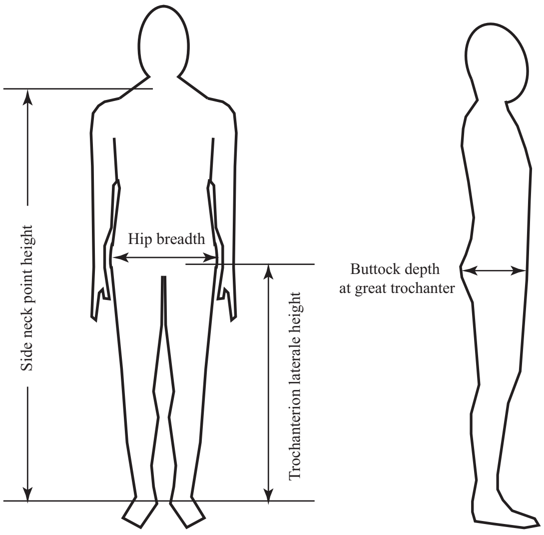

Figure 1: Body dimension. Average human dimensions of 206 elderly people are listed in Table 1.

These average values for 206 people are tabulated in Table 1.

Table 1: Average human dimensions of 206 elderly people. The unit is mm.

	Side neck point height	Trochanterion laterale height	Hip breadth	Buttock depth at great trochanter
206 people	1308	793	322	229
100 men	1366	825	322	231
106 women	1254	763	321	227

4 Simulations

4.1 Elliptic cylinder phantom configured with CG

An object using simulation can be built by combining the several predetermined three-dimensional forms with CG which means "combinatorial geometry". With a reference to Table 1 and using CG, an elliptic cylinder phantom in Fig. 2 is used in simulations. The length of the elliptic cylinder

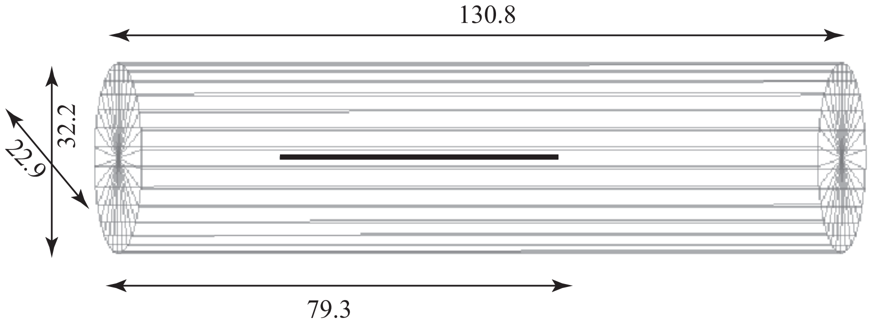

Figure 2: Elliptic cylinder phantom configured with CG. The phantom is constructed by reference to the dimension of 206 elderly people. The unit is cm.

phantom is referred the average the “side neck point height” in Fig. 1. The major and minor axis of the ellipse are referred “hip breadth” and “buttock depth at great trochanter” in Fig. 1. Using these axes, the circumference of the ellipse is 872 mm. The averaged 206 people “buttock circumference” (hips around) is 894 mm and the deference of the circumference between the body and the elliptic cylinder phantom is only 2.2 cm. This elliptic cylinder phantom can be approximated by elderly human body model. Thick solid line in Fig. 2 shows a radiation source and a wire. Assuming that a brachytherapy for prostate cancer is a typical treatment, the position of the source is the same as “trochanterion laterale height” in Fig 1. Therefore, the position of the radiation source is a distance of 79.3 cm from the bottom of the elliptic cylinder. Components of the phantom are the same as the composition of the human body soft tissue [8].

4.2 Normalization

For comparison with results of simulations and the Oncentra calculations based on AAPM TG-43, the results of simulations are required absolute values. In the measurement, the radioactivity of ^{192}Ir is determined by the measurement of the reference air kerma rate and the conversion factor. The conversion factor is listed by the certificate for the radiation source. We use this value to determine the normalization factor for simulations. The normalization factor is determined with simulated dose rate at 1 m from a radiation source in the air. The normalization factor is 2.688 ± 0.006 (photons/Bq·s) and by applying this value, it is possible to determine the absolute dose rate. In order to verify whether this factor is correct, we compared with the Oncentra calculations based on AAPM TG-43 and a simulation with a 30 cm diameter sphere water phantom. This results shows in Fig. 3. As we mentioned before, the Oncentra calculations are investigated in a limited 30 cm diameter sphere water phantom. These results show good agreement, therefore, this normalization factor is valid.

4.3 Position of absorbed dose for simulations

Fig. 4 shows a side view and Fig. 5 shows a top view of an elliptic cylinder phantom in Fig. 2. Absorbed doses for simulations are stored at three heights of the elliptic cylinder phantom. The heights h take 0 cm, 5 cm and 10 cm along the radiation source and wire in Fig. 4. 0 cm is refered to 79.3 cm where the radiation source is placed. The radiation source is located in the center of the ellipse plane in Fig 5. Absorbed doses are stored along the minor axis and the major axis of the ellipse. The distance r at dose point is from 1 cm to 11 cm in minor axis and 1 cm to 15 cm in major axis every 1 cm intervals. To be exact, we aggregate the absorbed dose at the distance r

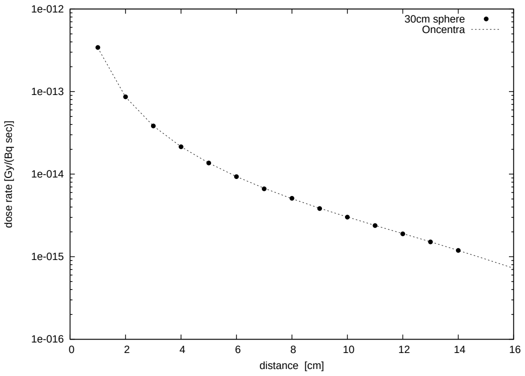

Figure 3: Absolute dose rate of EGS5 simulation and the Oncentra calculation. We use a 30 cm diameter sphere water phantom for EGS5 simulation. ●: EGS5 simulation with a 30 cm diameter sphere water phantom. Dashed line: Oncentra calculation.

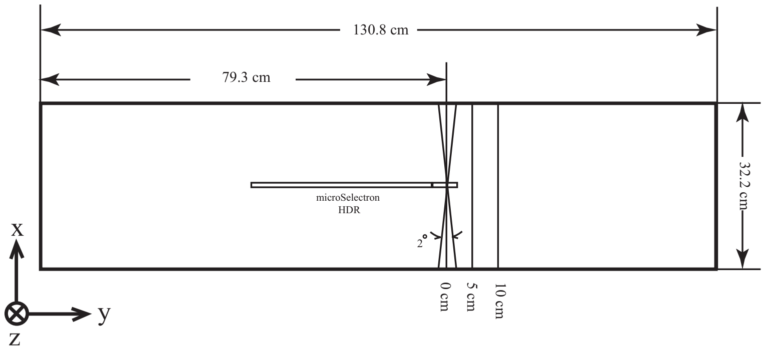

Figure 4: A side view of an elliptic cylinder phantom in Fig. 2. The heights h storing the dose take 0 cm, 5 cm and 10 cm along the radiation source and wire. The angle spread at that position is the ±1°. 0 cm is referenced to 79.3 cm where the radiation source is placed.

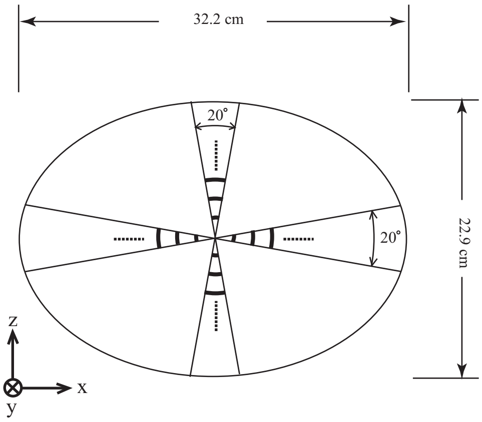

Figure 5: A top view of an elliptic cylinder phantom in Fig. 2. The radiation source is located in the center of the ellipse plane. The distances r storing the dose is from 1 cm to 11 cm in minor axis and 1 cm to 15 cm in major axis every 1 cm intervals. The width of r is 1 mm and the angle spread at that position is the ±10°.

which has a range $R - 0.05$ (cm) $< r < R + 0.05$ (cm), $R = 1, 2, 3, \cdots$ 11 (minor axis) or 15 (major axis). And as a length l of the arc, there is a relationship of $l = r\theta$, we take a range $-10° < \theta < 10°$ in Fig 5. As a height h of an elliptic cylinder phantom, we aggregate in the range $H - r\tan(1°)$(cm) $< h < H + r\tan(1°)$(cm), $H = 0, 5, 10$ in Fig. 4.

4.4 Conditions of Monte Carlo simulation EGS5

We simulate doses using EGS5. For the EGS5 simulating, the following parameters are considered in various regions or mediums, sampling of angular distributions of photoelectrons, K and L edge fluorescent photons, K and L Auger electrons, Rayleigh scattering, linearly polarized photon scattering, incoherent scattering and Doppler broadening of Compton scattering energies. We continue the simulations until the cut off kinetic energy 1 keV for one track. The number of injected particles from the source is 1.5×10^8 per one Monte Carlo simulation.

5 Results

5.1 Absorbed dose rate

Absorbed dose rates along the wire and the radiation source are shown in Fig. 6, Fig. 7 and Fig. 8. Fig. 6 shows at $h = 0$ cm, that is the absorbed dose rate in the same plane of the source. Judging from Fig. 6, there is no difference in the dose rate in the major axis direction, the minor axis direction and the Oncentra calculations. Fig. 7 shows the dose rates at $h = 5$ cm. The dose rates in the minor direction indicate a good agreement with the Oncentra calculations. On the other hand, the dose rate of the major axis direction tends to be away from the calculated value of Oncentra. Fig. 8 at $h = 10$ cm indicates a departure perfectly with the Oncentra calculation in the major direction from the distance $r = 10$ cm.

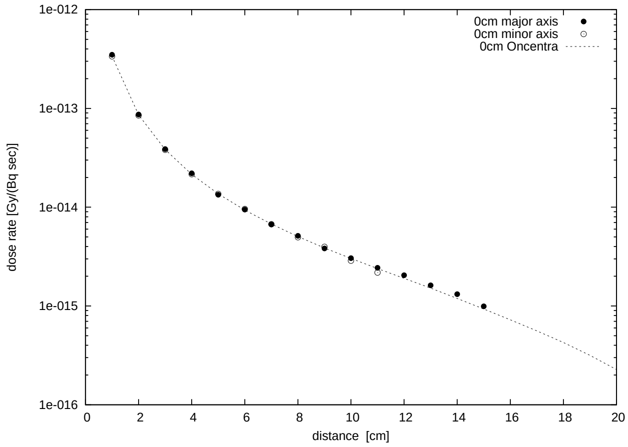

Figure 6: The absolute dose rates at $h = 0$ cm. ●: EGS5 simulation in the major axis direction. ○: EGS5 simulation in the minor axis direction. Dashed line: Oncentra calculation.

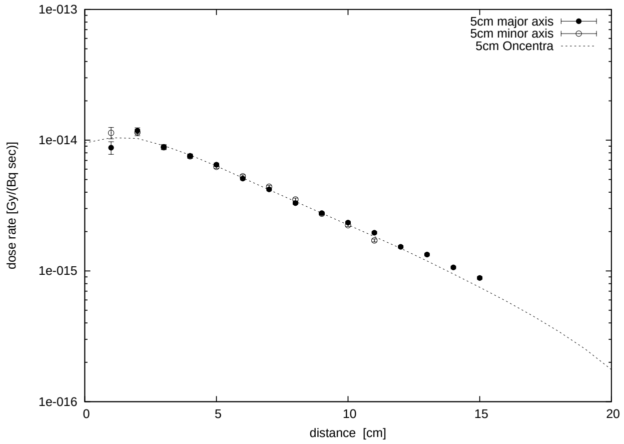

Figure 7: The absolute dose rates at $h = 5$ cm. ●: EGS5 simulation in the major axis direction. ○: EGS5 simulation in the minor axis direction. Dashed line: Oncentra calculation.

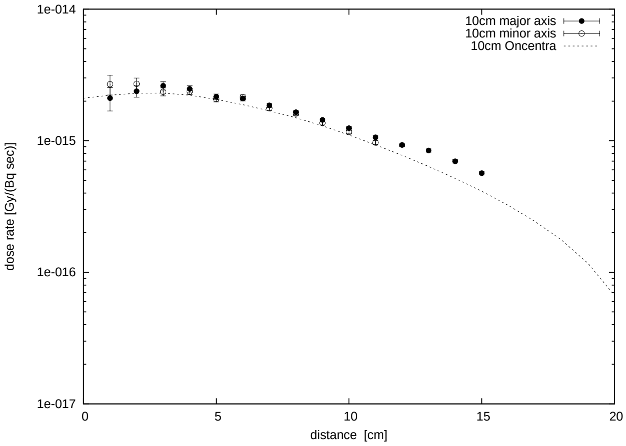

Figure 8: The absolute dose rates at $h = 10$ cm. ●: EGS5 simulation in the major axis direction. ○: EGS5 simulation in the minor axis direction. Dashed line: Oncentra calculation.

5.2 Relative values between the Oncentra calculation and the simulation

In order to compare in detail between the Oncentra calculation and simulation EGS5, we examine the relative values Oncentra/EGS5. Figures from 9 to 14 shows the relative values. Fig. 9 and Fig. 10 indicate the relative values in major and minor axis directions at $h = 0$ cm respectively. The relative values in major axis direction in Fig 9 have been below 1 at the distance r more than 10 cm. On the other hand, the values in minor axis direction in Fig 10 have become above 1 at the distance r more than 10 cm. Both are in the range of roughly 10 %. Fig. 11 and Fig. 12 at $h = 5$ cm tend to be the same as in Fig. 9 and Fig. 10. However the relative values in major axis direction are below near the 20 % at the distance r more than 10 cm. The relative values at $h = 10$ cm show in Fig. 13 and Fig. 14. Both values in major and minor axis directions are less than 1 in all distance r. The values in major axis direction are lower than in the range of 10 % to 30 %.

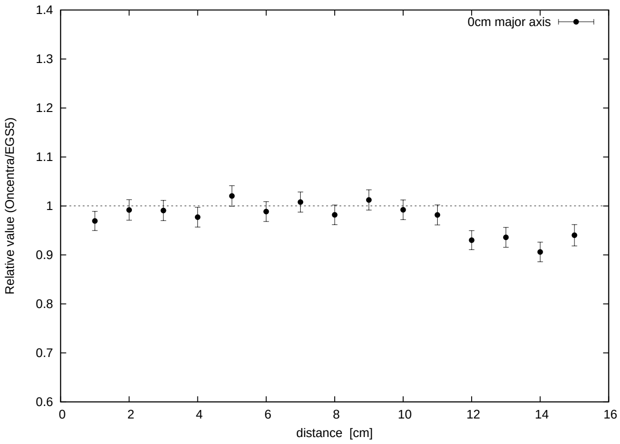

Figure 9: Relative values Oncentra/EGS5 at $h = 0$ cm in the major axis direction.

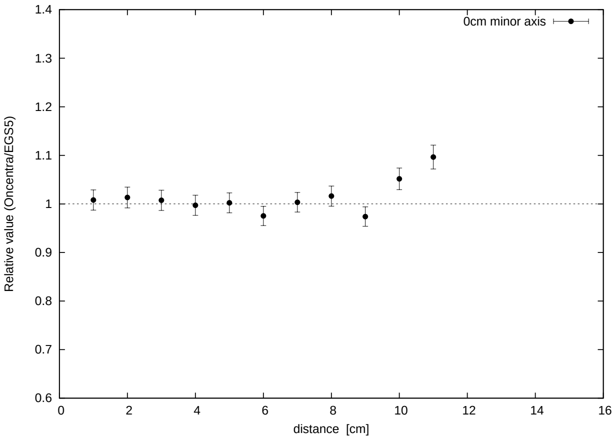

Figure 10: Relative values Oncentra/EGS5 at $h = 0$ cm in the minor axis direction.

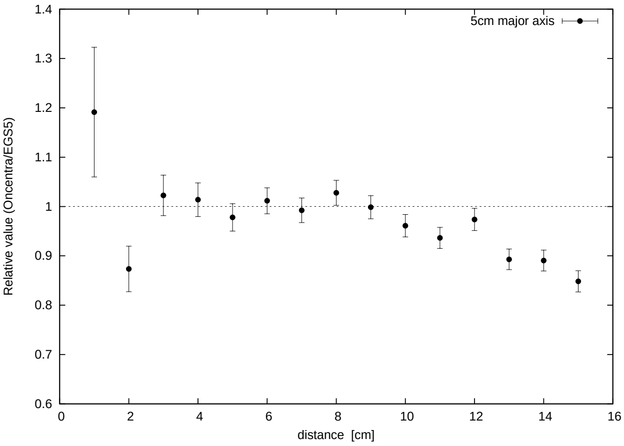

Figure 11: Relative values Oncentra/EGS5 at $h = 5$ cm in the major axis direction.

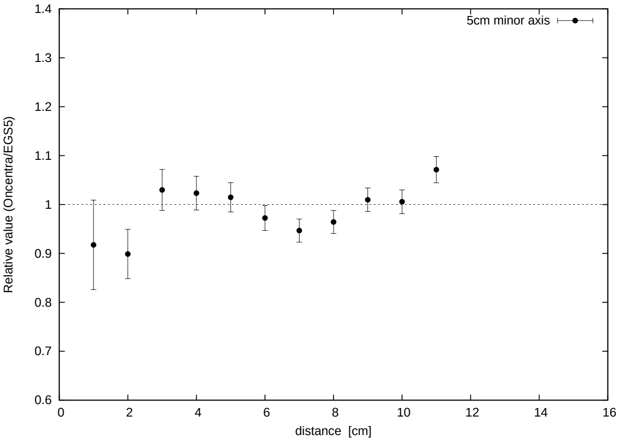

Figure 12: Relative values Oncentra/EGS5 at $h = 5$ cm in the minor axis direction.

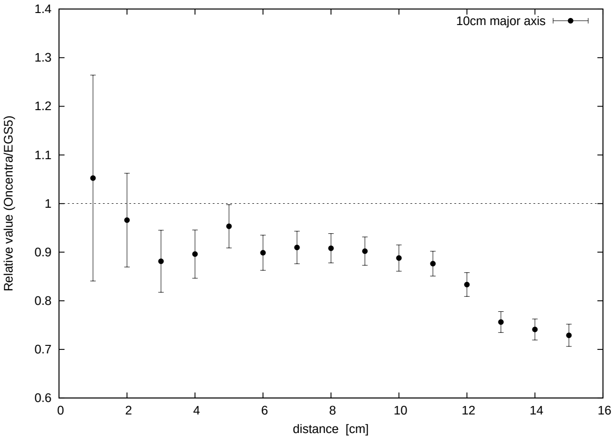

Figure 13: Relative values Oncentra/EGS5 at $h = 10$ cm in the major axis direction.

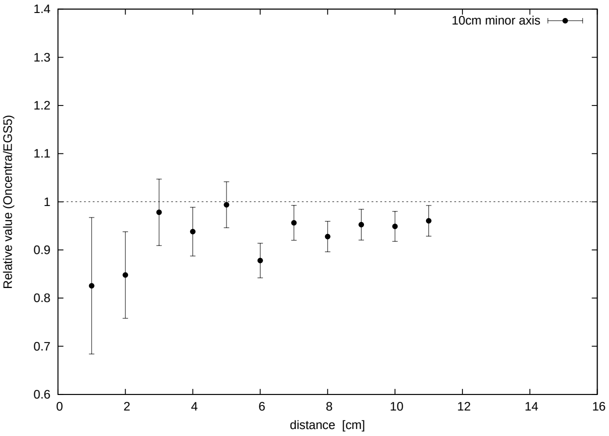

Figure 14: Relative values Oncentra/EGS5 at $h = 10$ cm in the minor axis direction.

6 Conclusion

We compared with the Oncentra calculation based on AAPM TG-43 and the simulation EGS5 using the elliptic cylinder phantom. The elliptic cylinder phantom is made based on the average values of 206 elderly human bodies. In the heights $h = 0$ cm and $h = 5$ cm, the relative values in major axis directions have been below 1 at the distance r more than 10 cm. On the other hand, the values in minor axis directions have become above 1 at the distance r more than 10 cm. This means that the irradiation dose is more than the dose estimated by the Oncentra calculations in a major axis and the dose is less than the estimated dose in a minor axis at the distance r more than 10 cm. In the height h 10 cm, the values in major and minor axis directions are less than 1. In the height h more than 10 cm, the irradiation dose tend to be more than the estimated dose. The Oncentra calculation based on AAPM TG-43 can not be reliable at more than 10 cm. In this paper, the error can be estimated with about 10 % to 30 %. We tried to examine the relative values of the doses separated by men and women. The purpose is simply to see the difference in the volume of the body for the treatment of prostate cancer, not to see the differences between men and women. Judging from Table 1, the differences between men and women are about 11 cm of “side neck point height” (the length of the elliptic cylinder) and 6 cm of “trochanterion laterale

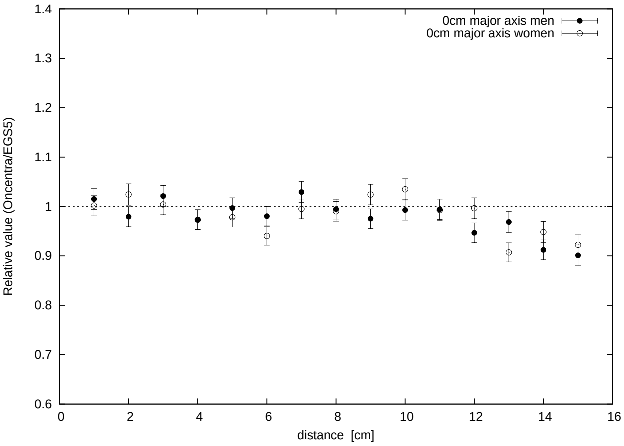

Figure 15: Relative values of men and women Oncentra/EGS5 at $h = 0$ cm in the major axis direction. ●: Men. ○: Women.

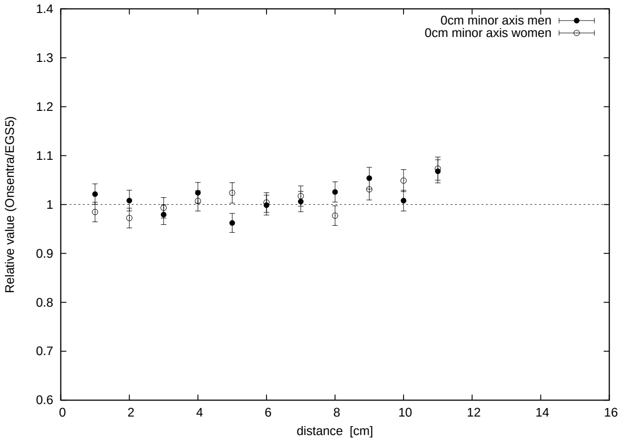

Figure 16: Relative values of men and women Oncentra/EGS5 at $h = 0$ cm in the minor axis direction. ●: Men. ○: Women.

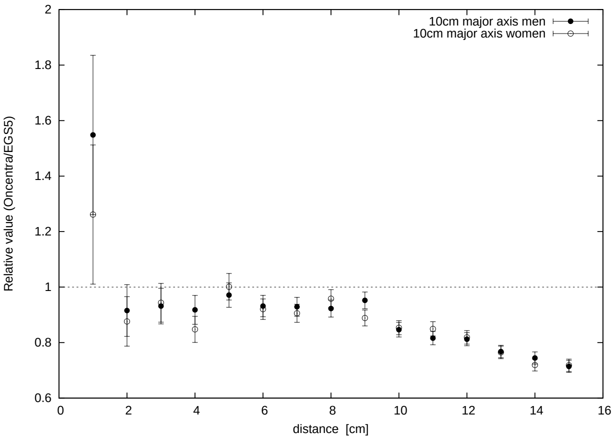

Figure 17: Relative values of men and women Oncentra/EGS5 at $h = 10$ cm in the major axis direction. ●: Men. ○: Women.

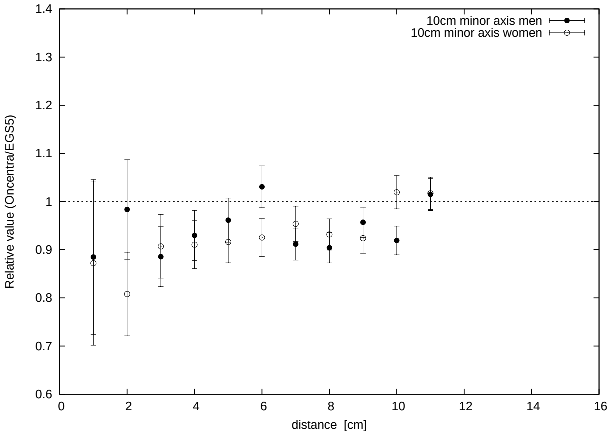

Figure 18: Relative values of men and women Oncentra/EGS5 at $h = 10$ cm in the minor axis direction. ●: Men. ○: Women.

height" (the source position from the bottom of the elliptic cylinder). For other factors, there is no big difference. Fig. 15 and Fig. 16 are the relative values each major and minor axis for each men and women in the height $h = 0$ cm. Fig. 17 and Fig. 18 are also the relative values each major and minor axis for each men and women in the height $h = 10$ cm. Between men and women, the relative values show the same tendency, there was no significant difference.

References

[1] "Oncentra Master Plan v3.3 Physics and Algorithms ", Nucletron, REF 192.739ENG-03.

[2] M. J. Rivard et al., Med. Phys. **31** 3,633(2004).

[3] G. M. Daskalov, E. Lőffler, J. F. Williamson, Med. Phys. **25** 11, 2200(1998).

[4] D. Granero et al., Med.Phys. **35** 11,4872(2008).

[5] P. Karaikos, A. Angelopoulos, L.Sakelliou, Med. Phys. **25** 10,1975(1998).

[6] R. E. P. Taylor and D. W. O. Rogers, Med.Phys. **35** 11,4933(2008).

[7] S. Tsuji and N. Narihiro, Proceedings of the Eighteenth EGS Users ’ Meeting in Japan, KEK Proceedings 2011-6 36-42(2011).

[8] “Atomic and Nuclear Properties of Materials for more than 300 materials, Soft tissue (ICRP)”, http://pdg.lbl.gov/2012/AtomicNuclearProperties/HTM_PAGES/261.html

[9] “Research on the elucidation of the characteristics of the elderly for the design of the equipment for the elderly”, http://www.hql.jp/project/funcdb2000/

VERIFICATION OF DOSE CALCULATION FOR BRACHYTHERAPY USING EGS5

K. Tanaka[1], K. Tateoka[1], O. Asanuma[2], K. Kamo[1], K. Sato[2], H. Takeda[2],
M. Takagi[3], M. Hareyama[3], and J. Takada[1]

[1]Graduate School of Sapporo Medical University, Sapporo 060-8556, Japan,
[2] Sapporo Medical University Hospital, Sapporo 060-8556, Japan,
[3]Teishin-kai Radiation Therapy Institute, Sapporo 060-8556, Japan
e-mail: tanakaken@sapmed.ac.jp

Abstract

The dose obtained from measurement with a radiophotoluminescent glass rod dosimeter (GRD) was compared to the dose calculated with the Monte Carlo (MC) code 'EGS5,' using ^{125}I source structures for model STM1251 and Oncoceed 6711. Some of the GRD positions were so close to the phantom surface that the backscatter margin was less than 5 cm, insufficient for photons. Consequently, the agreement between the MC calculation and GRD measurement support the validity of both methods.

1. Introduction

The dosimetry system using the American Association of Physicists in Medicine Task Group No 43 Updated Protocol 1 (AAPM-TG43U1) has some limitations. For example, it should not be used for small organs, such as the tongue. This is due to the lack of radiation equilibrium scatter conditions as the formalism assumes that dosimetry points have a sufficient amount of backscatter present. Another limitation is that it does not consider the inter-seed attenuation (ISA) which is a result of shielding by other implanted seeds since the dose calculation by the TG43U1 formalism is performed assuming a geometry without additional sources. For treatment planning purposes, the dose calculation should not have limitations as described above. Monte Carlo (MC) simulation is a potential option for this usage. The present study investigated a MC calculated dose distribution in a phantom for comparison to the measured results determined with glass rod dosimeters (GRDs).

2. Materials and Methods

2.1 MC modeling of the linear accelerator treatment head with the MLC

Dosimeters were irradiated with an ^{125}I low-energy brachytherapy source (seed) in an H_2O phantom. The phantom (Figure 1) was a cylinder made of 2 mm thick polymethyl-methacrylate (PMMA) with a diameter of 18 cm and a length of 16 cm. These materials and dimensions were chosen in order to simulate a human head receiving a tongue tumor treatment. The ^{125}I seed "BARD STM1251" was calibrated by the manufacturer with a stated Sk of 0.317U at the beginning of the irradiation, and "Oncoseed No. 6711" of 0.414 U. The irradiation period was about 24 hours. The dosimeters used in this work were radiophotoluminescent glass rod dosimeters (GRDs), GD-302M (Asahi Techno Glass Corporation). The source and GRDs were held in or on the phantom. The source and GRDs were located on the "GRD supporting plate" made of 2 mm thick PMMA set along the phantom centerline as shown in Figure 1 (b). The location in the phantom was r = 0 cm for the source and (r = 1, 2, 3, 4, 6, 8 cm, θ= 0, 45, 90, 135, 180, 225, 270, 315°) for the GRDs. In this case there was one GRD at each position. The GRDs were also placed on the surface along the dashed line in Figure 1 (a) with θ = 0, 45, 90, 135, 180, 225, 270, 315°, and in this case three GRDs were placed side by side at each of the specified angle θ. The GRDs were calibrated using a 6 MV X-ray beam from a linear accelerator (Primus KD2/7467, Toshiba Corporation). For the ^{125}I seed irradiation, the absorbed dose to water was estimated after correcting the photon-energy dependence of the GRD using the ratio of the mass energy-absorption coefficient.

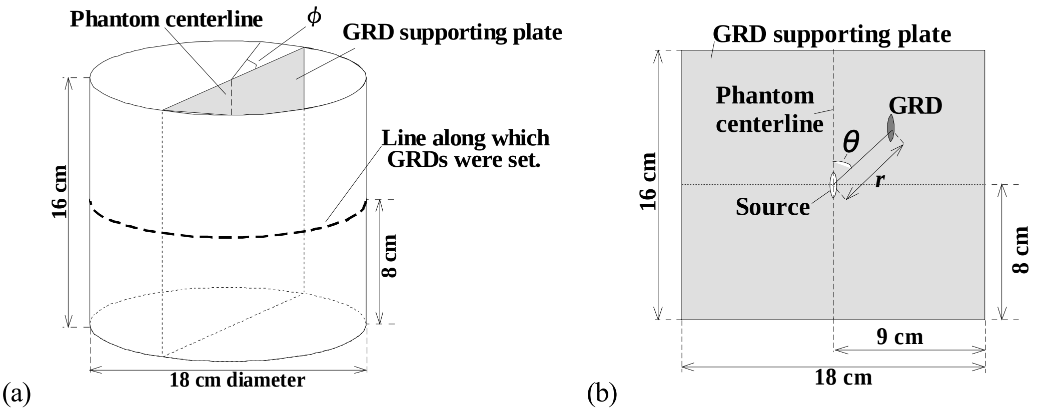

(a) (b)

Figure 1. Geometry for the dosimetry using a cylindrical phantom.

2.2 Validation of the MC models of the treatment head and the MLC

Calculations were carried out using the MC code EGS5.[2] At least 1x10^8 histories were simulated to obtain statistical uncertainties below 2%, as described in TG-43U1. The absorbed dose to the GRDs was calculated for the same geometry as the GRD measurement. The calculation geometry included the ^{125}I seed, GRDs, and phantom placed on a Styrofoam block (25 cm x 25 cm x 20 cm in thickness) and Pb (90 cm x 90 cm x 6 cm in thickness). The geometry input for the STM1251 was the same as that used by Kirov et al.[3], and Oncoseed 6711 as that used by Kennedy et al.[4] The EGS5 output was then converted to an absorbed dose to water using the mass energy-absorption coefficient.

3. Results

3.1 Dose distributions in/on phantom

The absolute value of the dose obtained with the GRD measurements and MC calculations was normalized to the TG43U1 formalism at its reference point, defined as 1 cm from the longitudinal axis of the source (r = 1 cm, θ = 90°). The reference point corresponds to the points (r = 1 cm, θ = 90°) and (r = 1 cm, θ = 270°) in the GRD experiment.

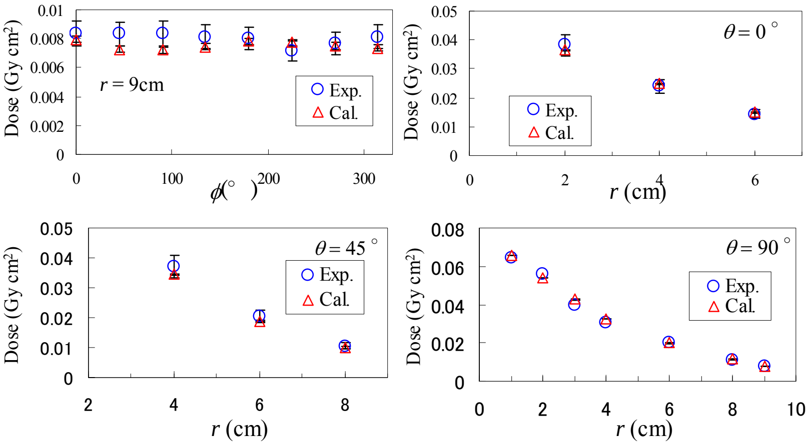

Figure 2. Comparison of the dose between the GRD measurement and MC calculation for the seed STM1251. To show the difference clearly, the dose is exhibited after being multiplied by the square of the distance.

The comparison between the GRD measurement and MC calculation after normalization is shown in Figures 2 for STM1251. The results for Oncoseed 6711 was previously published.[5] The value (Gy cm^2) is the dose multiplied with the square of the distance between the source and GRD. The distribution over 180° shows the similar tendency to that over 0°, 270° was similar to 90°, and 135°, 225°, 315° were similar to 45°, accordingly they are not shown in Figures 3. The ratio of the MC calculation to the GRD measurement ranged from 0.87 to 1.13 for STM1251, and 0.89 to 1.25.for Oncoseed 6711.

3.2 Dosimetry parameters of TG43U1 formalism

In order to check the validity of the present MC calculation, $g(r)$ and $F(r,\theta)$ were estimated. The results for STM1251 are shown in Figure 3. The detailed results are previously reported.[5] $F(3\text{cm},\theta)$ and $F(5\text{cm},\theta)$ are not exhibited because they show similar consistence to $F(2\text{cm},\theta)$ between MC and TG43U1. The uncertainty for this work was set at the statistic error in MC calculation. The uncertainty for the TG43U1 was set at 6.7% as an example because its complete list was not reported.[1] Calculated $g(r)$ using the EGS5 code for STM1251 agree with the TG-43U1 consensus data set to within 7% over all distances. Similar agreement was observed with $F(r,\theta)$ to within 5%, with the exception of small values of r and θ. In those points, the EGS5 calculation overestimated $F(r,\theta)$ by about 35% at (2 cm, 0°), 32% at (3 cm, 0°), and 24% at (5 cm, 0°). This lack of agreement is consistent with that between the investigations in determining the parameters of the TG43U1 formalism for STM1251.[6] The calculation of TG43U1 parameters and uncertainty estimation are still ongoing.

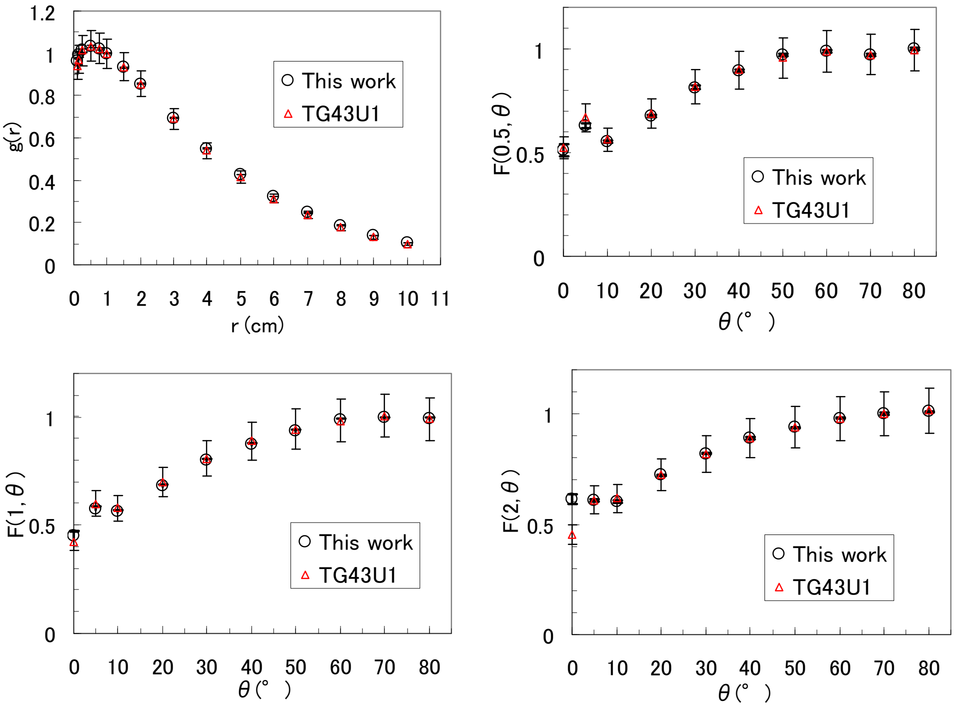

Figure 3. Comparison of TG43U1 parameters with MC calculation for STM1251.

4. Conclusions

The combination of EGS5 and source structures was found to reproduce the GRD measurement for ^{125}I model STM1251 within 18% and Oncoseed 6711 within the 25% uncertainty in the geometry lacking the equilibrium radiation scatter conditions. Also, $F(r,\theta)$ and $g(r)$ estimated by this calculation method were consistent with those proposed in the

TG43U1. The calculation of TG43U1 parameters and uncertainty estimation are still ongoing. The calculation tested is a potential option for treatment planning applicable to the ISA condition and the geometry lacking the equilibrium radiation scatter.

Acknowledgments

Part of the present study was supported by Grant-in-Aid for Scientific Research from the Japan Society for the Promotion of Science under grant #21791203, and by Grant-in-Aid from Sappro Medical University in 2012. For the support in experiments, the authors express their sincere appreciation to Division of Radiology and Nuclear Medicine in Sapporo Medical University Hospital and Hokkaido University including Mr. Keiji Goto, workshop in Sapporo Medical University including Mr. Yoshiyuki Kanazawa. For the kind advice about the present study, the authors thank to Medicon corporation including Mr. Takayoshi Nishida, and Asahi Techno Glass Corporation.

References

1) Rivard MJ, Coursey BM, DeWerd LA, William FH, Huq MS, Ibbott GS, Mitch MG, Nath R, Williamson JF. Update of AAPM Task Group No. 43 Report: A revised AAPM protocol for brachytherapy dose calculations. Medical Physics 2004:31:633-674.
2) Hiramaya, Y. Namito, A.F. Bielajew, The Egs5 code system, report 2005-8 (High Energy Accelerator Research Organization, Tsukuba, Japan, 2009).
3) Kirov AS. Williamson JF. Monte Carlo-aided dosimetry of the Source Tech Medical Model STM1251 I-125 interstitial brachytherapy source. Medical Physics 2001:28:764-772.
4) Kennedy RM, Davis SD, Micka JA, DeWerd LA. Experimental and Monte Carlo determination of the TG-43 dosimetric parameters for the model 9011 THINSeed™ brachytherapy source Monte Carlo and experimental dosimetry of an 125I brachytherapy seed. Medical Physics 2010:33:1681-1688.
5) Tanaka K. Tateoka K. Asanuma O, Kamo K, Bengua G, Sato K. Ueda T, Takeda H, Takagi M, Hareyama M, Takada J. A dosimetry study of the Oncoseed 6711 using glass rod dosimeters and EGS5 Monte Carlo code in a geometry lacking radiation equilibrium scatter conditions. Medical Physics 2011:38:3069-3076.
6) Rivard MJ. Butler WM. DeWerd LA. Huq MS. Ibbott GS. Meigooni AS. Melhus CS. Mitch MG. Nath R. Williamson JF. Supplement to the 2004 update of the AAPM Task Group No. 43 Report. Medical Physics 2007:34:2188-2205.